九州大学学術情報リポジトリ
Kyushu University Institutional Repository

A Study on the Interaction between Baroclinic Waves and Orographically Produced Stationary Vortices

守田, 治

https://doi.org/10.11501/3052545

出版情報：九州大学, 1990, 理学博士, 論文博士
バージョン：
権利関係：

A Study on the Interaction between Baroclinic Waves and Orographically Produced Stationary Vortices

守田治

A Study on the Interaction between Baroclinic Waves and Orographically Produced Stationary Vortices

by Osamu Morita

INDEX

Abstract

The interaction between migrating baroclinic waves and stationary vortices produced by a simple-shape orography was investigated through laboratory experiments using a rotating annulus of fluid.

Investigation was made of the transition from an upper symmetric to a wave regime. Examination was conducted of the heat flux, the structure of stationary vortices and baroclinic waves along with the time-dependent behavior of the baroclinic waves. For a given zonal wavenumber the transition from an upper symmetric to a wave regime occurred at a lower thermal Rossby number in the skewed field than in the axisymmetric field. This exhibits the stabilizing effect of the orography, which is consistent with the results by Jonas (1981). The structure of baroclinic waves showed a dependence on the zonal direction, that is, amplification occurred on the lee side of the obstacle, confirming the results of a linear theory by Frederiksen (1979) and Niehaus (1980).

§ 1. Introduction

Baroclinic waves in a rotating annulus of fluid have been studied both theoretically and experimentally by many researchers because of its simple situation without losing their essential qualities in studing some aspects of atmospheric and oceanic flows. Placing an obstacle in a channel of the rotating annulus of fluid abruptly makes the problem complicated owing to the following: 1) the interaction between migrating baroclinic waves and stationary vortices created by the orography 2) baroclinic instability in the skewed field or lee cyclogenesis 3) formation of a Taylor column in the stratified fluid and 4) trapping or shedding of vortices due to the orography in the stratified fluid.

The effect of large scale mountains on the general circulation has been studied by Manabe and Terpstra (1974). Using a general circulation model they found that a stationary trough is formed on the lee side of large mountains, accompanied by an increase of the kinetic energy of stationary disturbances and a decrease of the kinetic energy of transient disturbances along with lee cyclogenesis. Smith and Davies (1977), using a two-layer, β -plane quasi-geostrophic model, obtained similar results while also finding that the kinetic energy oscillate with a period of about 5 days due to the interaction between baroclinic and stationary waves.

Frederiksen (1979) and Niehaus (1980) have studied lee cyclogenesis theoretically. Frederiksen used a linear, two-

layer quasi-geostrophic spherical model with a basic state consisting of a jet at 30° N and an upper layer long planetary wave while Niehaus (1980) used a continuously stratified linear model with a skewed basic field. In spite of the differences in their models they obtained the same results: the growth rate of baroclinic waves barely changes and disturbances have their maximum amplitude on the lee side of the troughs. Niehaus (1980) further indicated that a distortion of the basic field shifted the maxima in the growth rate to lower zonal wavenumbers.

Wakata and Uryu (1984) have studied topographically forced baroclinic waves in a continuous zonal flow. They showed that a resonance occurs at the critical thermal Rossby number in a constant shear flow that has a zero vertical mean. One of the three equilibrium solutions is stable near a resonant point. Three equilibrium solutions also exist at a slightly off-resonant condition about a basic zonal flow. In this case, trapping and traveling of forced baroclinic waves occurs, according to the height of the topography. When these baroclinic waves migrate, amplitude vacillation occurs because of the stability change in the basic temperature field.

Since the works of Proudman (1916) and Taylor (1917) the well-known Taylor-Proudman theorem was formulated and has been studied by many reseachers. Huppert (1975) gave exact expressions for initiation of a Taylor column for both a homogeneous and a stratified fluid. His results stated that the normalized obstacle height divided by the Rossby number is an appropriate

measure for the initiation of a Taylor column for both cases and especially in the stratified fluid if the obstacle is somewhere vertical, a Taylor column is formed no matter how small a height of an obstacle is. Huppert and Bryan (1976) studied the interaction between zonal currents and an isolated topography and found that a cold anticyclonic vortex was formed over the topography, while a warm cyclonic vortex was formed due to the sinking of fluid after interaction with the topography. The cyclonic vortex was shed when the zonal flow was strong or became trapped near the topography when the zonal flow was weak.

Only a few studies of annulus experiments with bottom topography have been conducted so far. Yeh and Chang (1974) performed experiments to study the dynamical and heating effect of the Tibetan Plateau on a baroclinic flow by introducing a half ellipsoidal obstacle with its major axis slightly shifted with respect to the azimuthal direction. They were mainly concerned with the heating effect of the topography. However, while the heating was not strong enough to reverse the horizontal temperature gradient, the heating effect was similar to a dynamical effect of the topography except for its phase. Their results showed that the basic zonal flow was weakened by the drag of the topography while a stationary anticyclonic vortex was formed in the upper layer just above the obstacle. Furthermore, drifting cyclonic vortices were split in the upper layer while they intensified and expanded in the middle and lower layer above the obstacle. Jonas (1981) studied the effect of topography on baroclinic waves in laboratory experi-

ments. He constructed the bottom topography to have a dominant zonal wavenumber close to that of baroclinic waves with no topography and had an amplitude about 10% of the mean depth of the fluid. His results showed that the transition from baroclinically stable to unstable flows is stabilized in the presence of topographic forcing. On the other hand, Gent and Leach (1976) studied baroclinic instability using an eccentric annulus, whose thermal Rossby number changed gradually in the azimuthal direction. Their results revealed that baroclinic instability is a local phenomenon.

More recently, Boyer and Chen (1987) have performed some experimental simulation on the atmospheric flows in the Northern Hemisphere using a vertically stratified rotating fluid, including a realistic large topography at the bottom. It is noted that they have got somewhat similar flows to the real atmosphere inspite of including the mechanical effect only.

The present study investigates the interaction between migrating baroclinic waves and stationary vortices created by orography. The description of the experimental apparatus and a measuring technique are given in Section 2, the transition from a baroclinically stable to unstable flow, the heat flow measurement and the observation of the surface flow pattern are mentioned in Section 3, while the meridional distribution of the basic and perturbed temperature field is described in Section 4. The azimuthal structure of the basic and perturbed temperature field and the time-dependent behavior of each Fourier mode is detailed in Section 5. The structure of

orographically forced baroclinic waves based on a linear theory is shown in Section 6 while the vertical structure of baroclinic waves is given in Section 7. The summary and discussion follows in Section 8.

§ 2. Experimental apparatus and measuring technique

The cross section of the annulus used in this study is shown in Fig. 1. The working fluid is contained in the annular region (experimental chamber) between two concentric brass cylinders, whose radii are 7.1 cm and 16.7 cm. The fluid depth is 10.0 cm and the upper surface is free. Constant horizontal temperature difference is imposed between the outer and inner walls, each of which is maintained at constant temperatures within the accuracy of $\pm$ 0.05℃ by circulating water from heat baths. The entire system is mounted on a turntable T, which can be rotated at a uniform rotation rate Ω by a continuously variable-speed motor drive. A cylindrical obstacle, 5.0 cm in diameter and with varying heights from 1 cm to 10 cm with increments of 1 cm, is settled at the bottom at the mean radius of the channel. The surface flow pattern is visualized by aluminum powder and streak photographs are taken by the camera set on a sub-table, which is attached just above the turn table with the same rotation axis and rotates synchronously with it. To detect the basic field and wave disturbances, temperatures are measured by three different arrays of thermistor thermometers whose diameters are 0.15 cm. Details of the positioning of the array of probes will be described at the beginning of each related section. Change of voltage due to change in electric resistance is transferred to a desk top computer through a low-noise slipring, Wheatstone bridges, D.C. amplifiers and an A/D converter. Voltage data are converted to

temperature data by a calibration curve for each probe. Temperature data thus obtained have accuracies within ± 0.001℃. The data are simultaneously recorded by a chart recorder in order to monitor the behavior of the temperature field.

Notations which will appear hereafter are defined in Appendix A.

§ 3. Transition, heat flow measurement and surface flow pattern

Transition from an axisymmetric to a wave regime in a rotating annulus with bottom topography has been discussed by Jonas (1981). In this case, the bottom topography was cyclic and sinusoidal, having a wave length comparable with that of the preferred baroclinic waves. The wave amplitude of the topography was very small compared with the depth of the fluid. His results are as follows: 1) the baroclinic flow was stabilized in the presence of a small amplitude topography and 2) when baroclinic waves were present they were of shorter wavelength and larger amplitude than those in flows driven by similar temperature differences in the absence of topographic forcing.

In the present case, the zonal wavenumber of the orography corresponds approximately to 7～ 8, larger than the preferred baroclinic wavenumber. Since the orography is of a single object, it contains a very wide range of Fourier components. Further, the height of the orography varies from 1 to 10 cm, which is comparable with the depth of the fluid layer.

In the transition experiments, the height of the obstacle is varied from 1 to 10 cm, the imposed horizontal temperature difference ΔT is fixed for the two experiments at 5℃ and 10℃, and the rotation rate Ω is changed continuously from 0 to 0.4 rad/sec. Transition is judged by the change of the surface flow pattern visualized by use of aluminum powder and the discontinuous change of the heat flow with Ω. The results are

shown in Figs. 2(a) and 2(b), corresponding to the temperature difference of 5℃ and 10℃, respectively. The numerals in the figures are the preferred wavenumbers and K denotes the transition points after Kaiser (1970) while E(k) is the Eady's criterion (Eady, 1949) for wavenumber k. The Eady's criterion for a given wavenumber is calculated using the corrected Brunt-Väisälä frequency ε N, since this correction is needed because of the formation of sidewall thermal boundary layers with a very large temperature gradient (Williams, 1967; McIntyre, 1968; Kaiser, 1969; Ketchum, 1972; Uryu et al., 1974). The value of ε is chosen to be 0.8 after Ketchum (1972) and from the results of the present experiment. The transition curve from an axisymmetric flow to wavenumber 1 is shown by a dotted line. Since the envelope of the wave does not extend through the entire annulus but is rather localized, the wavenumber evaluated from its horizontal scale corresponds to 2 or 3. The streak photograph of wavenumber 1 is shown in Photo. 1 and the structure of it is discussed in Appendix B. Transition with topography occurs at a larger thermal Rossby number Θ than with no topography, showing the destabilizing effect of the topography. This is especially true when the normalized height of the topography is 0.3 and 0.8. However, this destabilizing effect is due to the excitation of baroclinic waves of wavenumber 2, which are seldom observed with no topography. In contrast, as far as wavenumber 3 is concerned, the transition with topography occurs at a smaller Θ than it does with no topography, showing the stabilizing effect of the topography. The

above results are consistent with those of Jonas (1981).

Heat flow from the outer to inner wall is determined by use of two thermistor thermometers Q1 and Q2 (see Fig. 1), detecting the temperature difference between the inflow and outflow circulating water in the cool bath C. The temperature difference is converted to heat flow by using a calibration curve. This calibration curve is obtained as follows. An electric heater, whose heating rate is continuously varied by a voltage regulator, is inserted in the cool bath C and the heating rate is measured by a wattmeter. Simultaneously the temperature difference is detected by two thermistor thermometers, keeping the entire system at a constant temperature. The above procedure is repeated at several heating rates from which the calibration curve is obtained. This technique is basically the same as that adopted by Uryu et al. (1974).

The heat flow results are shown in Figs. 3(a), (b) and (c). When there is no obstacle, the heat flow decreases almost linearly with rotation rate Ω in an axisymmetric regime, as was pointed out previously by a number of researchers (Bowden and Eden 1965, Kaiser 1971 and Uryu et al. 1974)[1]. When topography exists in a channel, the heat flow behaviors can be separated into two kinds, depending on the height of the topography. In the state of low topography (Fig. 3a), the heat flow

---

1. This experimental result is very old, but it should be emphasized because it is not yet solved!

scarcely changes, compared with that of no topography. In the state of high topography (Fig. 3b, 3c), the amount of heat flow increases according to the increase of the height of topography and the dependence of the heat flow on the rotation rate Ω becomes week. This tendency becomes more prominent as the topography is raised. When the normalized height of the topography exceeds 0.7, the heat flow hardly changes with Ω . These results indicate that there is a critical height of the topography; under which the heat is transported by a stationary vortex caused by the orography, the radial temperature gradient is reduced, the activity of the transient baroclinic waves decreases and the total heat flow both by a stationary eddy and transient waves remains almost constant as a result. When the height of the topography exceeds the critical value, the stationary eddy transfer so much heat that the decrease of the heat flow by transient waves cannot compensate the excess. This result is consistent with that obtained by Cehelsky and Tung (1987) using a two-layer model. Manabe and Terpstra (1974) pointed out that the sum of the stationary and transient eddy kinetic energy is only slightly affected by mountains since they cause a remarkable increase in the kinetic energy of stationary disturbances but simultaneously show a decrease in that of the transient eddies. It seems that in their case the height of mountains was under the critical value.

Photo. 2(a), 2(b) and 2(c) show the surface flow patterns when the baroclinic wave of wavenumber 3 appears. It is observed that when the baroclinic wave passes through the

obstacle, the wave length becomes short on the upstream side of the obstacle and becomes long on the lee side of it. The mechanism of this phenomenon will be discussed in Section 8.

§ 4. Meridional distribution of the basic and perturbed temperature field

Meridional distributions of the basic and perturbed temperature fields are measured by the array of probes shown in Fig. 4. Five probes are placed on the downstream side of the obstacle at θ = 30° and r = 8.1, 10.0, 11.9, 13.8 and 15.7 cm, respectively. Three probes are set just above the obstacle at θ = 0° and r = 8.1, 11.9 and 15.7 cm. The last three probes are positioned on the upstream side of the obstacle at θ =-30° and r = 8.1, 11.9 and 15.7 cm. Initially all these probes are set at z = 9.0 cm , and they are moved down vertically at intervals of 1 cm.

The imposed temperature difference Δ T is fixed at 5℃ , the normalized height of the obstacle H/d is 0.5 and the rotation rates Ω are 0.0, 8.08×10^{-2}, 1.506×10^{-1}, 2.027×10^{-1}, 2.561×10^{-1} and 2.907×10^{-1} rad/s. When Ω is greater than 2.0×10^{-1} rad/s, baroclinic waves appear with a preferred wavenumber of 3. In Figs. 5(a)-(e), the basic temperature fields at the three different azimuthal positions and for the five Ω are shown. On the upstream side of the obstacle (θ = -30°), the horizontal gradient of the basic temperature is almost identical to that for the case of no topography for all values of Ω . On the other hand, the horizontal temperature gradient on the downstream side of the obstacle (θ = 30°) appears to decrease.

In Fig. 6, Fourier components of the normalized temperature perturbation are shown for the case of no obstacle. For

the ground mode, the maximum temperature deviation exists in the middle layer. The axis of the maximum deviation inclines slightly from the upper inside to the lower outside region in the meridional plane. The maxima of the second harmonic exist in the upper layer and in the lower layer and the axis of the maximum deviation has the same tendency as the ground mode. The third harmonic has two maxima whose values are very small. The amplitudes of the sideband modes are also small.

In Figs. 7(a)-(c), the meridional distributions of the normalized temperature perturbations are shown at three different azimuthal positions, that is θ = -30° , 0° , 30° . The gross features of the ground mode Fourier component on the upstream side of the obstacle (θ = -30°) are similar to those of no topography, except that the axis of the maximum deviation becomes vertical in the lower layer. Just above the obstacle (θ = 0°), the value of the maximum increases slightly. On the downstream side of the obstacle (θ = 30°), the value of the maximum increases by about 20%. Its position shifts to the center of the fluid layer and the axis of the maximum deviation becomes vertical in the upper and middle layers. The second harmonic shows two maxima, appearing at θ = -30° as in the case of no obstacle. At θ = 30° , the maximum in the upper layer shifts downward with its value diminishing while the second maximum which is found in the lower layer disappears.

Figs. 8(a)-(c) are the same as Figs. 7(a)-(c) but for Ω = 2.561×10^{-1} rad/s. They are shown for comparison with the previous set of figures, which resemble in detailed features.

§ 5. Azimuthal structure of the basic and perturbed temperature fields and the time-dependent behavior of each Fourier mode

Fig. 9 shows the second array of probes arranged to measure the azimuthal distribution of the basic and perturbed temperature fields and the time-dependent behavior of each Fourier component. Twelve thermistor thermometers used in this array are set at the center of the channel at every 30° in the azimuthal direction with the first probe set at θ = 15° . Initially they are positioned at z = 9.0 cm and can be moved down vertically at intervals of 1 cm.

§ § 5.1. Azimuthal structure of the basic and perturbed temperature fields

In this series of experiments, the horizontal temperature difference Δ T is fixed at 5.0℃ , the normalized heights of the obstacle H/d are 0.3, 0.5 and 0.7 and the rotation rates Ω are 8.00×10^{-2} , 1.50×10^{-1}, 2.00×10^{-1}, 2.50×10^{-1} and 3.00×10^{-1} rad/s. When the rotation rate Ω are 2.50×10^{-1} and 3.00×10^{-1} rad/s, the flow is baroclinically unstable and the preferred wavenumbers are 2 and 3, respectively.

In Fig. 10(a), the stationary temperature perturbation in zonal-height sections for H/d = 0.3 and the five different Ω are shown. The stationary temperature perturbation is obtained as follows. The time mean temperature $\langle T\rangle_t$ of each probe is calculated, and then a space mean $\langle T\rangle_{t\theta}$ consisting of the

twelve $\langle T \rangle_t$ is made at each level. When $\langle T \rangle_{t\theta}$ is subtracted from $\langle T \rangle_t$, the stationary temperature perturbation $\langle T - \langle T \rangle_\theta \rangle_t$ is obtained. When the flow is baroclinically stable, a positive deviation appears on the windward side of the obstacle with a negative deviation on the lee side of the obstacle. The formation of this temperature deviation is caused by forced baroclinic waves, which will be discussed in Section 6. The stationary vortex remains trapped in the present parameter range, which is consistent with the numerical simulation by Huppert and Bryan (1976). When the flow becomes baroclinically unstable and baroclinic waves develop, the magnitude of the temperature deviation around the obstacle becomes small.

When H/d = 0.5, the structure of the stationary temperature deviation is not very different from that of H/d = 0.3, which is shown in Fig. 10(b). The horizontal extent of the temperature deviation increases, corresponding to Rossby's deformation radius (L_R = NH/f). It is reasonable that the horizontal extent of the deviation increases, accompanied by the increase of the height of the obstacle (see Fig. 10c).

In the next set of figures (Fig. 11), the amplitudes of the Fourier components of transient baroclinic waves for three obstacle heights (H/d = 0.3, 0.5 and 0.7) and for two rotation rates (Ω = 2.50×10^{-1} and 3.00×10^{-1} rad/s) are shown in azimuth-height sections.

Fig. 11(a) is for H/d = 0.3, Ω = 2.50×10^{-1} rad/s and k = 2, whose basic field was shown in the fourth panel of Fig. 10(a). For the ground mode, the maxima appear downstream near

the height of the obstacle (θ = 50° , z/d = 0.4) and at the farthest distance from the obstacle in the middle layer (θ = 180° , z/d = 0.6). The vertical profile of the ground mode is shown at two different azimuthal angles (θ = 45° and 315°). Amplification of the ground mode at θ = 45° and at the obstacle height is apparent when the profile is compared with that of θ = 315° , which has almost the same vertical profile as that of no obstacle. The second harmonic shows no change in its structure over all θ , but small maxima are observed on the lee side and at the top of the obstacle and also at about θ = 90° at the obstacle height. The third harmonic has its maximum in the upper layer and on the upstream side of the obstacle (θ = 270° , z/d = 0.8). However, the amplitude of the third harmonic is not large enough so that the dependence on θ is obscure.

Fig. 11(b) is the same as Fig. 11(a) but for H/d = 0.5, the basic field of which is shown in the fourth panel of Fig. 10(b). The gross features are almost the same as those for Fig. 11(a), but the area where amplification of the ground mode occurs extends to the leeward of the obstacle and the magnitude of the amplification increases.

Fig. 11(c) is the same as Fig. 11(a) but for H/d = 0.7. The area in which amplification of the ground mode occurs extends further, but in this case the magnitude of the amplification decreases. The amplitude of higher harmonics increases compared with those for the case of H/d = 0.5.

Fig. 12 is the same as Fig. 11, but with a rotation rate

of $\Omega = 3.00\times 10^{-1}$ rad/s and the preferred wavenumber k = 3. In this figure, the ground mode of migrating baroclinic waves is amplified near the top and on the lee side of the obstacle. The vertical profile of the ground mode has two maxima on the lee side of the obstacle (θ = 45°). Notably, when the normalized height of the obstacle is greater than 0.5, the magnitude of the lower maximum becomes larger than the upper maximum. When H/d = 0.7, the area where the amplification occurs extends upstream at the lower half of the obstacle height. The second harmonic is also amplified near the top and on the lee side of the obstacle as it was in the case of preferred wavenumber 2.

Fig. 13 shows the dependence of the normalized temperature variation of the first 15 Fourier components on the azimuthal angle θ at the obstacle height, with the parameters being $\Omega = 3.0\times 10^{-1}$ rad/s, H/d = 0.5 and k = 3. Amplification of the ground mode and second harmonic on the lee side of the obstacle is clearly shown in this figure. The temperature deviation mainly consists of the ground mode and its higher harmonics while the contribution of the sideband modes is negligibly small.

Fig. 14 shows the dependence of the normalized temperature deviation of the first 15 Fourier components on height at the azimuthal angle of θ = 45° , with the parameters being $\Omega = 3.0\times 10^{-1}$rad/s, H/d = 0.5 and k = 3. The maximum of the ground mode is found near the obstacle height (z/d= 0.4), which appeared in the upper layer with no topography as was mentioned in Section 4. The structure of the second harmonic is somewhat

complicated. In the case of no obstacle, there were two maxima, one in the upper layer the other in lower layer, with the magnitude of the former larger than the latter.

§ § 5.2. Time-dependent behavior of each Fourier mode

The time-dependent behavior of the zonal mean temperature, amplitude and phase of each Fourier component are shown in Fig. 15. Temperature data detected 1 cm above the height of the obstacle are used in this figure.

When the rotation rate Ω is 2.50×10^{-1} rad/s and the preferred wavenumber k is 2 (Fig. 15a), both the zonal mean temperature and the amplitude of the Fourier component reveal a vacillation cycle with very short period (2~ 3 rotations). This period is much shorter than the period reported by previous researchers (e.g. Pfeffer et al., 1980). This short period vacillation seems to have suffered from a long term modulation. The variation of the zonal mean temperature shows a negative correlation with that of the amplitude of each Fourier mode. The frequency of the second harmonic is almost twice as long as that of the ground mode, or the phase velocities of the ground mode and the second harmonic are almost the same. The Phase velocity of the second harmonic becomes negative at some point in time, meaning that the second harmonic retrogrades at that time.

When the rotation rate Ω is 3.00×10^{-1} rad/s and the preferred wavenumber k is 3 (Fig. 15b), the zonal mean tempera-

ture and the amplitude of the Fourier component show a more regular vacillation cycle compared with the case of wavenumber 2. The zonal mean temperature shows a negative correlation with the amplitude of the ground mode and a positive correlation with phase velocity of the ground mode.

From Fig. 5, it can be seen that an increase in the zonal mean temperature corresponds to the increase of horizontal temperature gradient at the mid channel. Therefore, it is reasonable that the horizontal temperature gradient has a negative correlation with the amplitude of the ground mode and a negative correlation with the phase velocity of the ground mode. This type of vacillation was reported by Smith and Davies (1977) and Wakata and Uryu (1984). In the numerical model of Smith and Davies (1977), the variation of eddy kinetic energy and zonal kinetic energy oscillated with a period of about 5 days and were negatively correlated.

§ 6. Forced baroclinic waves due to orography: linear theory

The structure of forced baroclinic waves is discussed with linear perturbation theory and is compared with the experimental results. Considering an incompressible Boussinesq fluid on a f-plane with bottom topography, the hydrostatic and the quasi-geostrophic flow approximation are made. For simplicity, it is assumed that the topography is independent of the meridional direction. Then, conservation of potential vorticity leads to the following perturbation equation for pressure p:

$$\left(\frac{\partial}{\partial t}+U\frac{\partial}{\partial x}\right)\left[\frac{\partial^2 p}{\partial z^2}+\frac{N^2}{f^2}\left(\frac{\partial^2 p}{\partial x^2}+\frac{\partial^2 p}{\partial y^2}\right)\right]=0, \tag{1}$$

with the boundary conditions

$$-\frac{1}{\rho_0 N^2}\frac{\partial}{\partial z}\left(\frac{\partial p}{\partial t}+U\frac{\partial p}{\partial x}\right)+\frac{1}{\rho_0 N^2}\frac{dU}{dz}\frac{\partial p}{\partial x}=\frac{1}{f\rho_0}\sqrt{\frac{2\nu}{f}}\frac{\partial^2 p}{\partial x^2}+U\frac{\partial H}{\partial x} \tag{2}$$

at z=0, and

$$-\frac{\partial}{\partial z}\left(\frac{\partial p}{\partial t}+U\frac{\partial p}{\partial x}\right)+\frac{dU}{dz}\frac{\partial p}{\partial x}=0 \tag{3}$$

at z=d, with

$$p=0 \tag{4}$$

at y=0,D,

where

$$N^2 = -\frac{g}{\rho_0}\frac{d\langle\rho\rangle}{dz}$$

is the Brunt-Väisälä frequency.

The boundary conditions (2),(3) and (4) are chosen in order to be similar to the experimental conditions, i.e. the top boundary is free and the bottom and sidewall boundaries are rigid. Ekman pumping and the orography with wavenumber k_o are assumed at the bottom boundary. If the sinusoidal solution of the form

$$p = \hat{p}(z)\ sin\left(\frac{\pi y}{D}\right)\ exp\,(ikx) \tag{5}$$

is assumed, Eq. (1) can be rewritten

$$\frac{d^2\hat{p}}{dz^2} + \frac{N^2}{f^2}(k^2+l^2)\hat{p} = 0 \tag{1'}$$

where $l = \pi/D$.

The solution of Eq. (1') with the boundary conditions (2) and (3) is readily obtained as

$$p = \frac{4kU(0)\hat{H}}{\rho_0\Gamma}\left[-\frac{k\lambda}{N^2}sinh\,(\lambda d) + i\frac{D_t}{f}(k^2+l^2)\ cosh\,(\lambda d)\right]$$
$$cosh\,\lambda(d-z)\ sin\,(ly)\ exp\,(ikx), \tag{6}$$

where

$$\lambda^2 = \frac{N^2}{f^2}(k^2+l^2),$$

$$D_t = \sqrt{\frac{2\nu}{f}},$$

and

$$\Gamma = [exp(\lambda d) + exp(-\lambda d)]\left[\frac{D_t}{f}(k^2+l^2)\right] + [exp(\lambda d) - exp(-\lambda d)]\left(\frac{k\lambda}{\rho_0 N}\right)^2 .$$

The density perturbation can be calculated from the pressure perturbation by making use of the hydrostatic relation as

$$\rho = \frac{4k\lambda U(0)H}{\rho_0 g \Gamma}\left[-\frac{k\lambda}{N^2} sinh(\lambda d) + i\frac{D_t}{f}(k^2+l^2)\, cosh(\lambda d)\right] sinh\,\lambda(d-z)\, sin(ly)\, exp(ikx) . \quad (7)$$

The rectangular shaped bottom topography is analyzed by a Fourier series up to the 150th component. The contribution to the pressure and density perturbation of each Fourier component are calculated by Eq. (6) and (7), forming a summation to the 150th component. The Brunt-Väisälä frequency N is obtained, based on the temperature measurement assuming a linear dependence of density with height z. The zonal velocity U(z) is obtained, based on the temperature measurement and surface flow velocity assuming a linear dependence of density in the meridional direction while making use of the thermal wind relation and the hydrostatic approximation. A few examples of the results given by this calculation are shown in Fig. 16 for a horizontal temperature difference of $\Delta T = 5℃$, Coriolis parameter f = 0.16, 0.3, 0.4, 0.5 and 0.6 and the nondimensional obstacle height H/d = 0.5. This figure can be compared with Fig. 10(b). When f = 0.16 and 0.3, a warm region is formed on the upstream side of the obstacle while a cold region is formed on the lee side of and above the obstacle (Fig. 16a,

b). The magnitude of the cold deviation is about twice as large as that of the warm deviation. When f is 0.4, the maxima of the temperature deviation appear also at the upper boundary. The value of the cold deviation around the obstacle is almost the same as that of the warm deviation, and it is larger than the value of the maximum at the upper boundary. When f = 0.5 and 0.6, the structure around the obstacle is almost the same as the previous cases while the values of the maxima around the obstacle become smaller than those at the upper boundary, and the overall structures show somewhat complicated features. The qualitative behavior of forced baroclinic waves is well simulated by linear perturbation theory, except for the maxima at the upper boundary which are not observed in the laboratory experiments. However, qauntitatively the magnitudes of the disturbances are overestimated by one order at the most. This result may be due to the use of the zonal velocity at the bottom in solutions (6) and (7).

§ 7. Vertical structure

Fig. 17 shows the placement of the third array of thermistor thermometers for measuring the vertical structure and the time sequence of baroclinic waves. Twelve probes are separated into four groups, which are placed at the azimuthal angle θ = -45° , -15° , 15° and 45° along the mean radius. Each group consists of three probes, which are set at the nondimensional heights z/d = 0.2, 0.5 and 0.8. The vertical resolution of this array is not sufficient enough, but does satisfy the obtaining of a rough vertical structure.

Fig. 18(a) shows the phase line of the ground mode and second harmonic of the temperature deviation at the four different azimuthal angles relative to the obstacle, with the rotation rate $\Omega = 2.50 \times 10^{-1}$ rad/s and the preferred wave number k = 2. The upper panel of this figure is the case of no obstacle and azimuthal angle θ only shows the relative position of each thermistor group. The vertical structure of the ground mode shows a typical structure of baroclinically unstable waves, but that of second harmonic does not. This means that the second harmonic is not baroclinically unstable but is forced by the ground mode. One of the experimental results by Rao and Ketchum (1975) also has the same structure as the present case, namely the phase lines of the ground mode and the second harmonic show an eastward tilt contrary to those of the third and the fourth harmonic which show a westward tilt. On the upstream side of the obstacle (θ = -15° , -45°),

the ground mode has almost the same structure as that of no obstacle , except that the tilt of the phase line becomes steep in the lower layer for the case of H/d = 0.7 and θ = -15° . On the downstream side of the obstacle, as the height of the obstacle increases the extent of the deformed area becomes larger. For instance, the vertical structure almost recovers at θ = 45° for the case of H/d = 0.3, but when H/d = 0.7 it has not recovered yet at θ = 45° and phase line tilts westward. For the second harmonic, deformation of the vertical structure occurs on the downstream side of the obstacle, but the deformation is small and does not appear as essential as that of the ground mode.

Fig. 18(b) is the same as Fig. 15(a) but for the rotation rate of $\Omega = 3.00\times 10^{-1}$ rad/s and preferred wave number k = 3. Variation in the vertical structure passing around the obstacle is almost the same as that of the previous case.

Fig. 19 presents an example of time sequence of a phase line where the parameters are $\Omega = 3.00\times 10^{-1}$ rad/s, k = 3 and H/d = 0.5. The ground mode and the second harmonic barely change their vertical structure and appear to have an almost constant frequency. From this figure, it can be concluded that the vertical structure shown in Fig. 18 is not temporal but an almost steady one.

§ 8. Summary and discussions

The mechanism of the amplification of baroclinic waves on the lee side of the obstacle is discussed more precisely in the following. Fig. 20 shows the schematic plan view of the idealized basic temperature field based on the results of the laboratory experiments and the linear theory. The amplitude of the skewed basic field due to the obstacle is settled on 20% of the horizontal temperature difference, which is the reasonable value compared with the experimental results. As the result of the deformation of the basic temperature field, two regions which have large horizontal temperature gradient (region A and B) are produced. The region A located in the northwest part of the obstacle is characterized by the increased horizontal temperature gradient and the diminished static stability, while the region B located in the southeast part of the obstacle is characterized by the increased horizontal temperature gradient and the increased static stability. The growth rates and phase velocities of baroclinic waves at these regions and the reference area S, not disturbed by forced baroclinic waves, are calculated using the following formulae deduced by the linear perturbation theory:

$$kc_i = \frac{k\Lambda}{\lambda}\sqrt{\left|1-\frac{\lambda^2 d^2}{4}-\lambda d\ coth\,(\lambda d)\right|} \tag{8}$$

$$c_r = \frac{U(0)+U(d)}{2}. \tag{9}$$

where U(0) and U(d) are the basic zonal velocity at the bottom and the upper boundary. The results are shown in Fig. 21, in which the field values N, f and Λ in the expressions (8) and (9) are based on the results of laboratory experiments. The magnitude of the temperature deviation around the obstacle is assumed to be 40% of the horizontal internal temperature difference, which is somewhat overestimated on the upstream side of the obstacle. The growth rates of the region A and B become 1.54 and 1.28 times of that of the reference region S, respectively. This remarkable change of the growth rate around the obstacle clearly shows the mechanism of lee cyclogenesis. The most preferred wavenumber of the region A shifts to the higher wavenumber than that of the region S, while the most preferred wavenumber of the region B shifts to the lower wavenumber. The change of the wavenumber around the obstacle agrees qualitatively well with the behavior of observed baroclinic waves, namely the elongation of baroclinic waves occurs on the lee side of the obstacle and shortening occurs on the upstream side of the obstacle.

Now the results of the preceding sections are summarize as follows: 1) The topography in a baroclinic flow causes forced baroclinic waves accompanied by a skewed basic temperature field. 2) The temperature structure of stationary vortices has a warm region formed on the upstream side of the obstacle with a cold region located on the lee side of the obstacle. 3) The stationary vortex transfers heat from the outer to the inner wall and as a result it moderates the horizontal temperature

gradient. 4) For the marginal wavenumber with no topography, the transition from a baroclinically stable to unstable flow occurs at a lower thermal Rossby number, that is, the topography has a stabilizing effect. 5) In the present experiment, the cylindrical obstacle causes baroclinic waves with wavenumber 1, which do not appear without the obstacle. The thermal Rossby number at which they appear is larger than the critical thermal Rossby number with no topography. 6) Due to the skewed temperature field or enhanced baroclinicity, the growth rate of baroclinic waves increases around the obstacle and the amplification of baroclinic waves is observed on the lee side of the obstacle. This phenomenon of lee cyclogenesis in the skewed basic temperature field is consistent with the theories of Niehaus (1980) and Frederiksen (1979).

Acknowledgment

The author wishes to extend his sincere thanks to Professors M. Uryu and T. Takahashi for their critical reading and stimulating discussions of this manuscript. Thanks are also due to Professor S. Miyahara for his critical reading of this manuscript and his valuable advice on devising the electronic measuring system.

Appendix A

Notations

a	inner radius of the annulus
b	outer radius of the annulus
d	fluid depth of the working fluid
Ω	rotation rate
f	($=2\Omega$) Coriolis parameter
ΔT	imposed horizontal temperature difference
T_o	mean temperature between outer and inner walls
k	preferred wavenumber
k_o	wavenumber of the obstacle
H	height of the obstacle
H_T	height of thermistor thermometers
(r, θ, z)	cylindrical coordinate
	$\theta = 0$ is taken at the center of the obstacle
m	m-th Fourier component of baroclinic waves
$\langle T \rangle_\theta$	zonal mean temperature
T'	temperature deviation from $\langle T \rangle_\theta$
$\langle T \rangle_t$	time mean temperature
T''	temperature deviation from $\langle T \rangle_t$
$T^* = T/\Delta T$	normalized temperature
ρ_o	mean density of the working fluid
$\langle \rho \rangle_\theta$	zonal mean density
$\Delta \rho$	density difference corresponding to ΔT
ρ'	density deviation from $\langle \rho \rangle_\theta$
ν	kinematic viscosity of the working fluid at T_o

μ thermal conductivity of the working fluid at T_o

κ thermal diffusivity of the working fluid at T_o

g gravitational acceleration

Q heat flow from outer to inner wall

N $\left(=\sqrt{\frac{\Delta \rho g}{\rho_o d}}\right)$ Brunt-Väisälä frequency

U(z) zonal velocity

Λ $\left(=\frac{dU}{dz}\right)$ vertical shear of zonal velocity

And nondimensional parameters constructed from dimensional parameters above are as follows:

Θ $\left(=\frac{\Delta \rho g d}{\rho_o \Omega^2 (b-a)^2}\right)$ thermal Rossby number

Ta $\left(=\frac{4\Omega^2 (b-a)^5}{\nu^2 d}\right)$ Taylor number

Pr $\left(=\frac{\nu}{\kappa}\right)$ Prandtl number

Nu $\left(=\ln\left(\frac{b}{a}\right)\frac{Q}{2\pi \mu d \Delta T}\right)$ Nusselt number.

Appendix B

The structure of waves with wavenumber 1

The structure of waves consisting of the wavenumber 1 component was measured using the same system as described in Section 7. Experimental parameters are as follows: $\Delta T = 5.13℃$, $\Omega = 2.218 \times 10^{-1}$ rad/s, $H/d = 0.8$, $\Theta = 1.824$ and $Ta = 1.313 \times 10^{7}$. From Fig. 2(a), it is apparent that this parameter range corresponds to the domain which quasi-stationary waves of wavenumber 1 most frequently appear. Fig. B1 shows the amplitude and the phase line for each Fourier component (from the ground mode to the fourth harmonic) of the temperature deviation at a given instance. Both the amplitude and the phase line show the characteristic structure of unstable baroclinic waves, i.e. the maximum amplitude occurring at mid depth and the forward tilt of the phase line. In Fig. B2, it is shown that this vertical structure is not temporal but quasi-stationary. This is especially true for the structure of the ground mode and the second harmonic which dose not change throughout the experiment. However, the third harmonic does show a temporal change of its structure.

References

Bowden, M and H.F. Eden, 1965: Thermal convection in a rotating fluid annulus: Temperature, heat flow and flow field observations in the upper symmetric regime. J. Atmos. Sci., **22**, 185-195.

Boyer, D. and R.-R. Chen, 1987: Laboratory simulation of mechanical effect of mountains on the general circulation of the Northern Hemisphere: uniform shear background flow. J. Atmos. Sci., **23**, 3552-3574.

Cehelsky, P. and K.K. Tung, 1987: Theories of multiple equilibria and weather regimes - A critical reexamination. Part II : baroclinic two layer models. J. Atmos. Sci., **44**, 3232-3303.

Eady, E.T., 1949: Long waves and cyclone waves. Tellus, **1**, 33-52.

Frederiksen, J.S., 1979: The effects of long planetary waves on the regions of cyclogenesis: Linear theory. J. Atmos. Sci., **36**, 195-204.

Gent, P.R. and Leach, H., 1976: Baroclinic instability in an eccentric annulus. J. Fluid Mech., **77**, 769-788.

Huppert, H.E., 1975: Some remarks on the initiation of internal Taylor columns. J. Fluid Mech., **67**,397-412.

Huppert, H.E. and K. Bryan, 1976: Topographycally generated eddies. Deep-Sea Res., **23**, 655-679.

Jonas, P.R., 1981: Laboratory observations of the effect of topography on baroclinic instability. Quart. J. Roy. Met. Soc., **107**, 775-792.

Kaiser, J.A.C., 1969: Rotating deep annulus convection I: thermal properties of the upper symmetric regime. Tellus, **21**, 789-805.

Kaiser, J.A.C., 1970: Rotating deep annulus convection part 2. Wave instabilities, vertical stratification and associated theories. Tellus, **22**, 275-287.

Kaiser, J.A.C., 1971: Heat transfer by symmetric annulus convection. J. Atmos. Sci., **28**, 929-932.

Ketchum, C.B., 1972: An experimental study of baroclinic waves at large Taylor number. J. Atmos. Sci., **29**, 665-679.

Manabe, S. and T.B. Terpstra, 1974: The effects of topography on the general circulation of the atmosphere as identified by numerical experiments. J. Atmos. Sci., **31**, 3-42.

McIntyre, M.E., 1968: The axisymmetric convective regime for a rigidly bounded rotating annulus. J. Fluid Mech., **32**, 625-655.

Niehaus, M.C.W., 1980: Instability of non-zonal baroclinic flows. J. Atmos. Sci., **37**, 1447-1463.

Pfeffer, R.L., G. Buzyna and R. Kung, 1980: Time-dependent modes of behavior of thermally driven rotating fluids. J. Atmos. Sci., **37**, 2129-2149.

Proudman, J., 1916: On the motion of solids in a liquid possessing vorticity. Proc. Roy. Soc., **A92**, 408-424.

Rao, S.T. and C.B. Ketchum, 1975: Spectral characteristics of the baroclinic annulus waves. J. Atmos. Sci., **32**, 698-711.

Smith, R.F.T. and D.R. Davies, 1977: A note on some numerical experiments with model mountain barriers. Tellus, **29**, 97-106.

Taylor, G.I., 1917: Motion of solids in fluids when the flow is not irrotational. Proc. Roy. Soc., **A93**,99-113.

Uryu, M., O. Morita, N. Noguchi and R. Sawada, 1974: Heat transport in a rotating fluid annulus. J. Meteor. Soc. Japan, **52**, 93-105.

Wakata, Y. and M. Uryu, 1984: Non-linear behaviors of forced baroclinic wave in a continuous zonal flow. J. Meteor. Soc. Japan, **62**, 809-832.

Williams, G.P., 1967: Thermal convection in a rotating fluid annulus: Part I. The basic axisymmetric flow. J. Atmos. Sci., **24**, 144-161.

Yeh, T.-C. and C.-C. Chang, 1974: A preliminary experimental simulation on the heating effect of the Tibetan Plateau on the general circulation over Eastern Asia in summer. Scientia Sinica, **17**, 397-420.

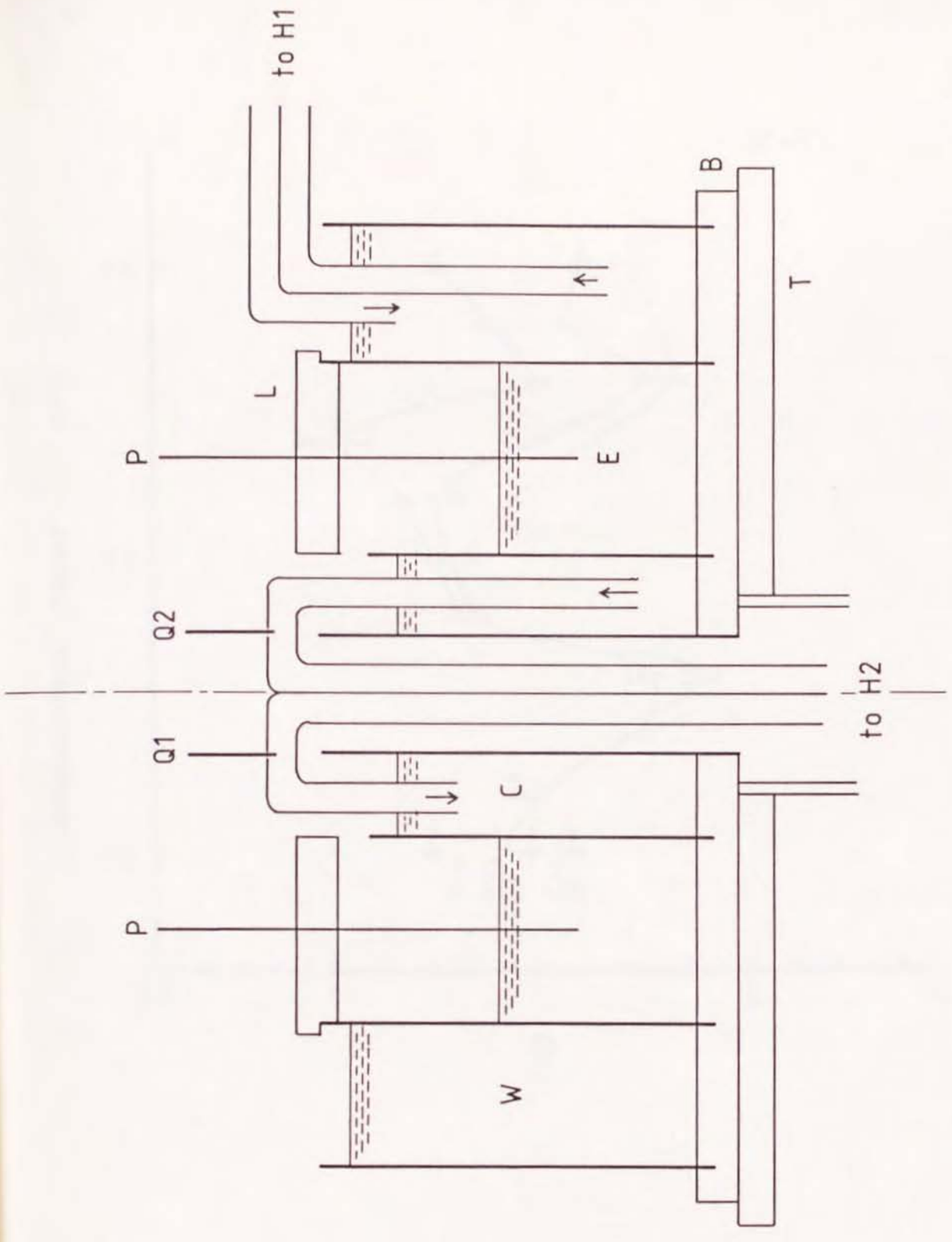

Fig. 1 Experimental apparatus. E:experimental chamber (working fluid), B: acrylic base, L: acrylic lid, P: thermistor thermometer, Q1, Q2: thermistor thermometers for heat flow measurement, C: cool water, W: warm water

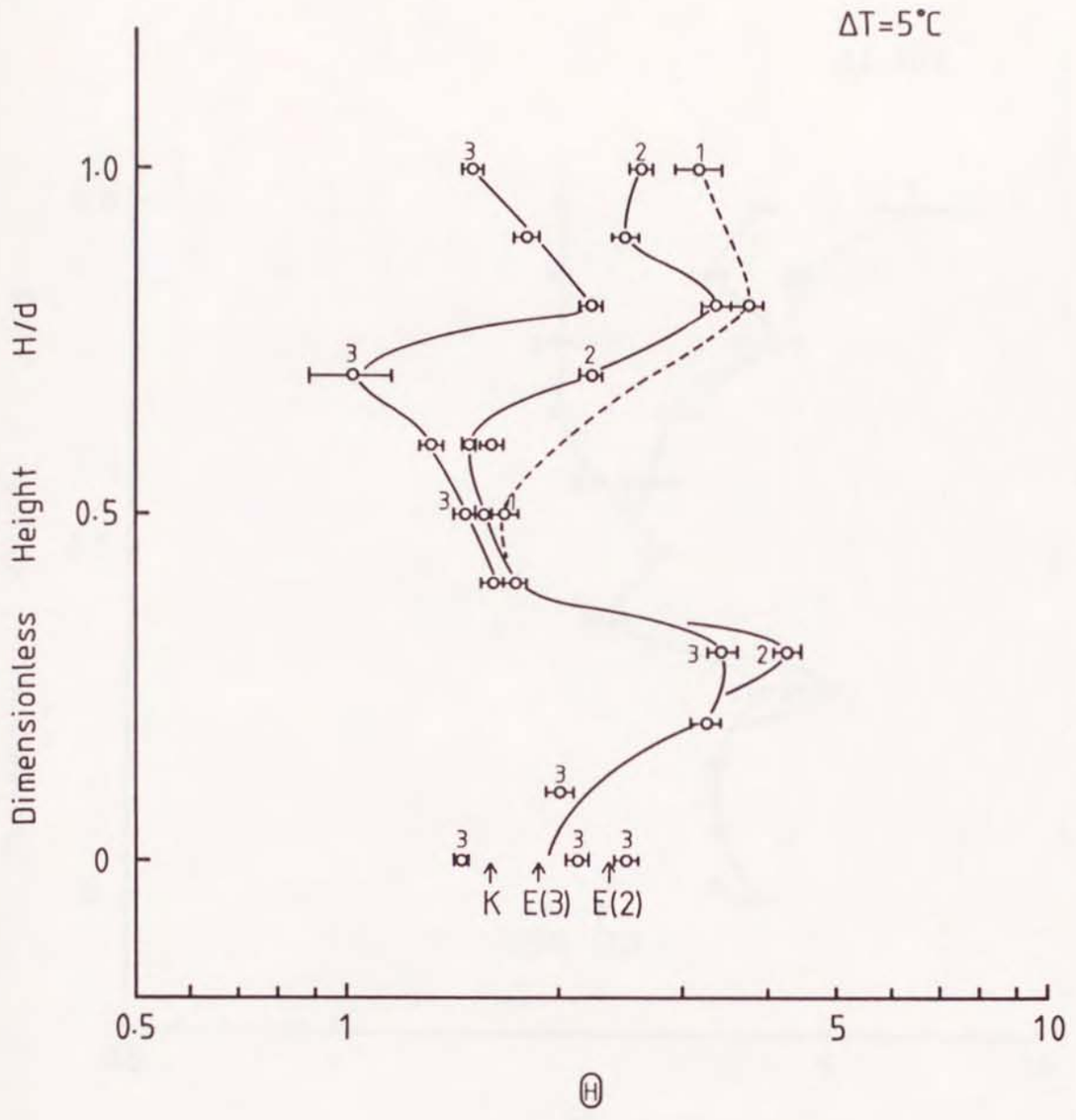

Fig. 2(a) Transition curve from baroclinically stable to unstable flow, where the horizontal temperature difference Δ T is 5℃ .

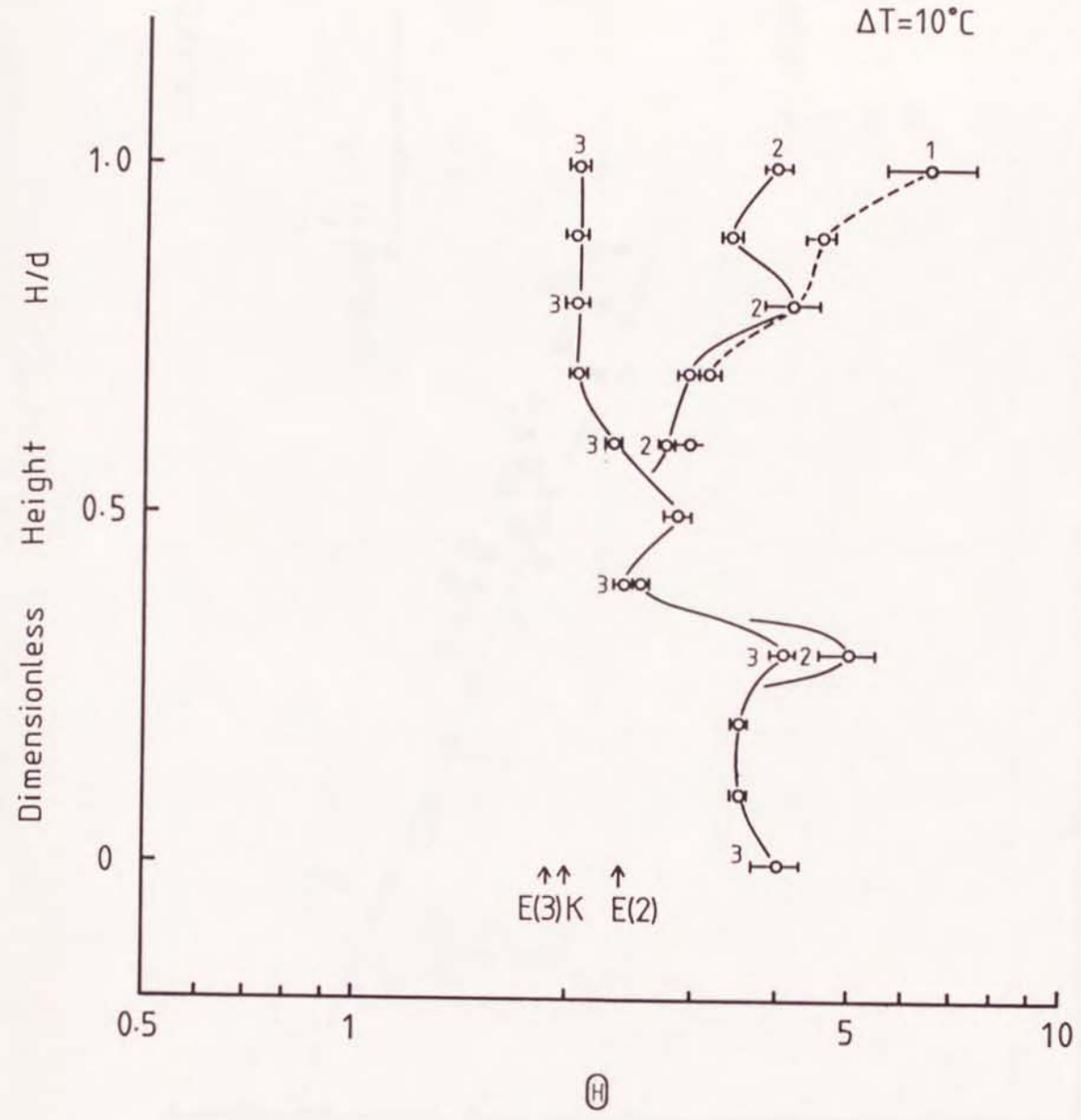

Fig. 2(b) Same as Fig. 2(a) but for $\Delta T = 10°C$.

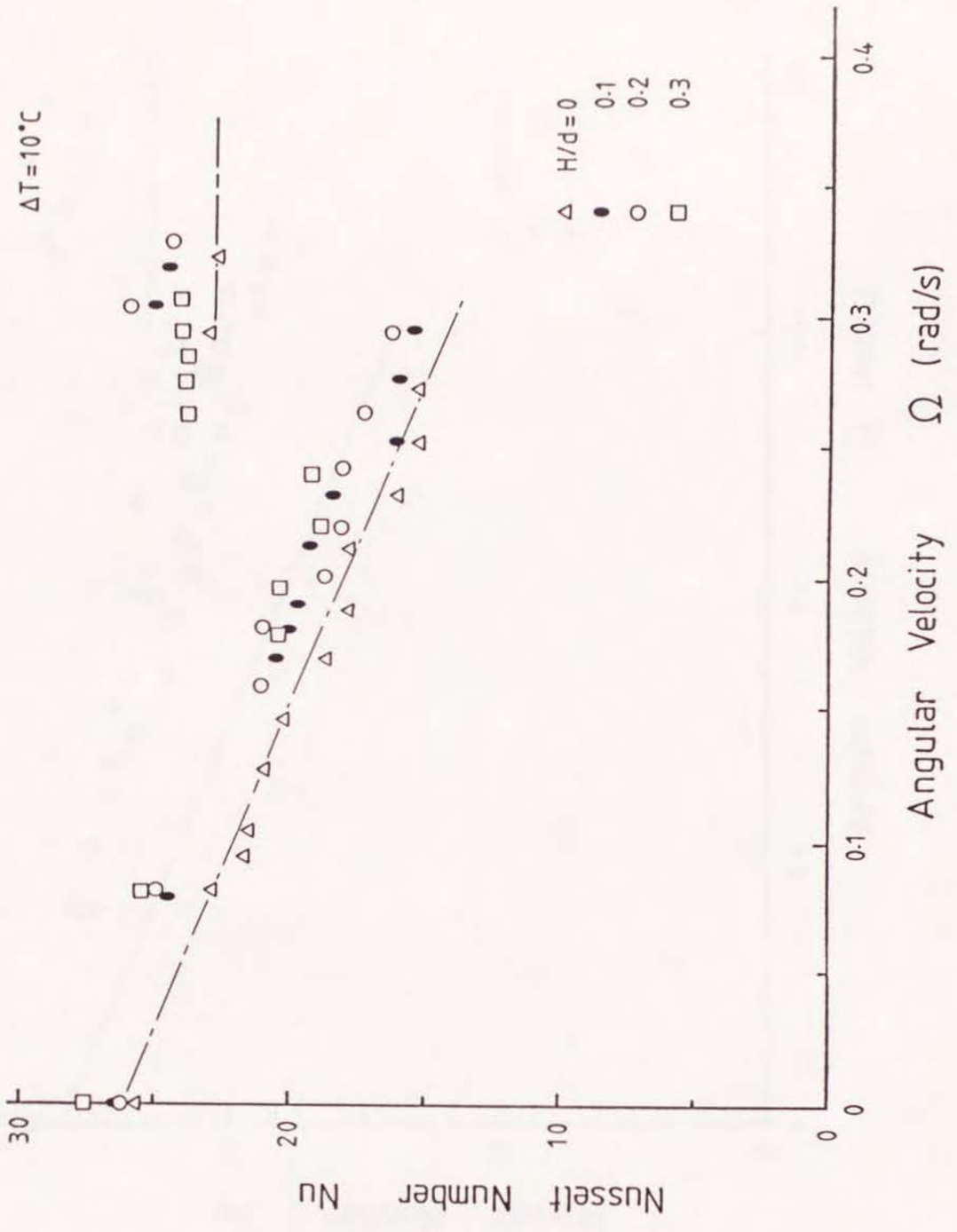

Fig. 3(a) Dependence of normalized heat flow Nu on the rotation rate Ω , where H/d = 0, 0.1, 0.2 and 0.3. The dashed line is the heat flow with no topography.

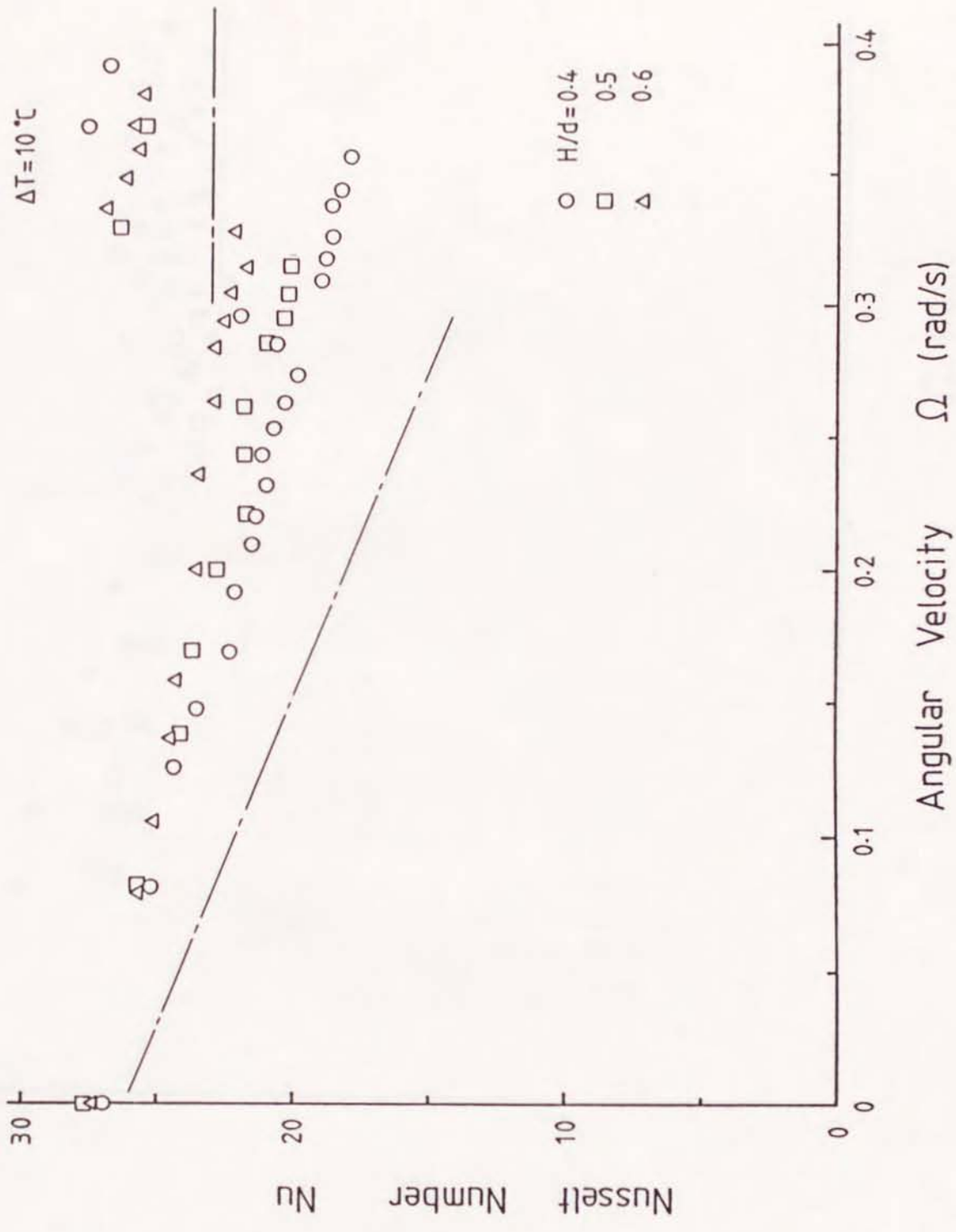

Fig. 3(b) Same as Fig. 3(a) but for H/d = 0.4, 0.5 and 0.6.

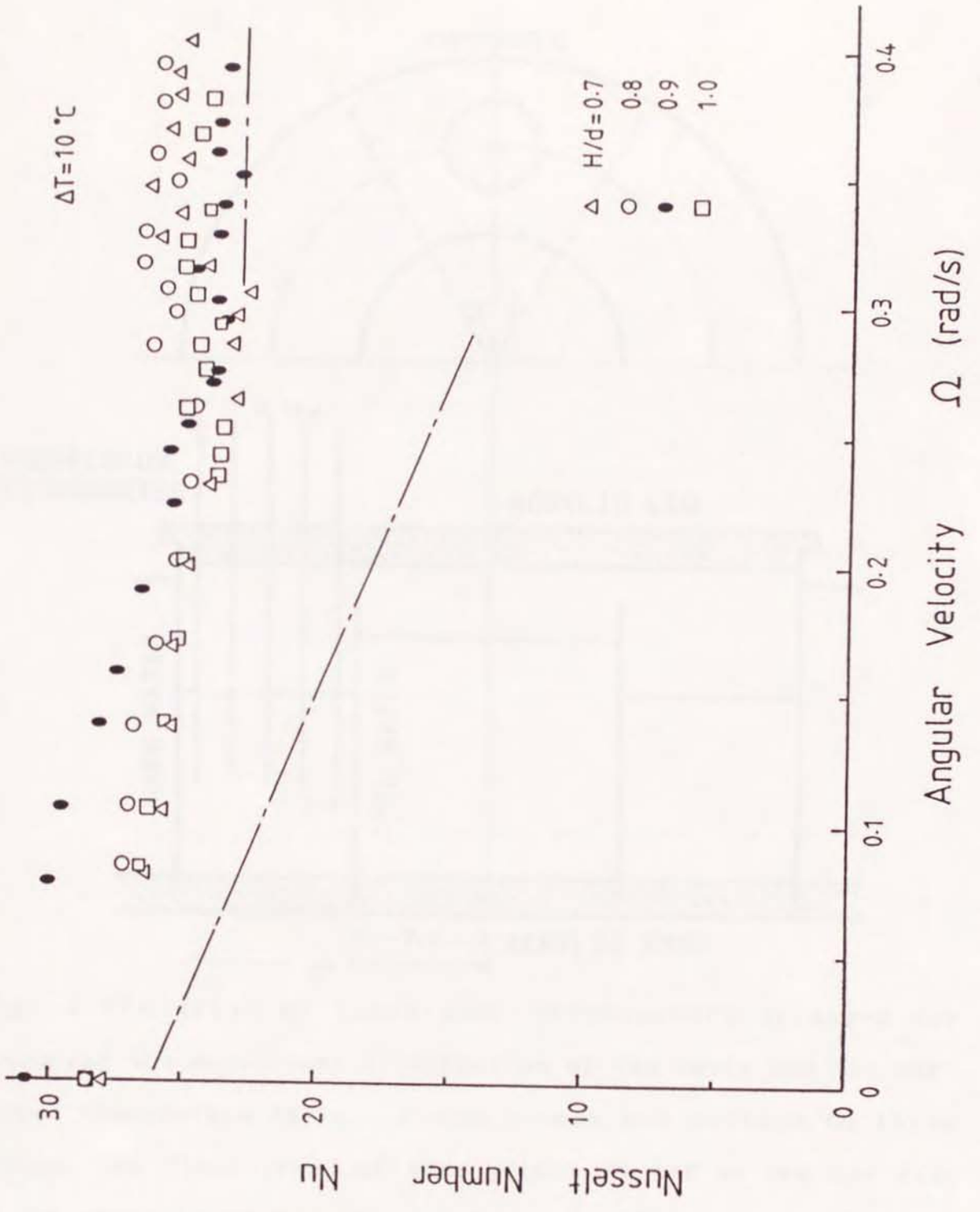

Fig. 3(c) Same as Fig. 3(a) but for H/d = 0.7, 0.8, 0.9 and 1.0.

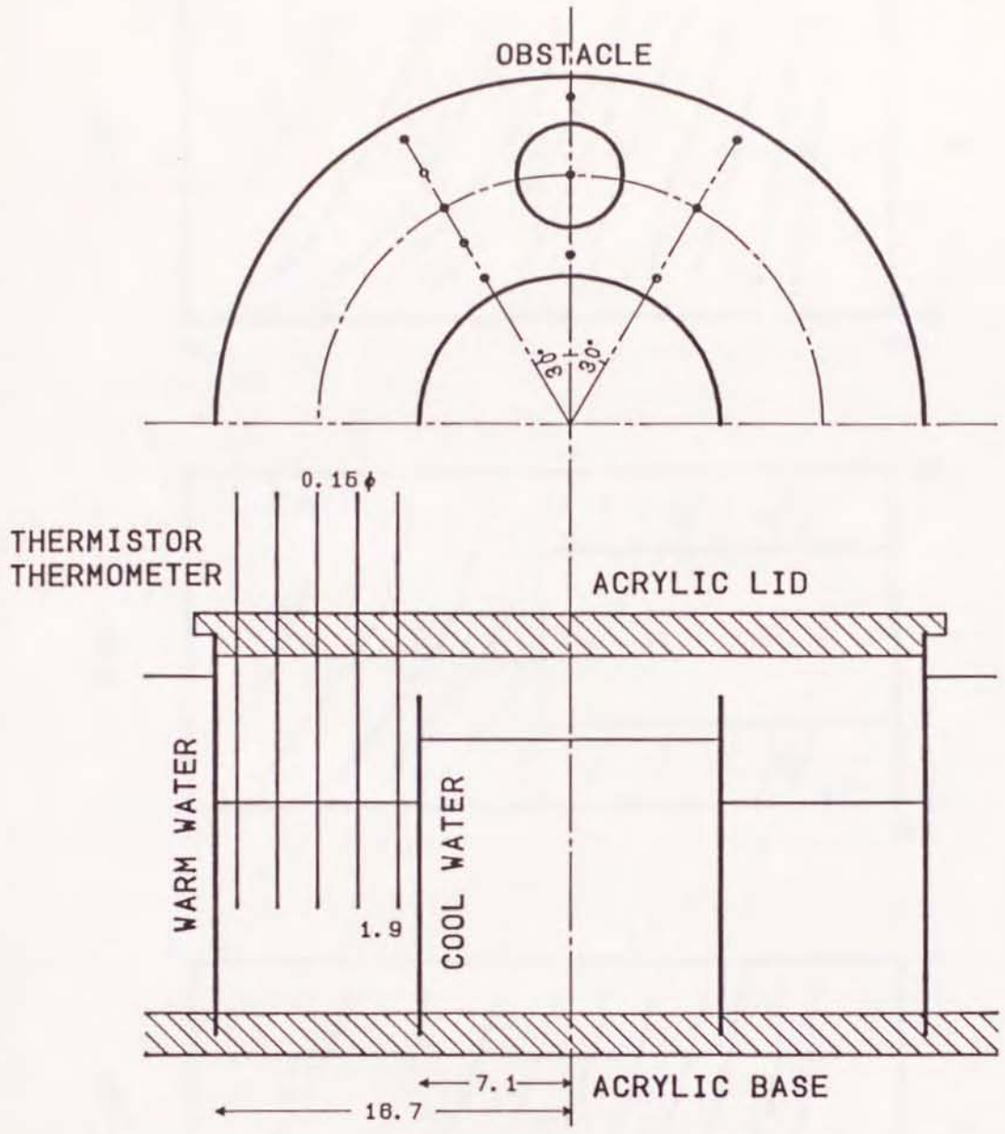

Fig. 4 The array of thermistor thermometers arranged for measuring the meridional distribution of the basic and the perturbed temperature field. Eleven probes are divided to three groups, the first group of five probes is set on the lee side of the obstacle at θ = 30° and r = 8.1, 10.0, 11.9, 13.8 and 15.7 cm, the second group of three probes is placed just above the obstacle at θ = 0° and r = 8.1, 11.9 and 15.7 cm, and the third group of three probes is located on the upstream side of the obstacle at θ = -30° and r = 8.1, 11.9 and 15.7 cm.

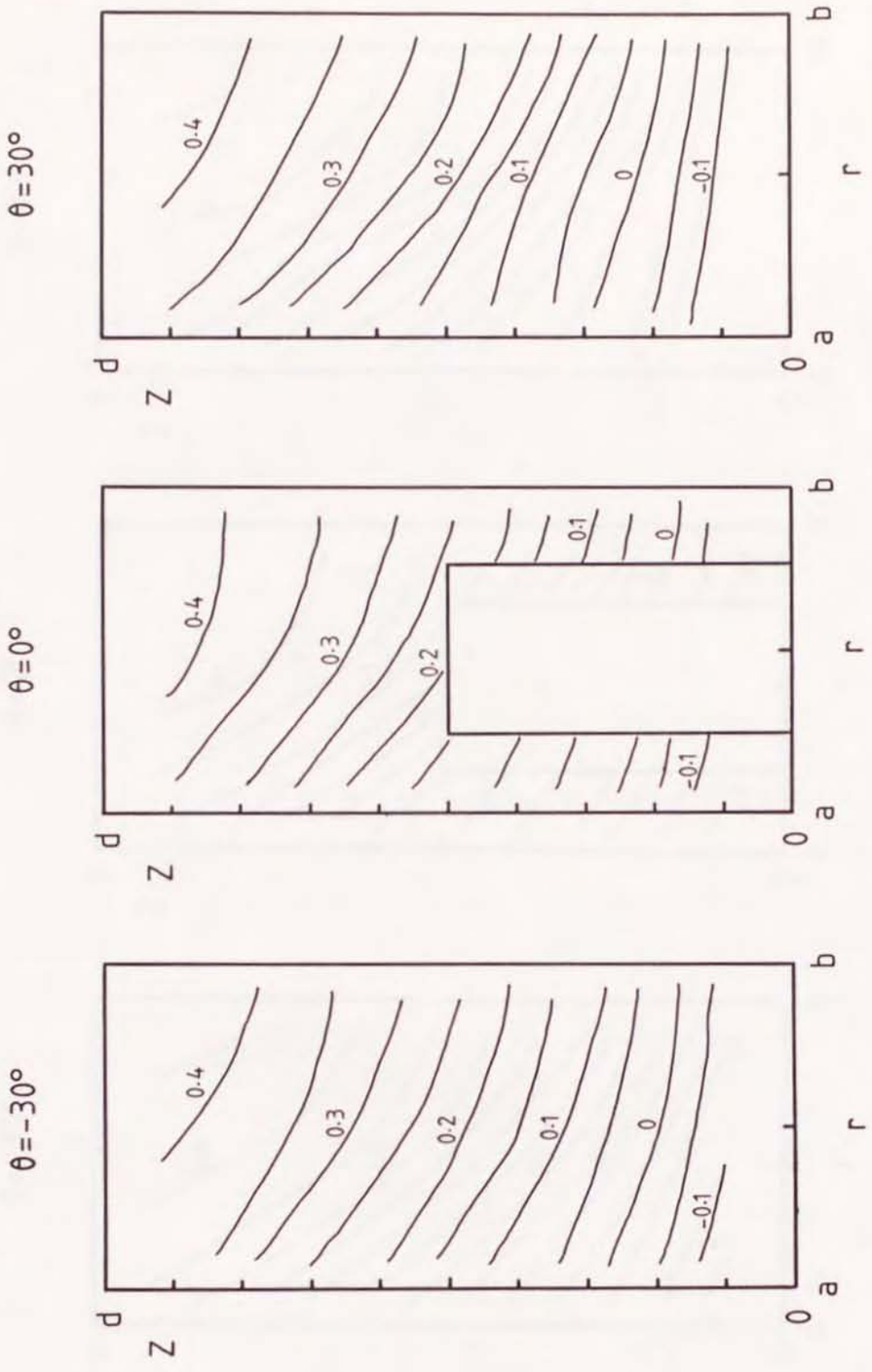

Fig. 5(a) Normalized time-mean temperature at three different azimuthal positions (θ = -30° , 0° , 30°) for the rotation rates $\Omega = 8.08\times 10^{-2}$ rad/s with T_o as the reference temperature. Numerals in the figures are $\langle T\rangle^{*}_{t}-T^{*}_{o}$ multiplied by 100.

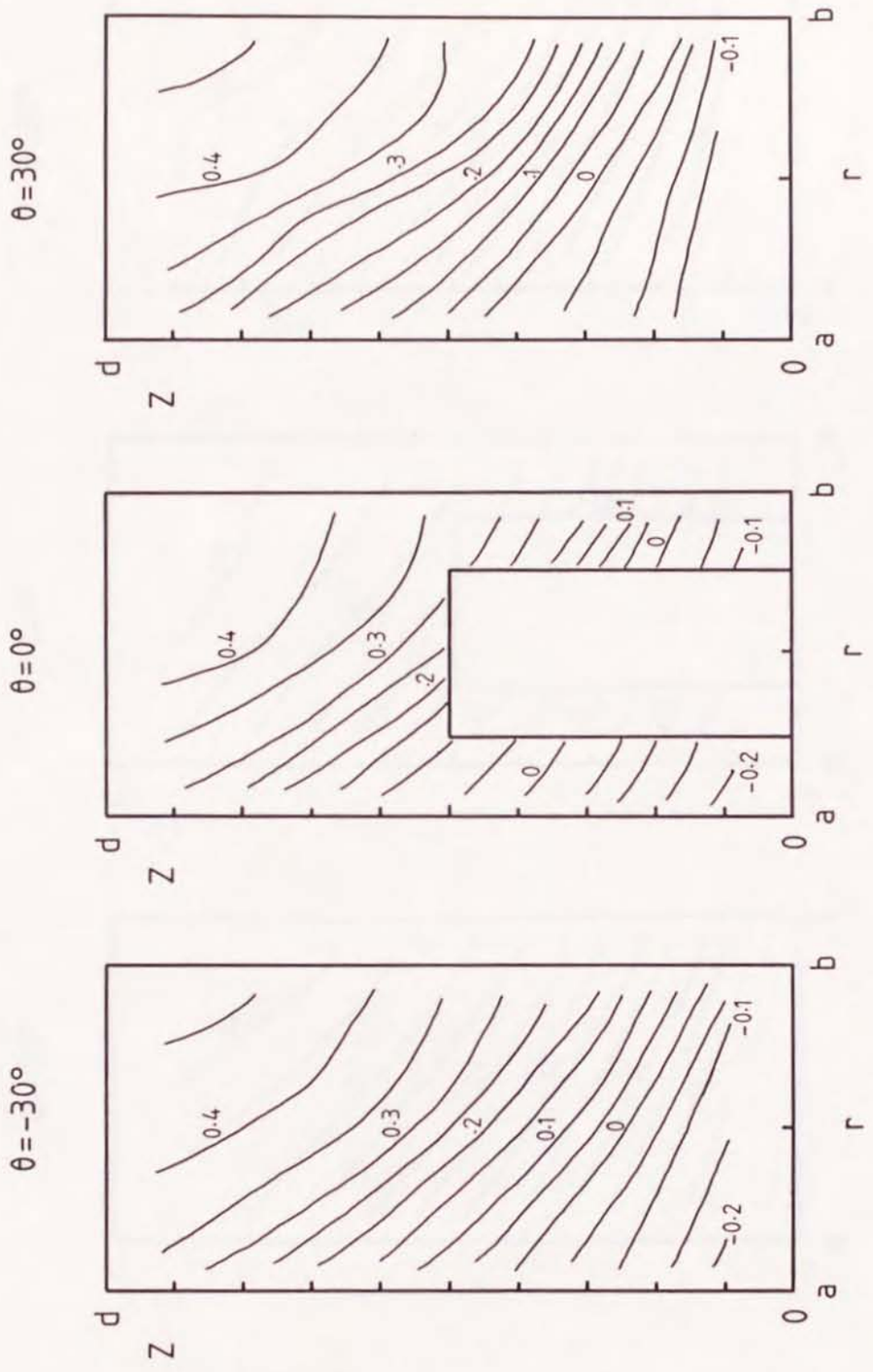

Fig. 5(b) Normalized time-mean temperature at three different azimuthal positions (θ = -30° , 0° , 30°) for the rotation rates Ω = 1.506×10^{-1} rad/s with T_o as the reference temperature. Numerals in the figures are $\langle T\rangle^{*}_{t}-T^{*}_{o}$ multiplied by 100.

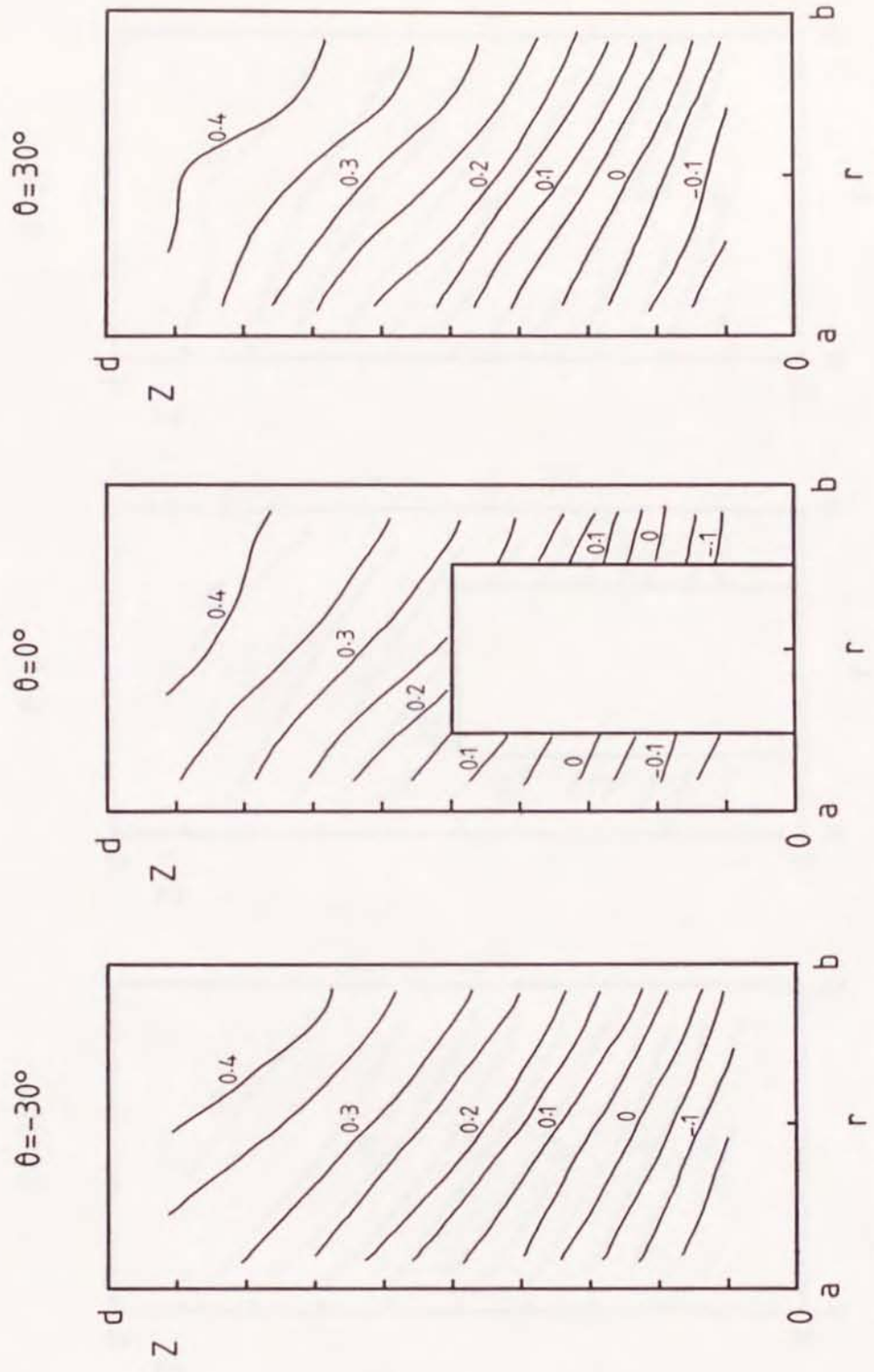

Fig. 5(c) Normalized time-mean temperature at three different azimuthal positions (θ = -30° , 0° , 30°) for the rotation rates $\Omega = 2.027\times 10^{-1}$ rad/s with T_o as the reference temperature. Numerals in the figures are $\langle T\rangle^{*}_{t}-T^{*}_{o}$ multiplied by 100.

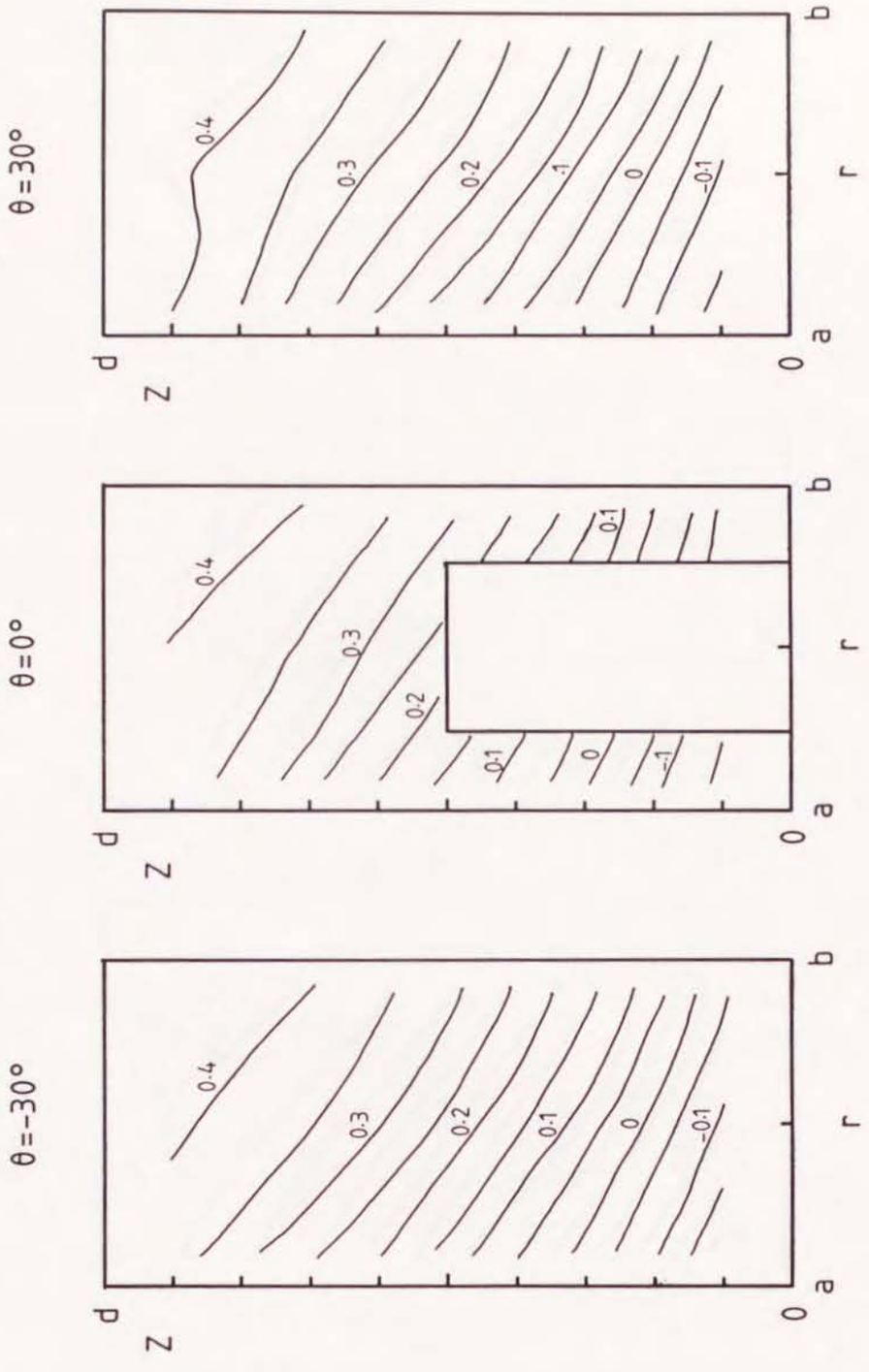

Fig. 5(d) Normalized time-mean temperature at three different azimuthal positions (θ = -30° , 0° , 30°) for the rotation rates $\Omega = 2.561 \times 10^{-1}$ rad/s with T_o as the reference temperature. Numerals in the figures are $\langle T \rangle^{*}_{t} - T^{*}_{o}$ multiplied by 100.

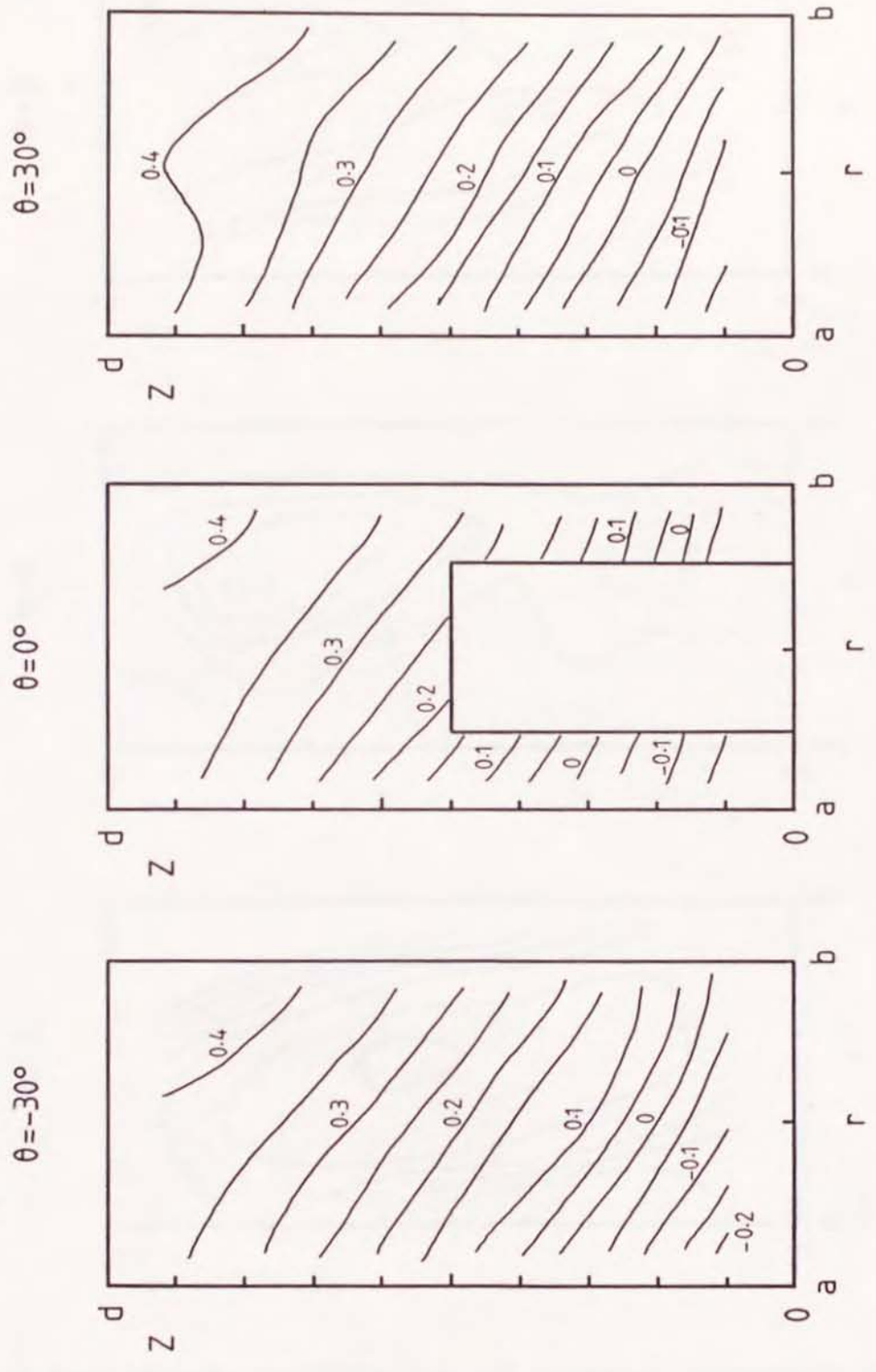

Fig. 5(c) Normalized time-mean temperature at three different azimuthal positions (θ = -30° , 0° , 30°) for the rotation rates Ω = 2.907×10^{-1} rad/s with T_o as the reference temperature. Numerals in the figures are $\langle T\rangle^{*}_{t}-T^{*}_{o}$ multiplied by 100.

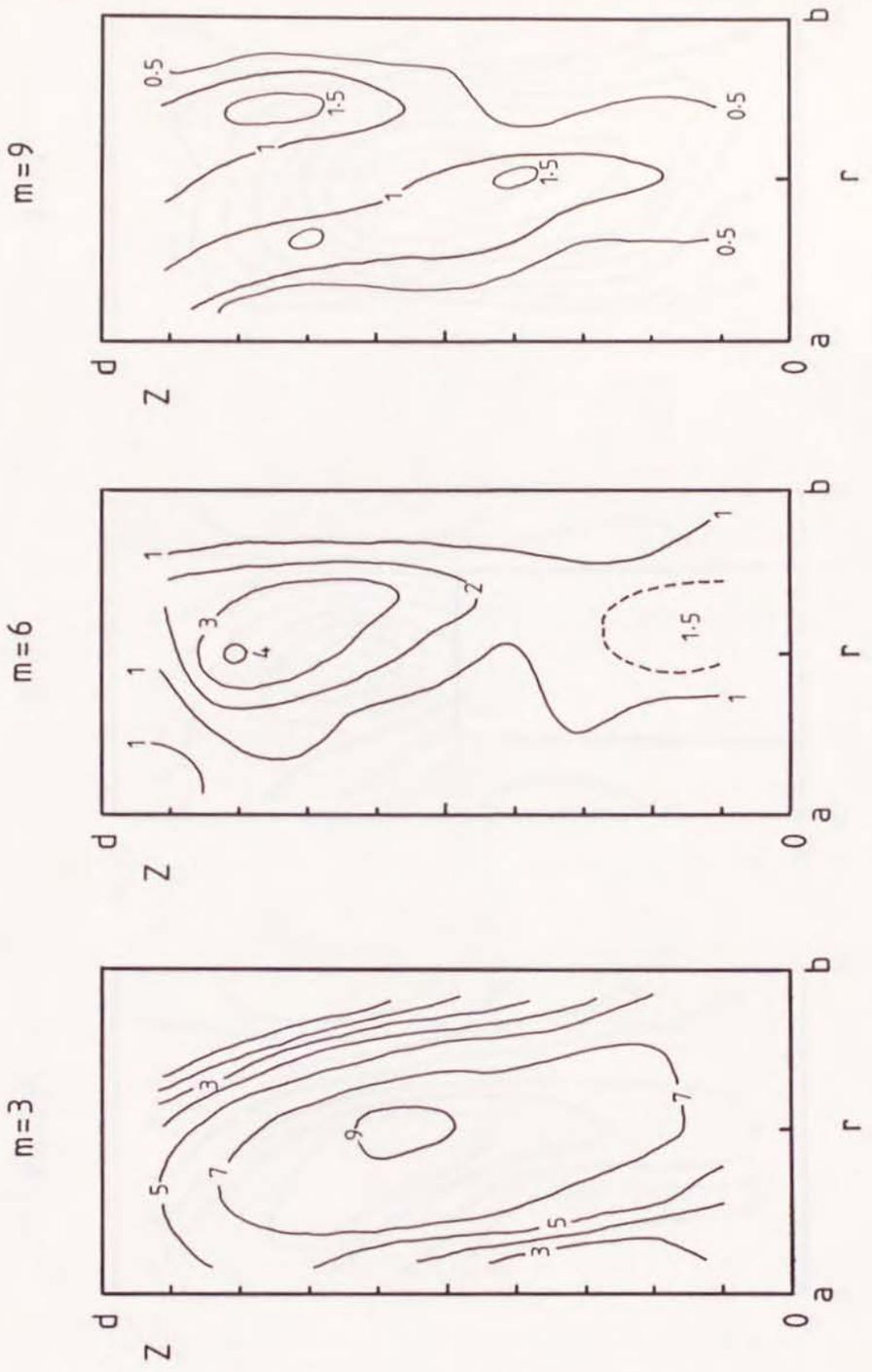

Fig. 6 Meridional distribution of Fourier components m = 3, 6 and 9 of the normalized temperature perturbation, analyzed during one period, for the case of no obstacle. Here Ω = 2.923×10^{-1} rad/s, ΔT = 5.47℃ and k = 3. Numerals in the figure are T"" multiplied by 100.

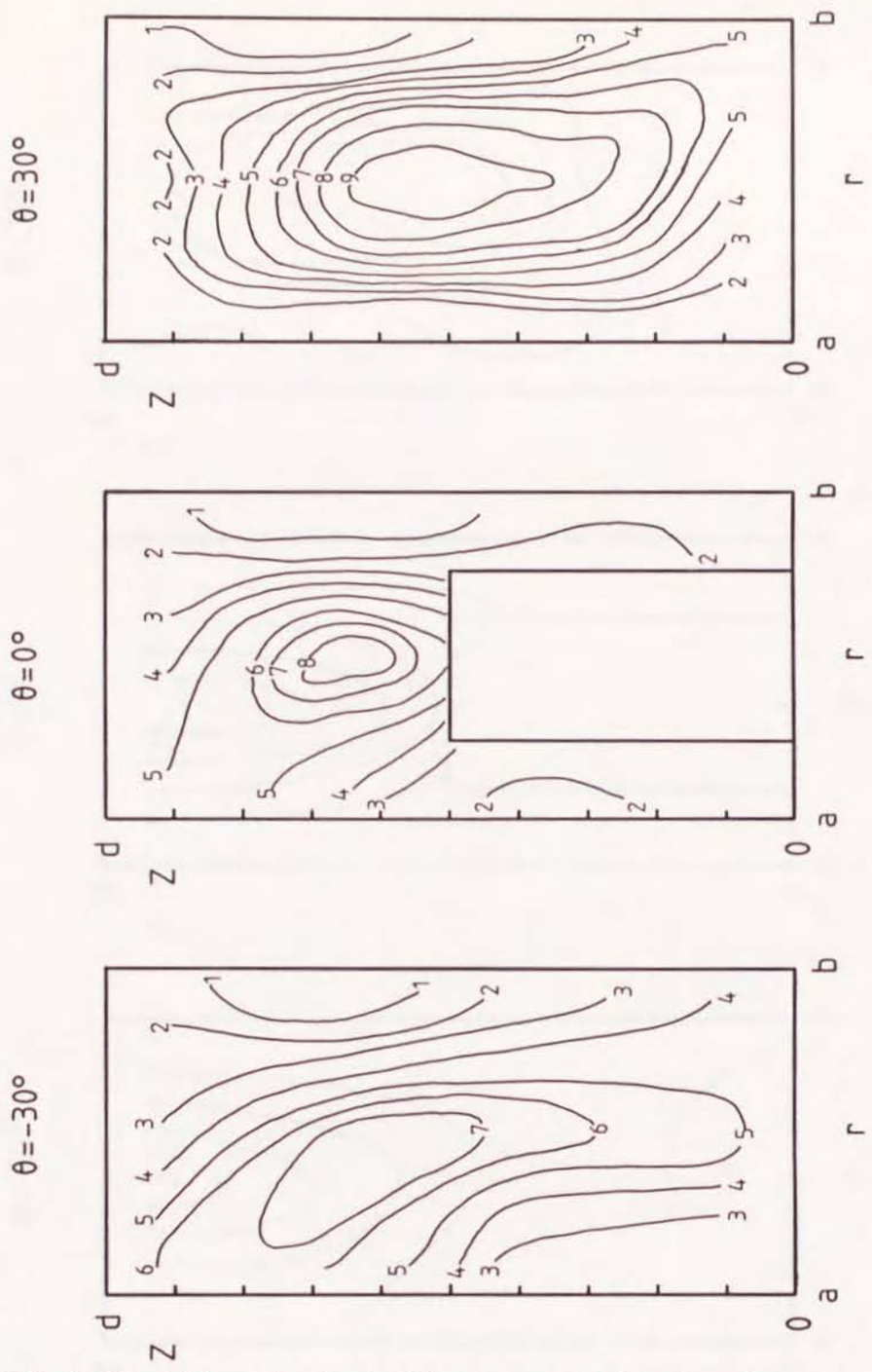

Fig. 7(a) Meridional distribution of the Fourier ground mode (m=3) of the normalized temperature perturbation at three different azimuthal positions (θ = -30° , 0° , 30°), analyzed during one period. Numerals in the figures are T"" multiplied by 100. Here, experimental parameters are Ω = 2.907× 10^{-1} rad/s, Δ T= 5.40℃ , T_o = 14.95℃ and k = 3.

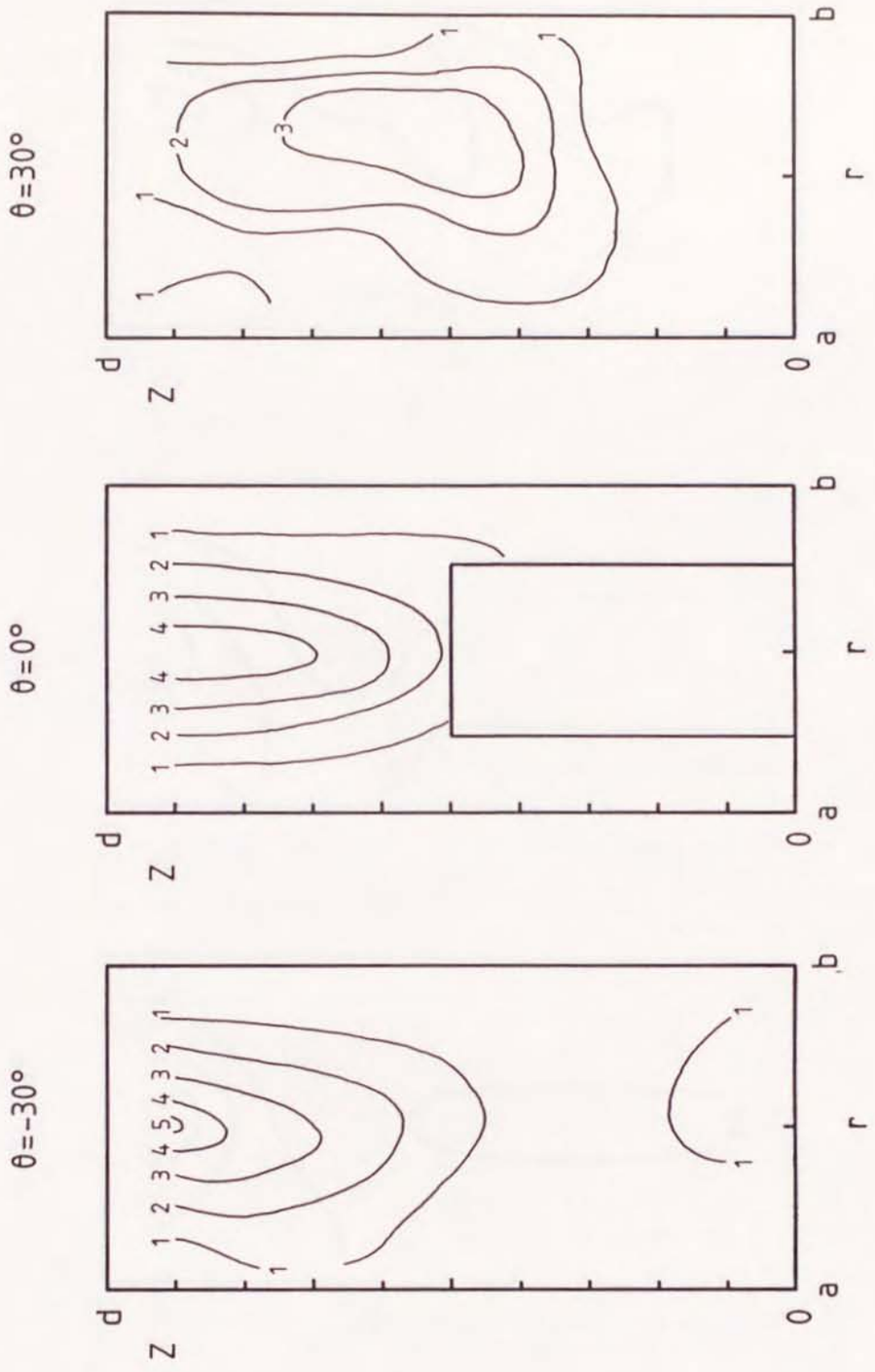

Fig. 7(b) Same as Fig 7(a) but for the second harmonic (m=6).

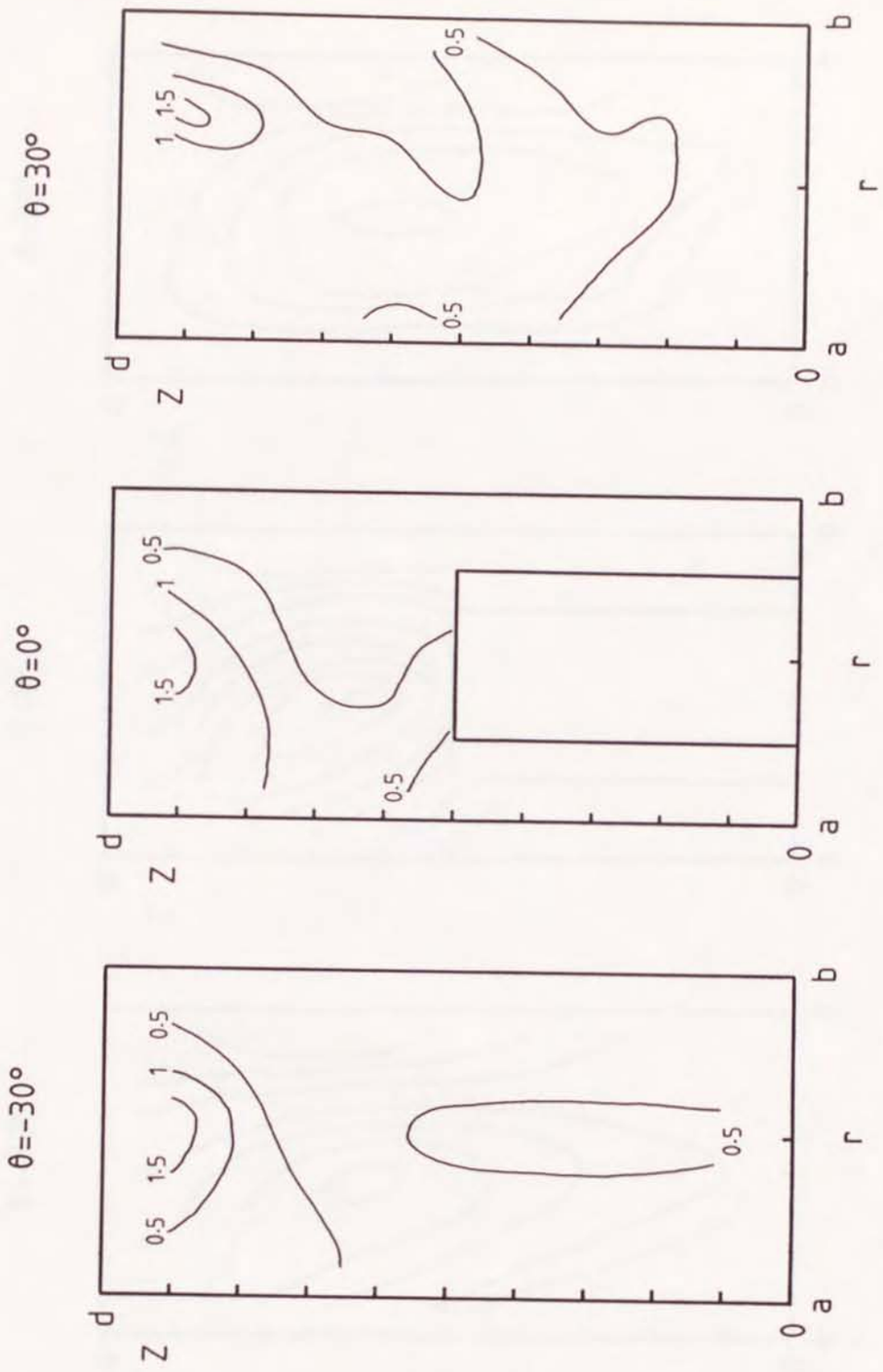

Fig. 7(c) Same as Fig 7(a) but for the third harmonic (m=9).

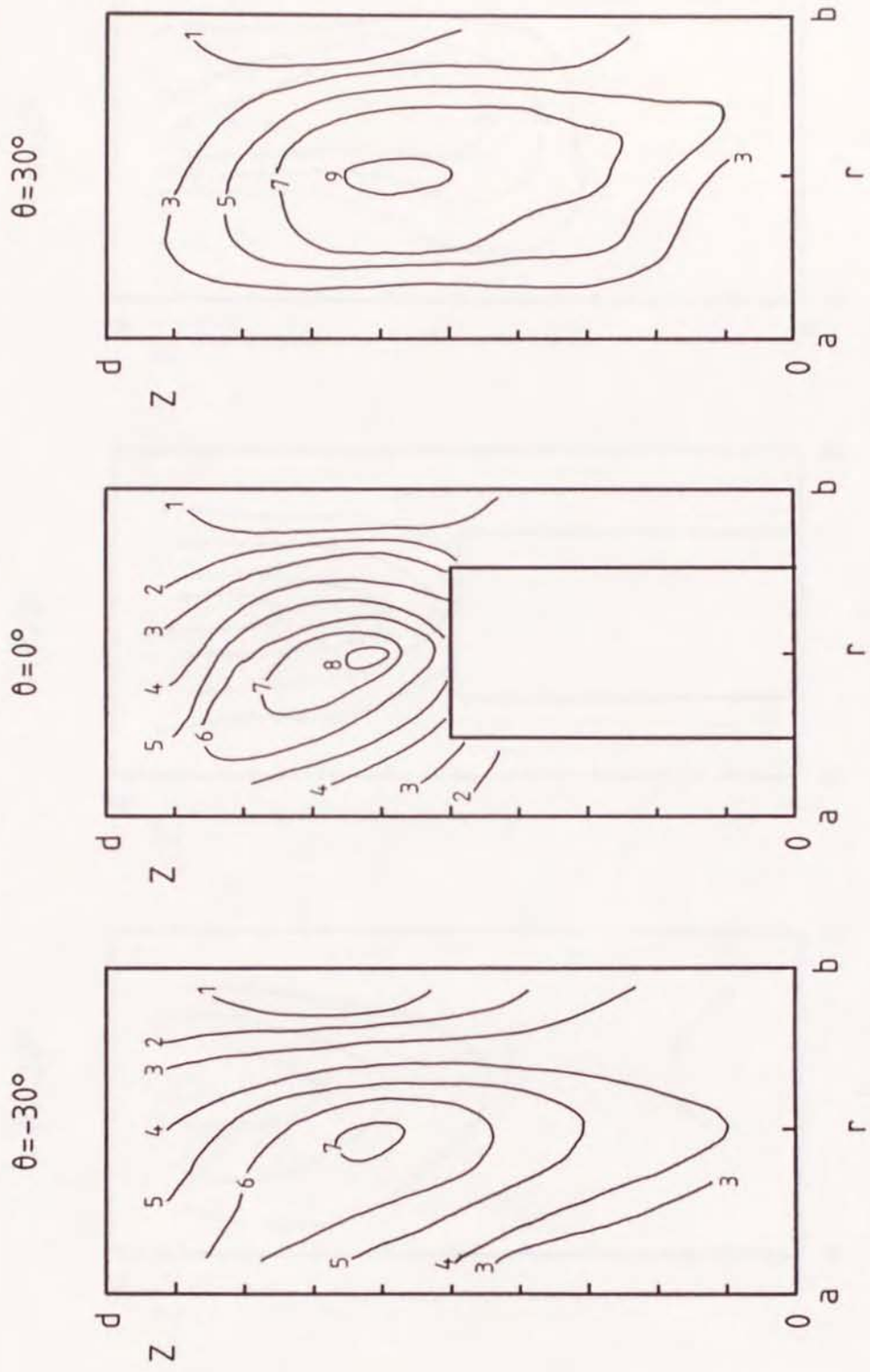

Fig. 8(a) Same as Fig. 7(a) but for the rotation rate Ω = 2.561×10^{-1} rad/s.

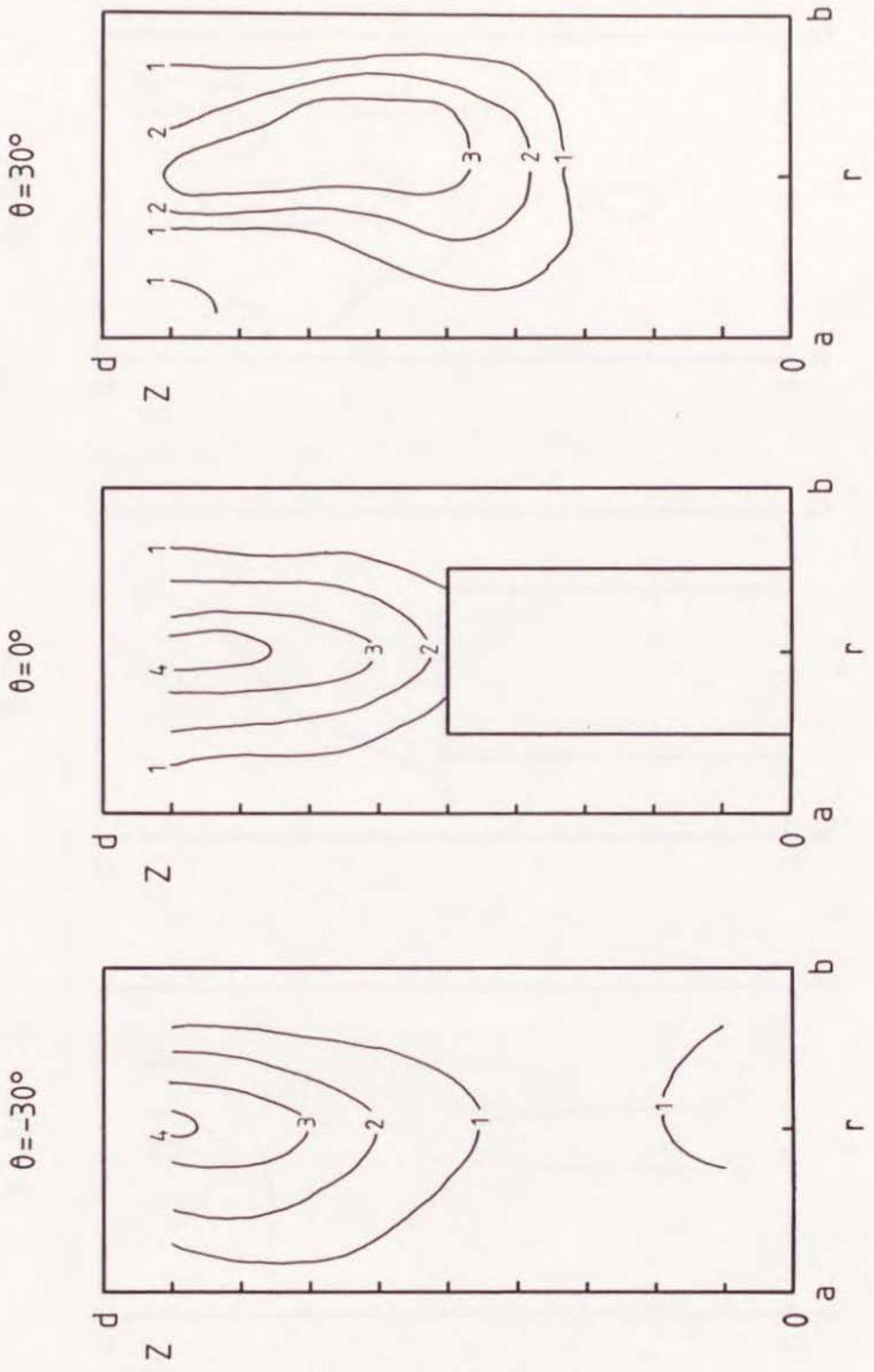

Fig. 8(b) Same as Fig. 7(b) but for the rotation rate Ω = 2.561×10^{-1} rad/s.

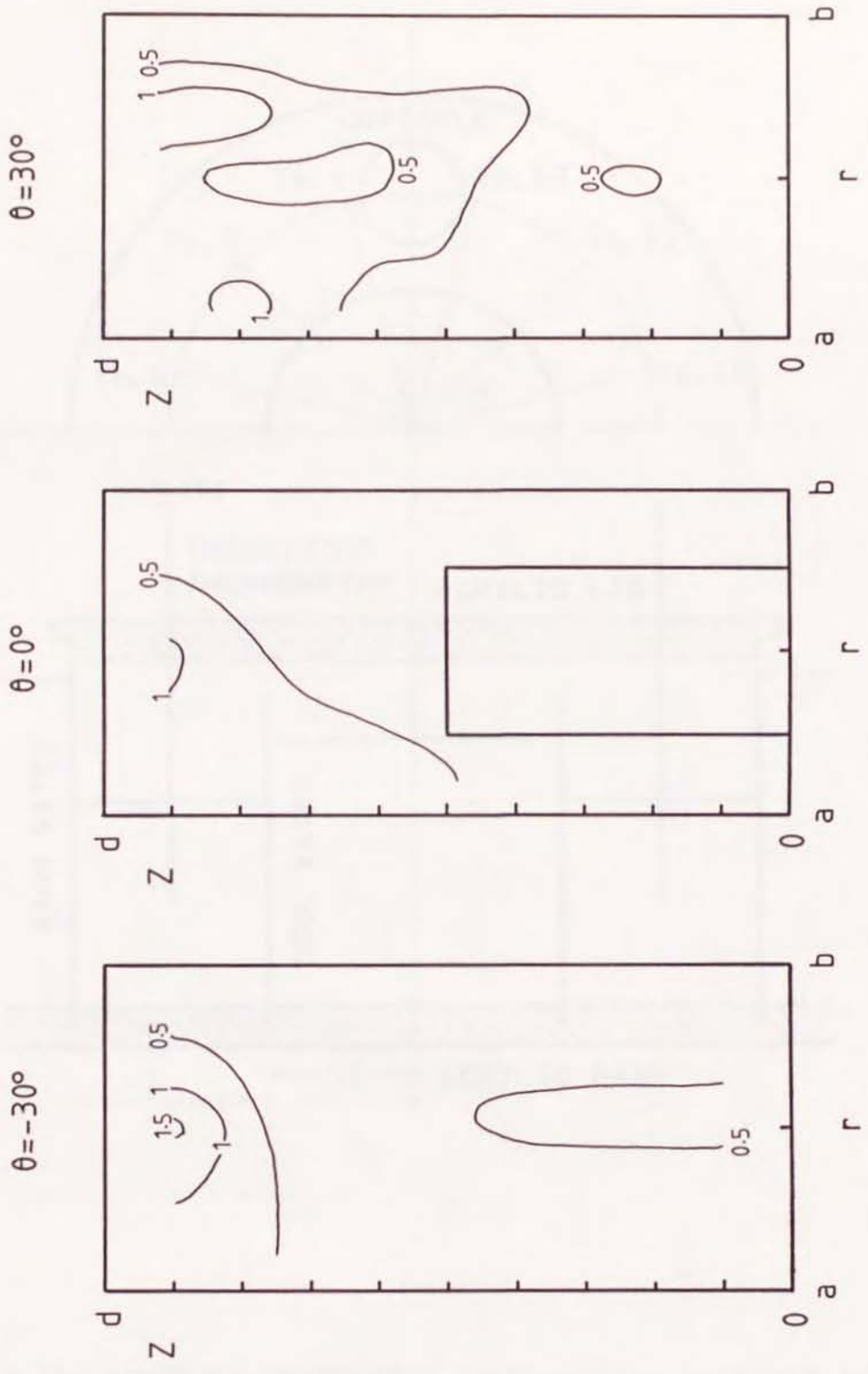

Fig. 8(c) Same as Fig. 7(c) but for the rotation rate Ω = 2.561×10^{-1} rad/s.

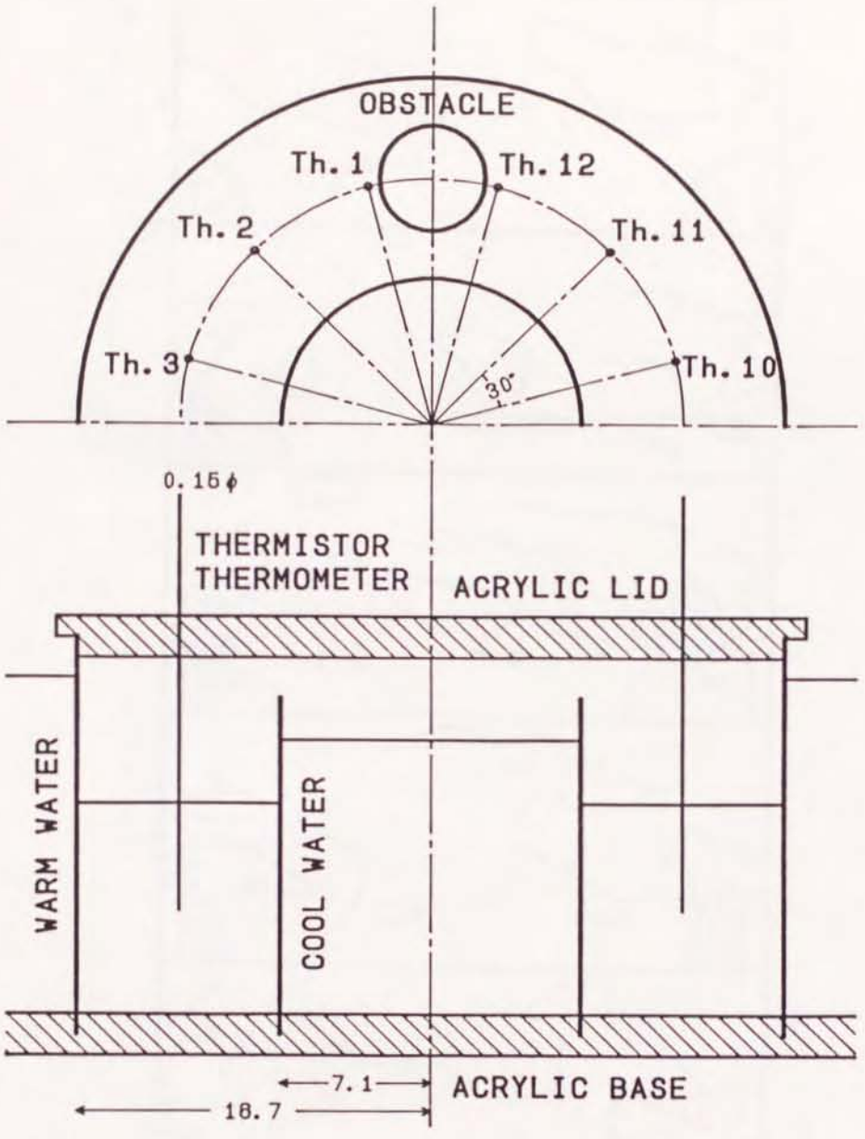

Fig. 9 The array of thermistor thermometers arranged to measure the azimuthal distribution of the basic and the perturbed temperature field. Twelve probes are set at the mean radius of the channel at every 30° , setting the first probe at θ = 15° . They can be moved down vertically at intervals of 1 cm.

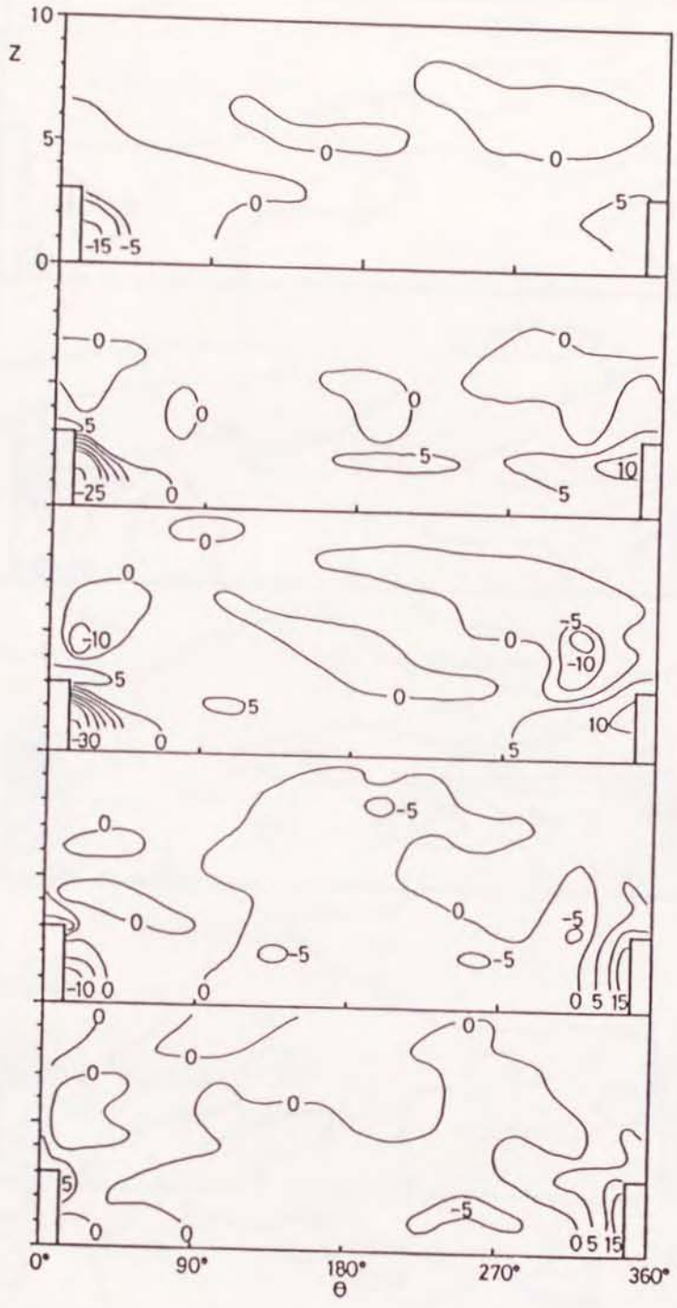

Fig. 10(a) The azimuth-height distribution of the time-mean temperature deviation from the zonal mean. Numerals in the figure are $\langle T-\langle T\rangle_{\theta}\rangle_{t}$ multiplied by 100. Here the normalized height of the obstacle H/d is 0.3 and the rotation rates Ω are 8.00×10^{-2}, 1.51×10^{-1}, 2.00×10^{-1}, 2.50×10^{-1} and 3.00×10^{-1} rad/s from the top to the bottom panel, respectively.

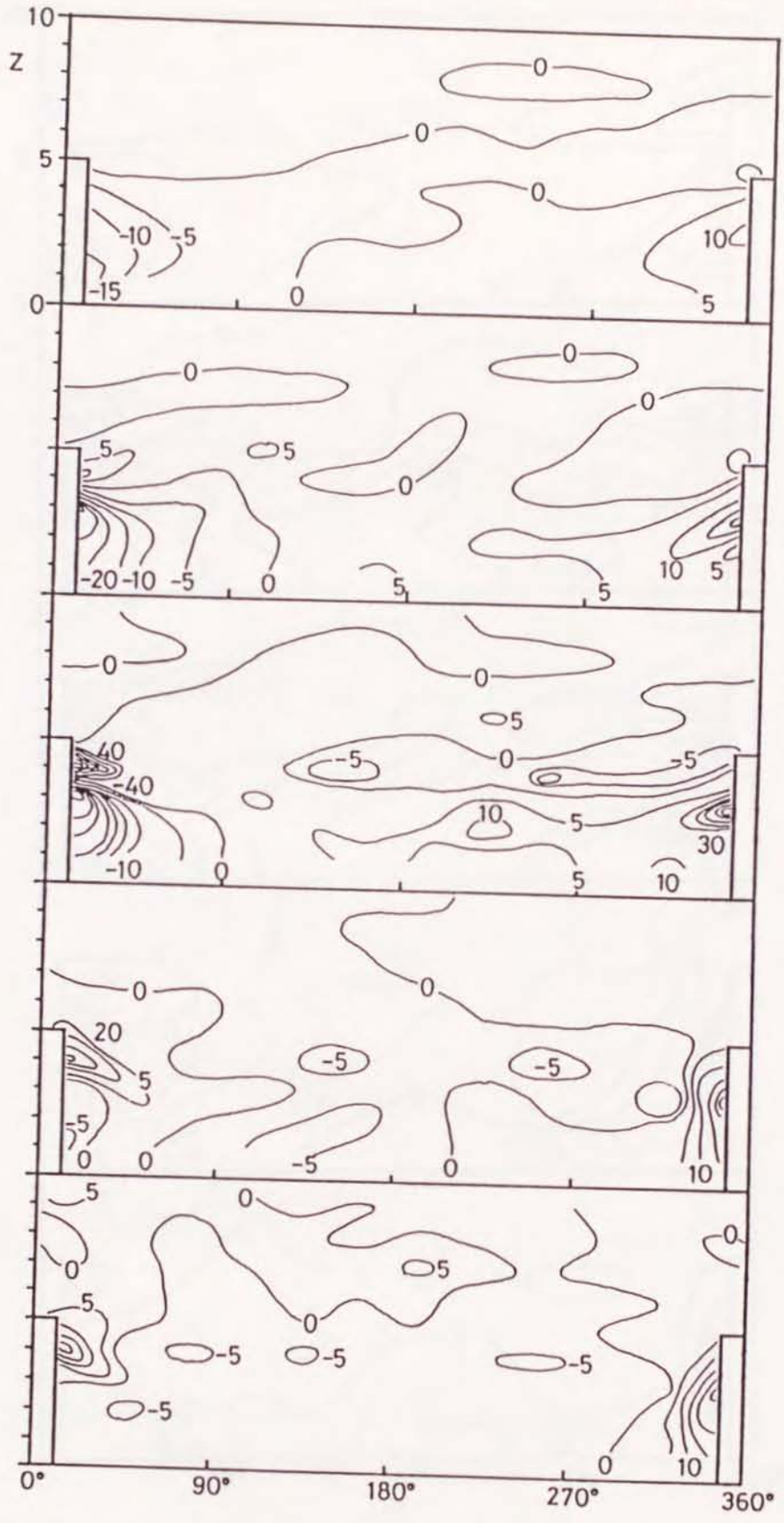

Fig. 10(b) Same as Fig. 10(a) but for H/d = 0.5.

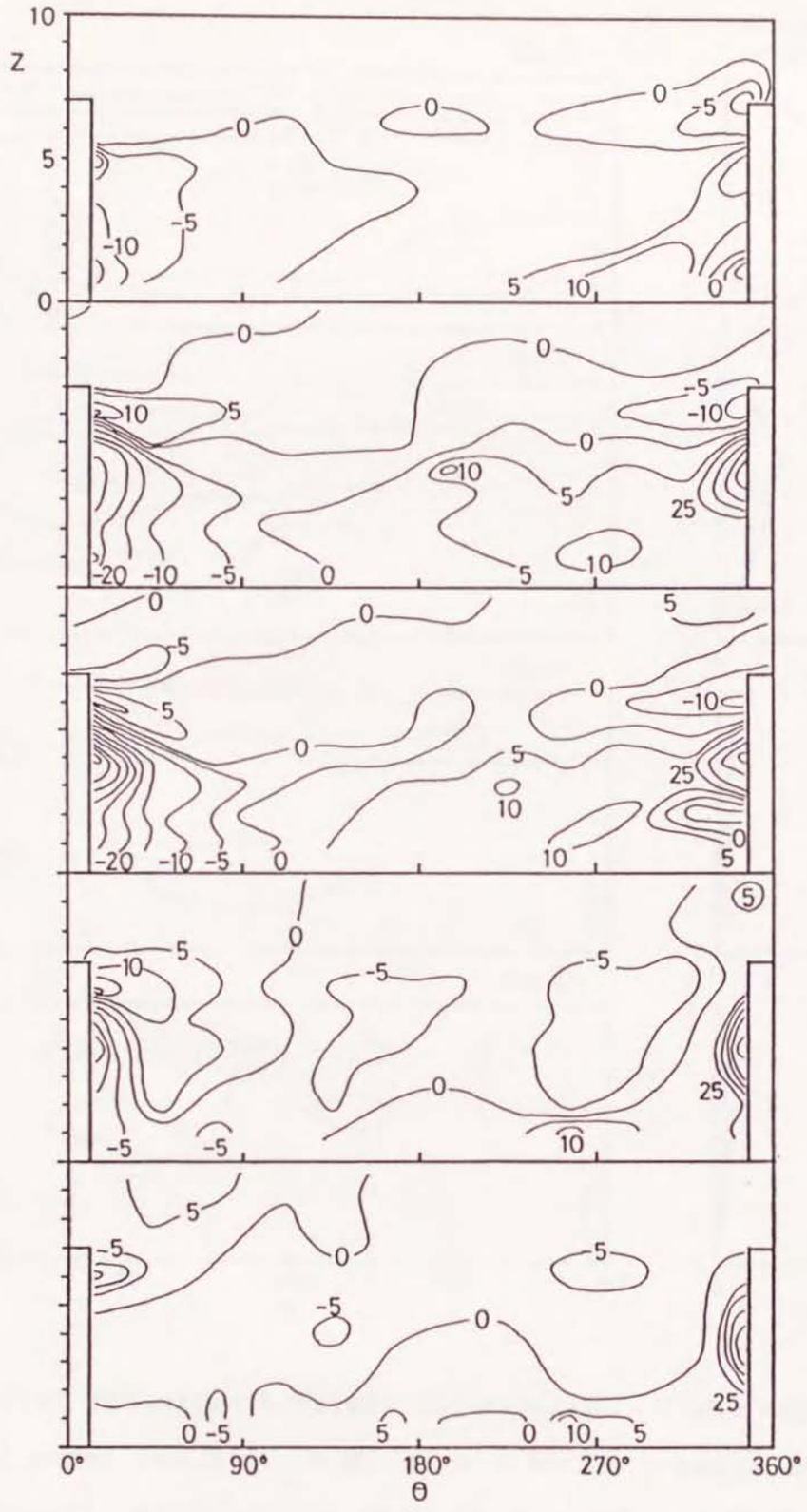

Fig. 10(c) Same as Fig. 10(a) but for H/d = 0.7.

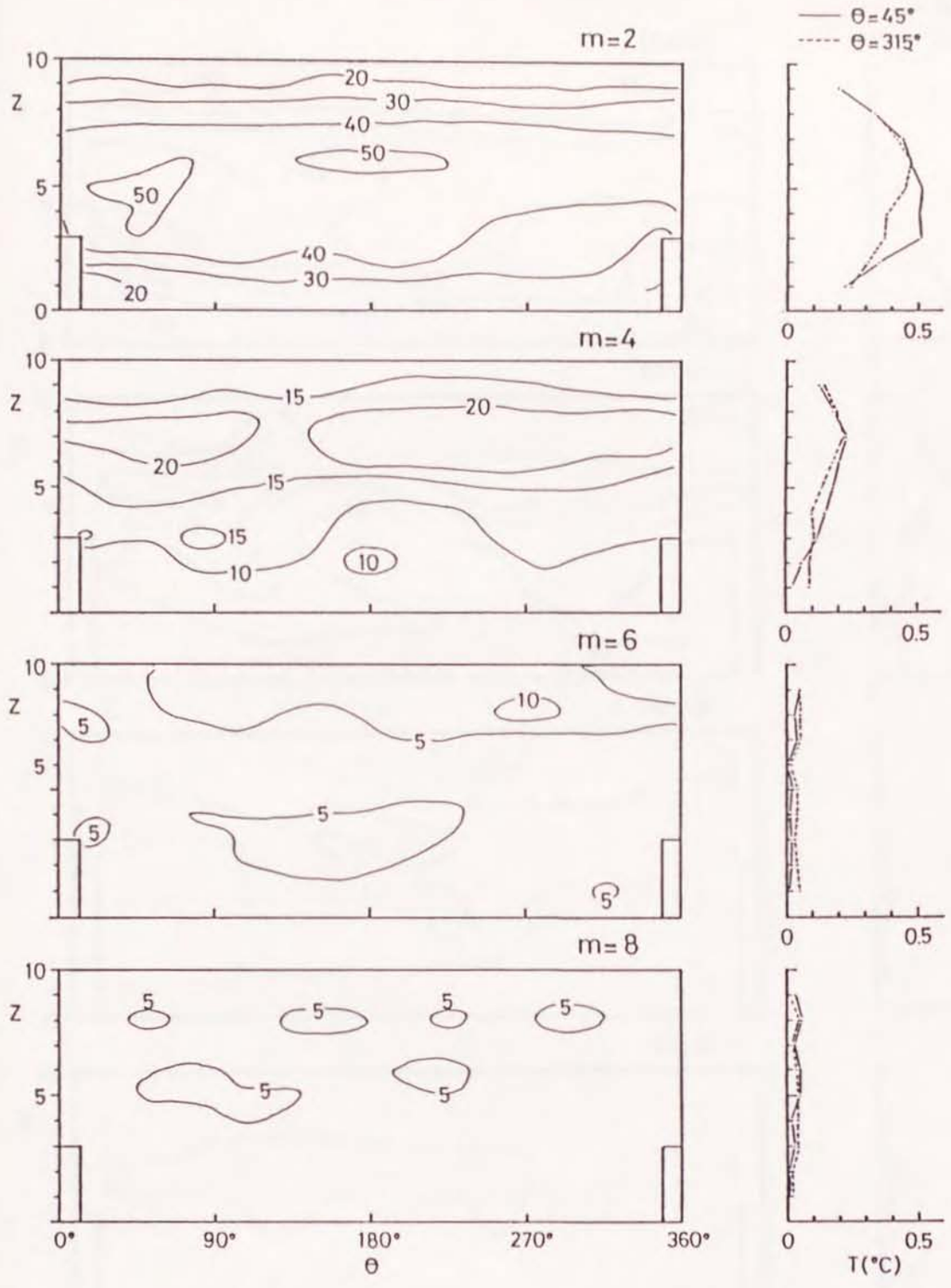

Fig. 11(a) The azimuth-height distribution of the amplitude of Fourier modes for H/d = 0.3, Ω = 2.5×10^{-1} rad/s and k = 2. The vertical profiles of them at θ = 45° and 315° are also shown on the right panels. Unit of numerals in the figure is 1/100 ℃ .

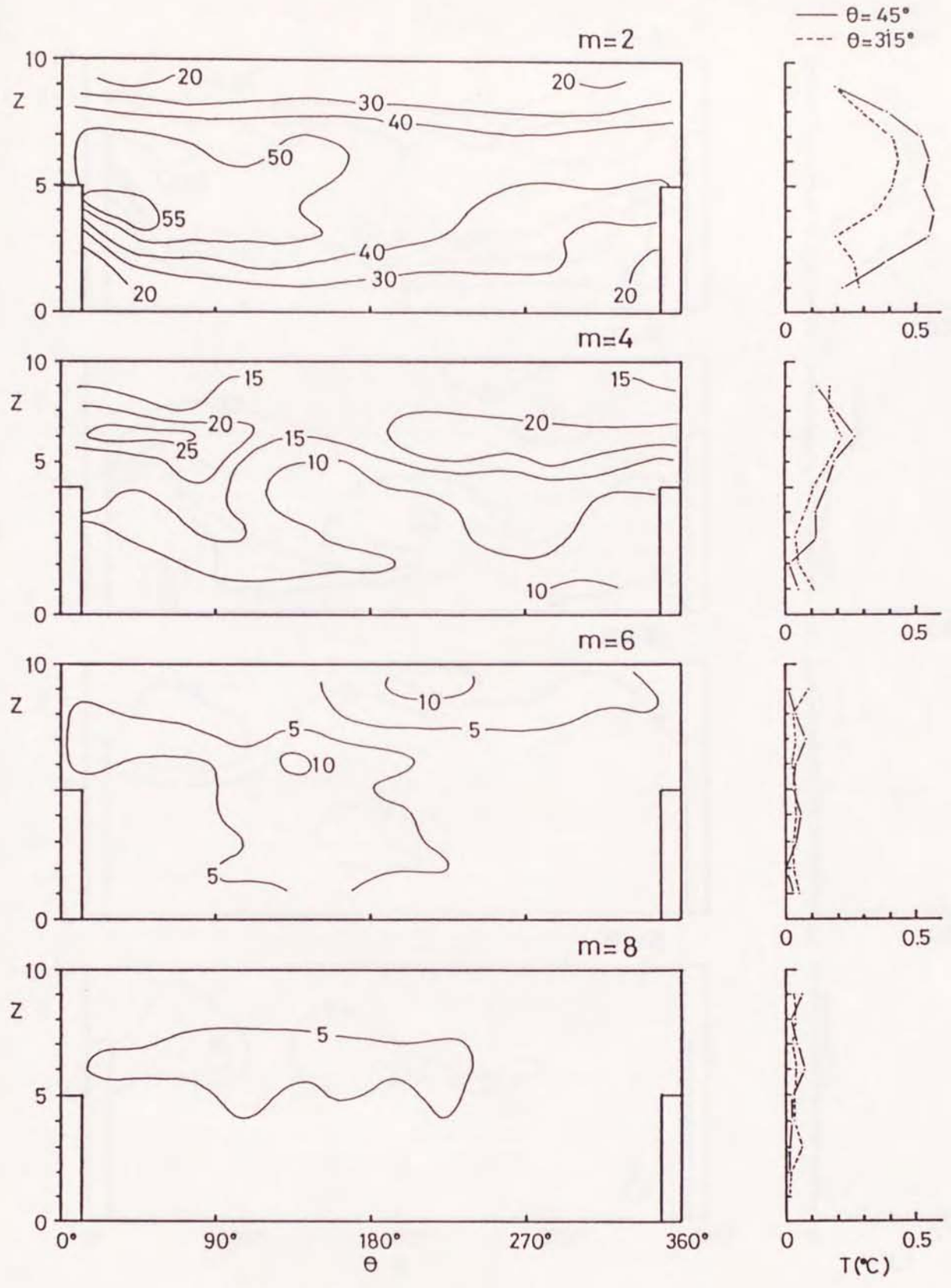

Fig. 11(b) Same as Fig. 11(a) but for H/d = 0.5.

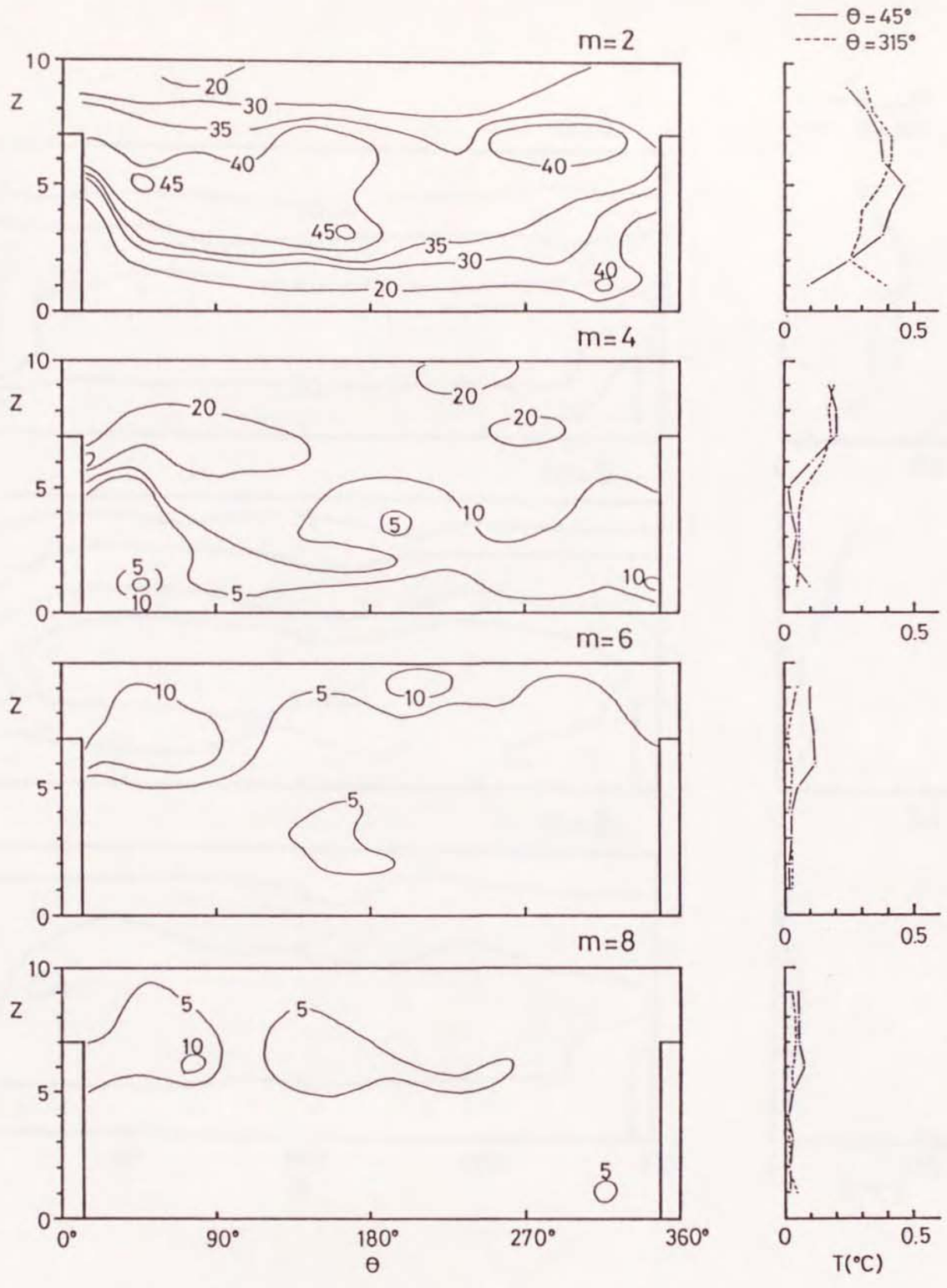

Fig. 11(c) Same as Fig. 11(a) but for H/d = 0.7.

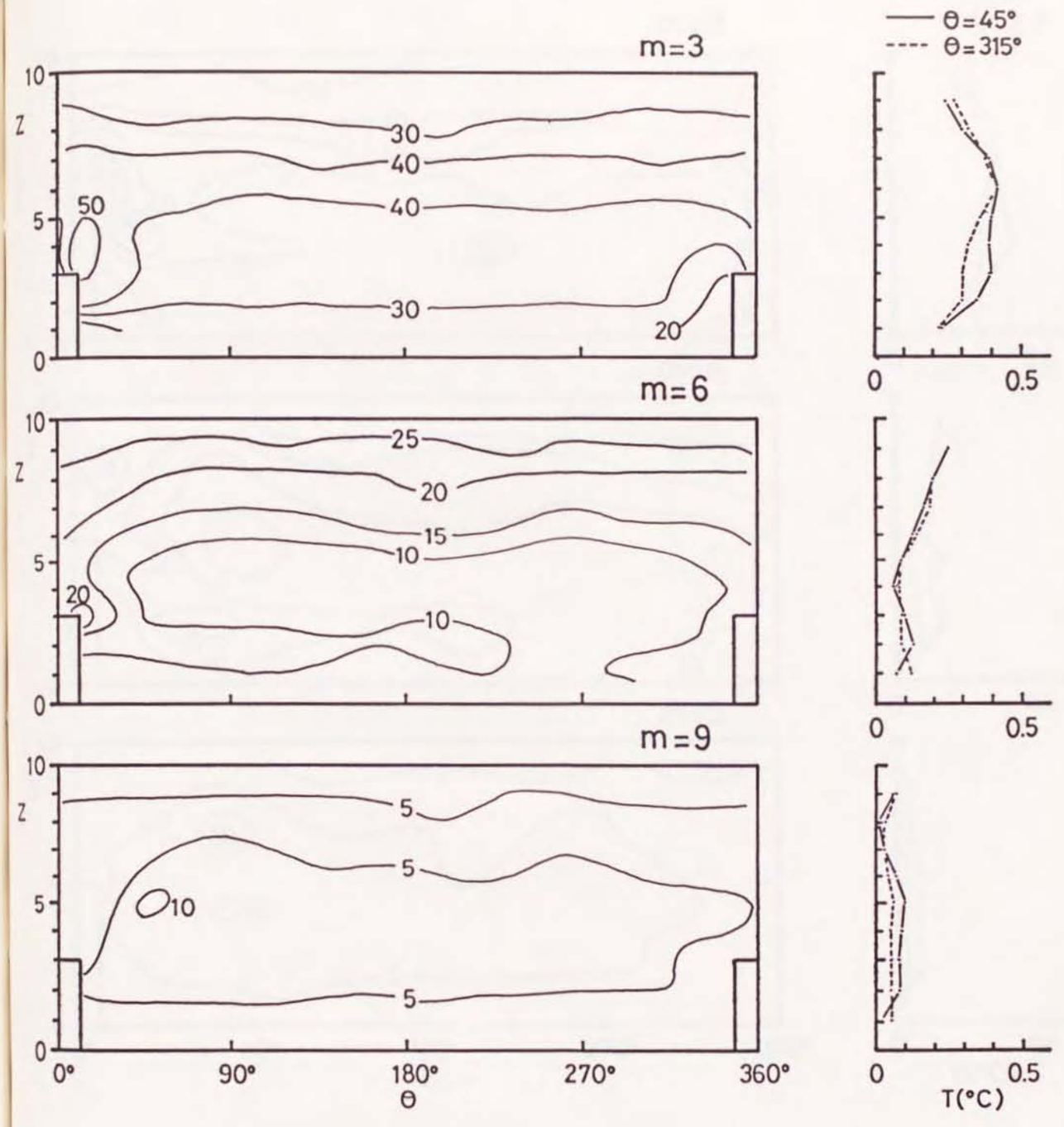

Fig. 12(a) Same as Fig. 11(a) but for $\Omega = 3.0 \times 10^{-1}$ rad/s and k = 3.

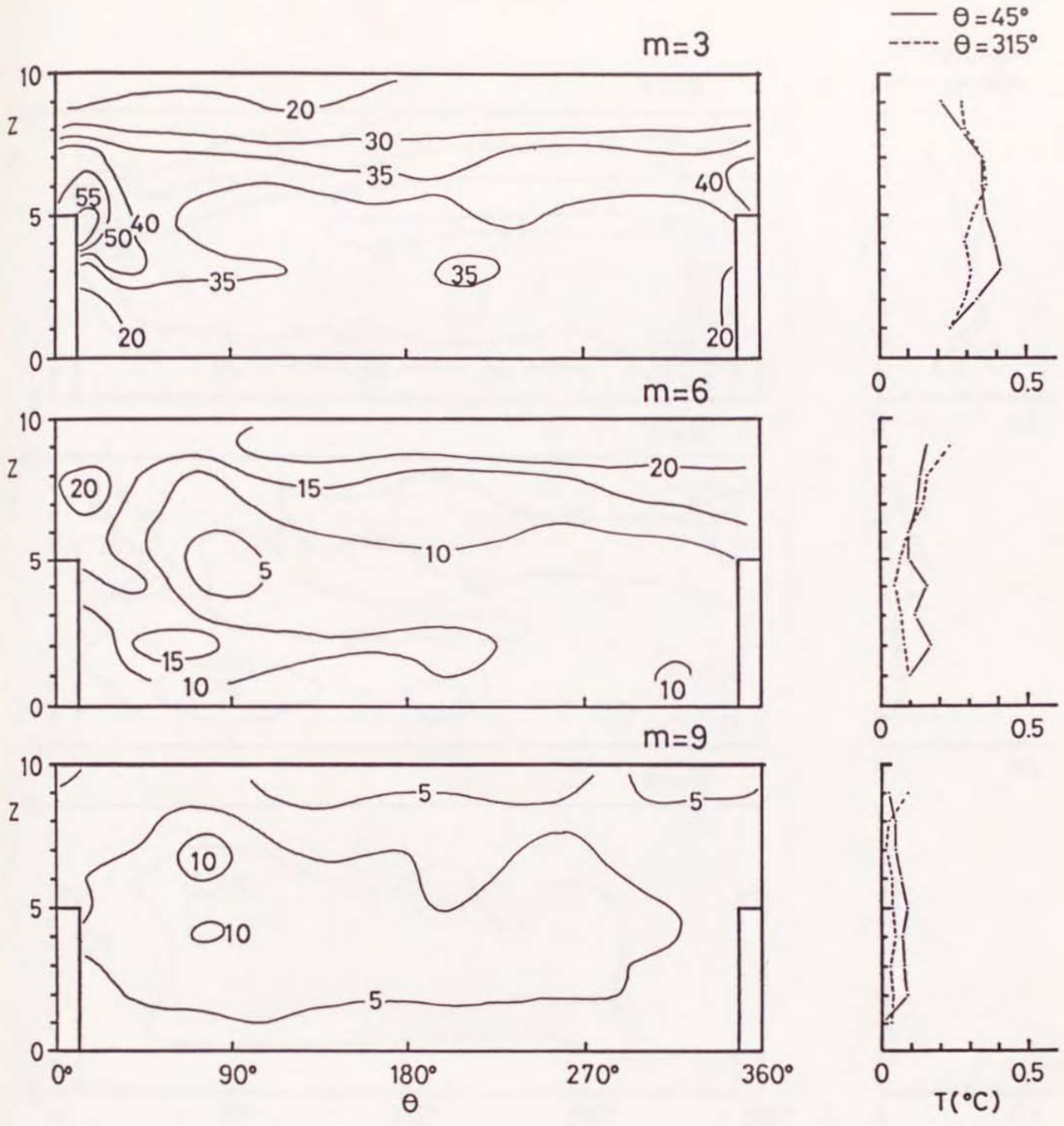

Fig. 12(b) Same as Fig. 11(b) but for $\Omega = 3.0 \times 10^{-1}$ rad/s and $k = 3$.

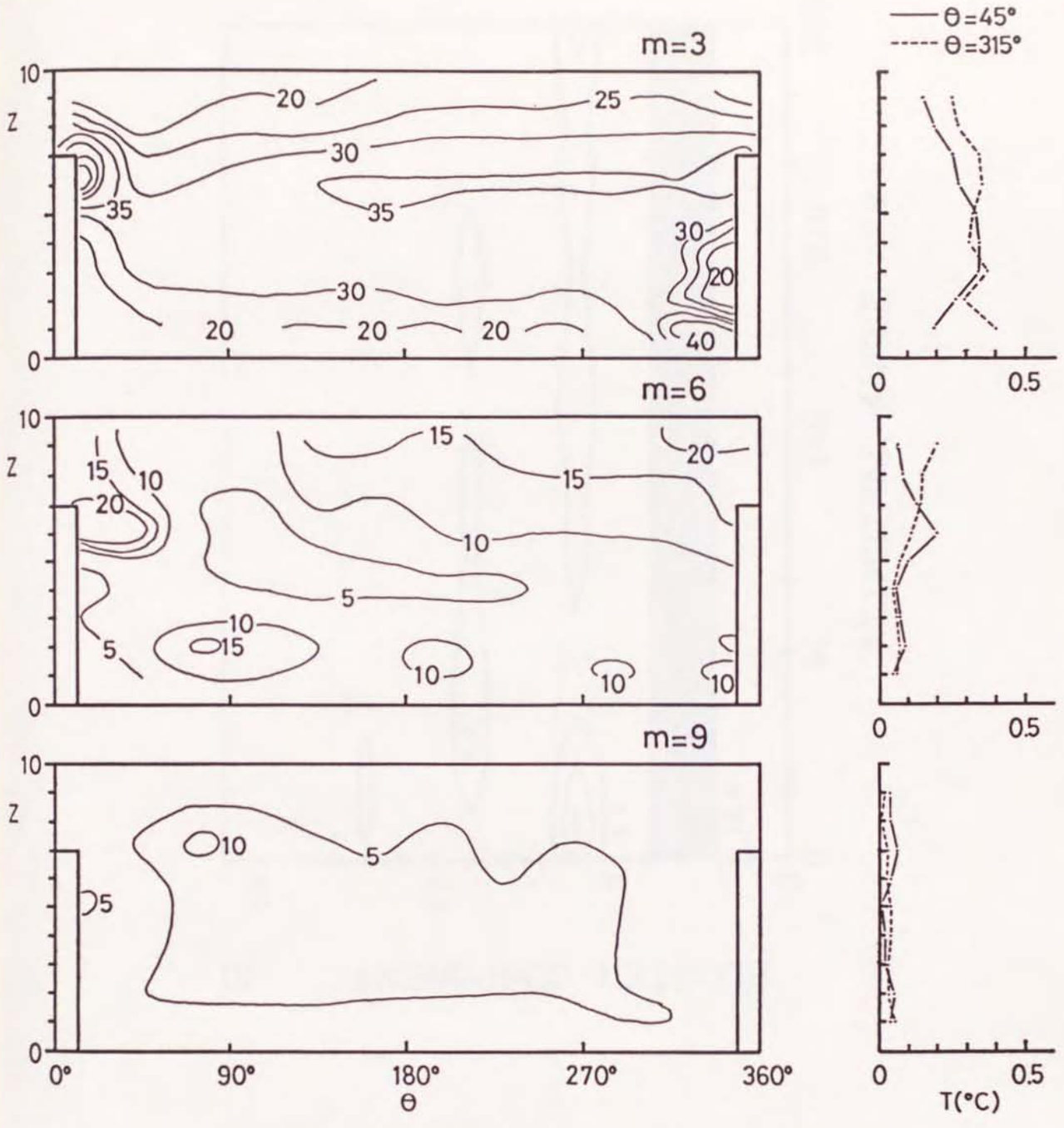

Fig. 12(c) Same as Fig. 11(c) but for $\Omega = 3.0 \times 10^{-1}$ rad/s and k = 3.

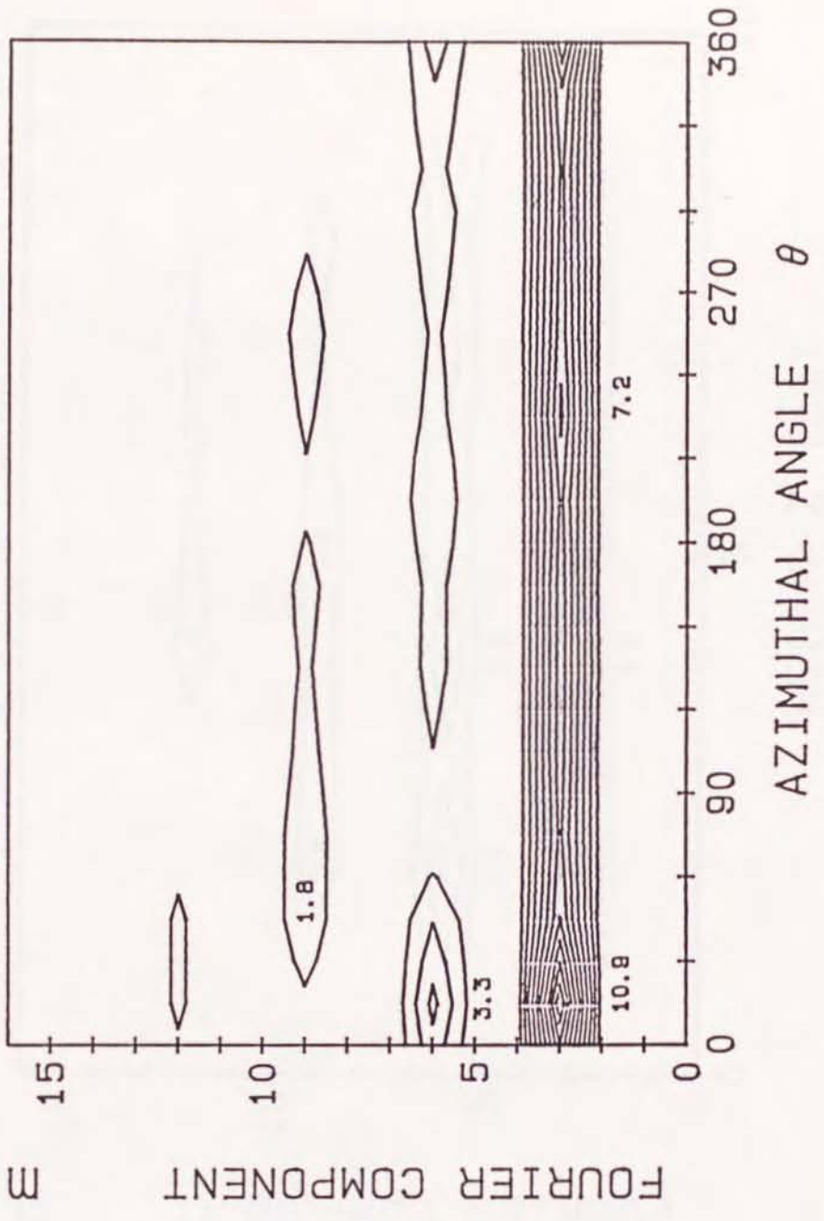

Fig. 13 The dependence of the normalized temperature variation of the first 15 Fourier modes on the azimuthal angle θ , where $\Omega = 3.0\times 10^{-1}$ rad/s, H/d = 0.5, H_t/d = 0.5 and k = 3. Numerals in the figure are T" multiplied by 100.

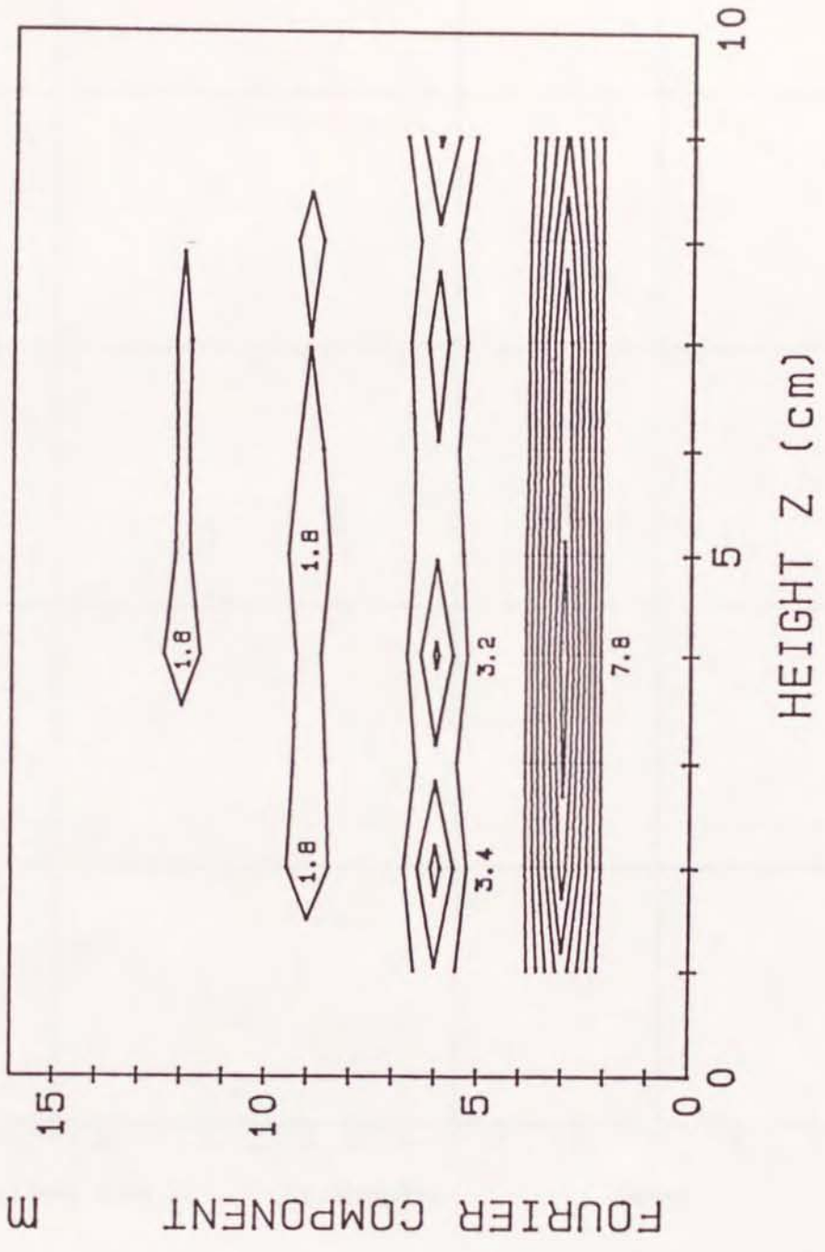

Fig. 14 The dependence of the normalized temperature variation of the first 15 Fourier components on height z, where Ω = 3.0 $\times$ 10^{-1} rad/s, H/d = 0.5 and k = 3. Numerals in the figure are multiplied by 100.

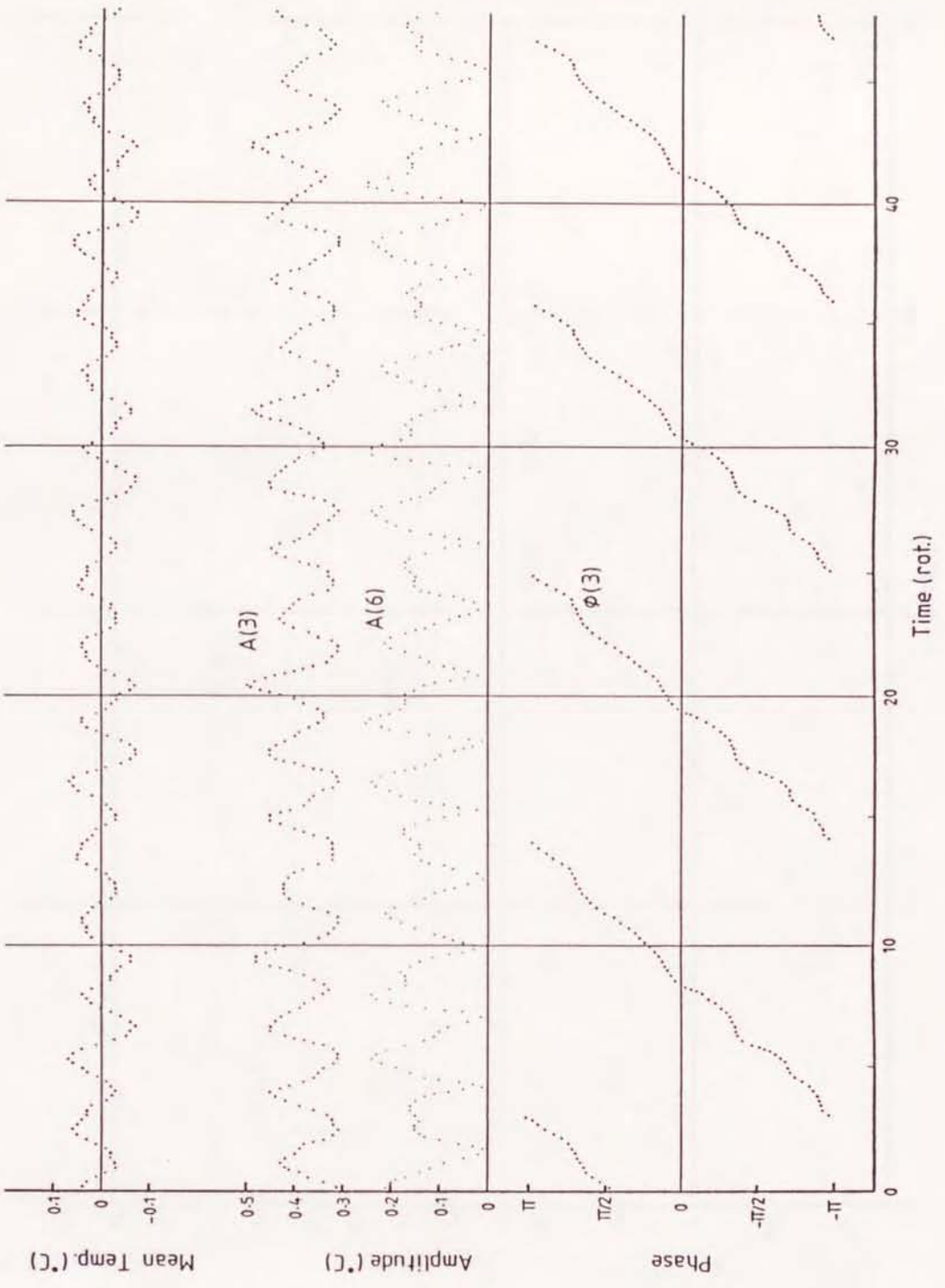

Fig. 15(a) The time-dependent behavior of the zonal mean temperature, amplitude and phase of each Fourier component, where $\Omega = 2.50 \times 10^{-1}$ rad/s, H/d = 0.5, H_T/d = 0.6 and k = 2. Notations in the figure, for example A(2) and ϕ (4), denote the amplitude of second harmonic and the phase of fourth harmonic, respectively.

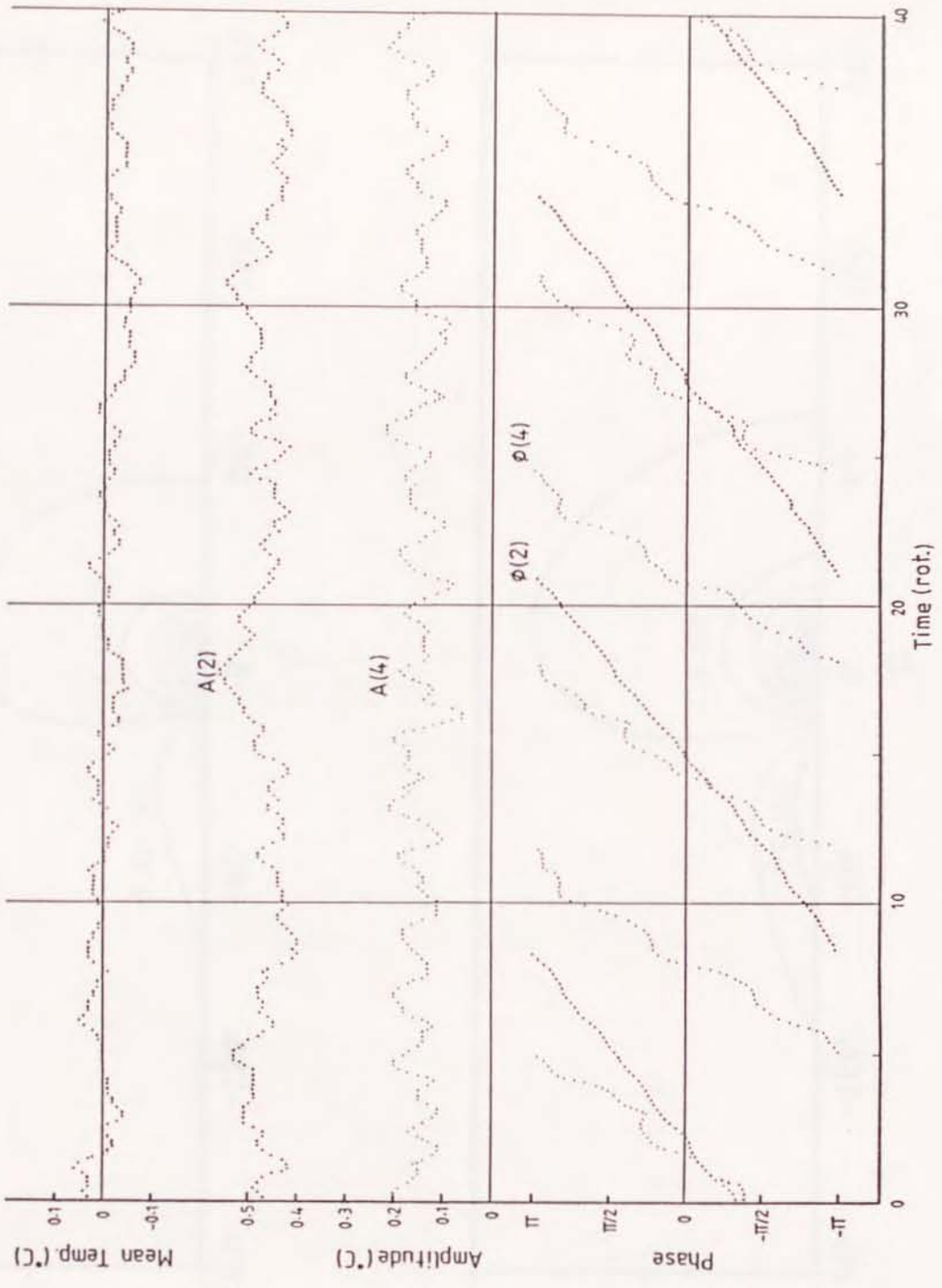

Fig. 15(b) Same as Fig. 15(a) but for $\Omega = 3.0 \times 10^{-1}$ rad/s, $H/d = 0.5$, $H_T/d = 0.6$ and $k = 3$.

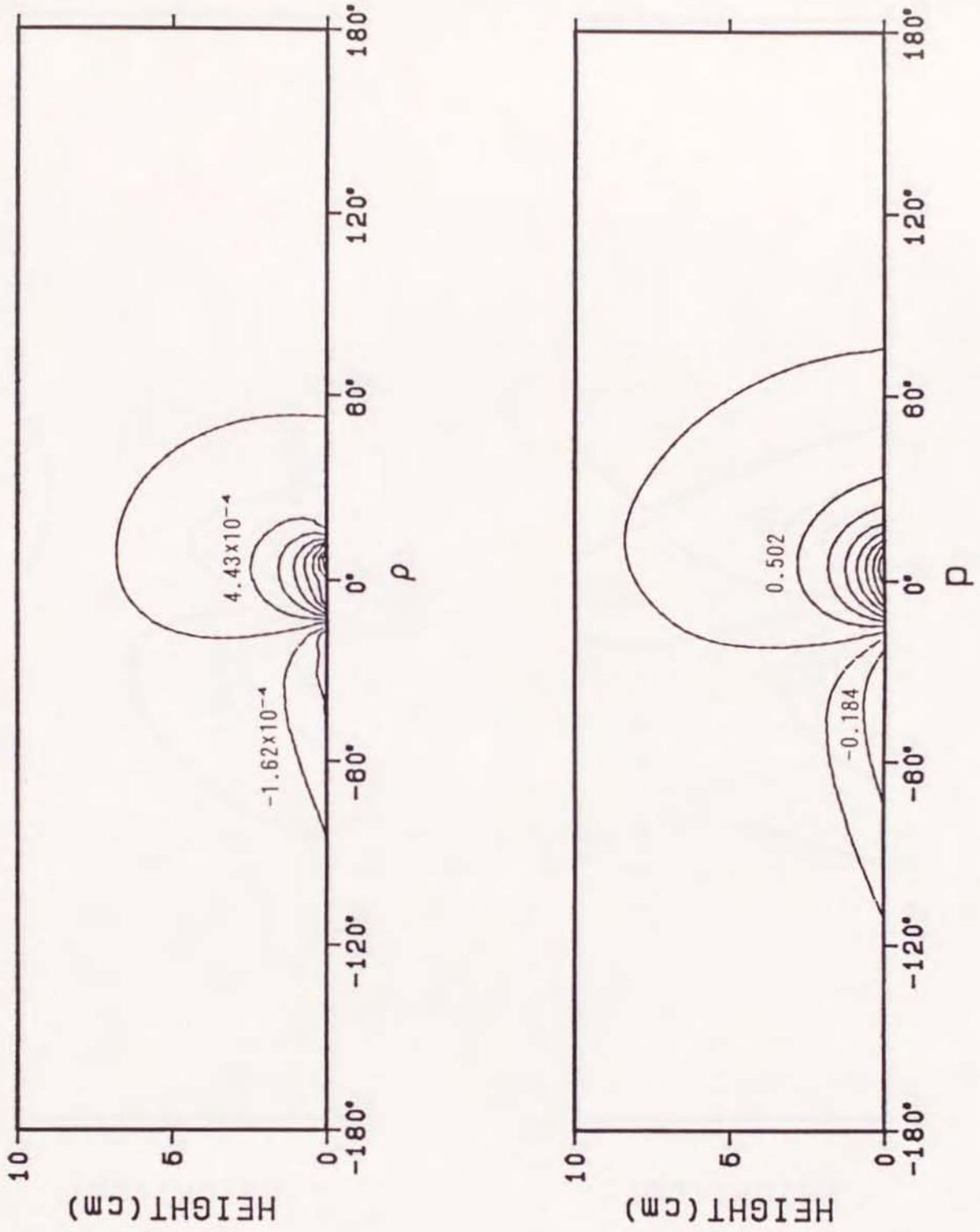

Fig. 16(a) The density and the pressure perturbation of forced baroclinic waves from the linear theory. Here the external parameters are f = 0.16, N = 0.26 and $\Lambda = 9.26\times 10^{-2}$ cm/s.

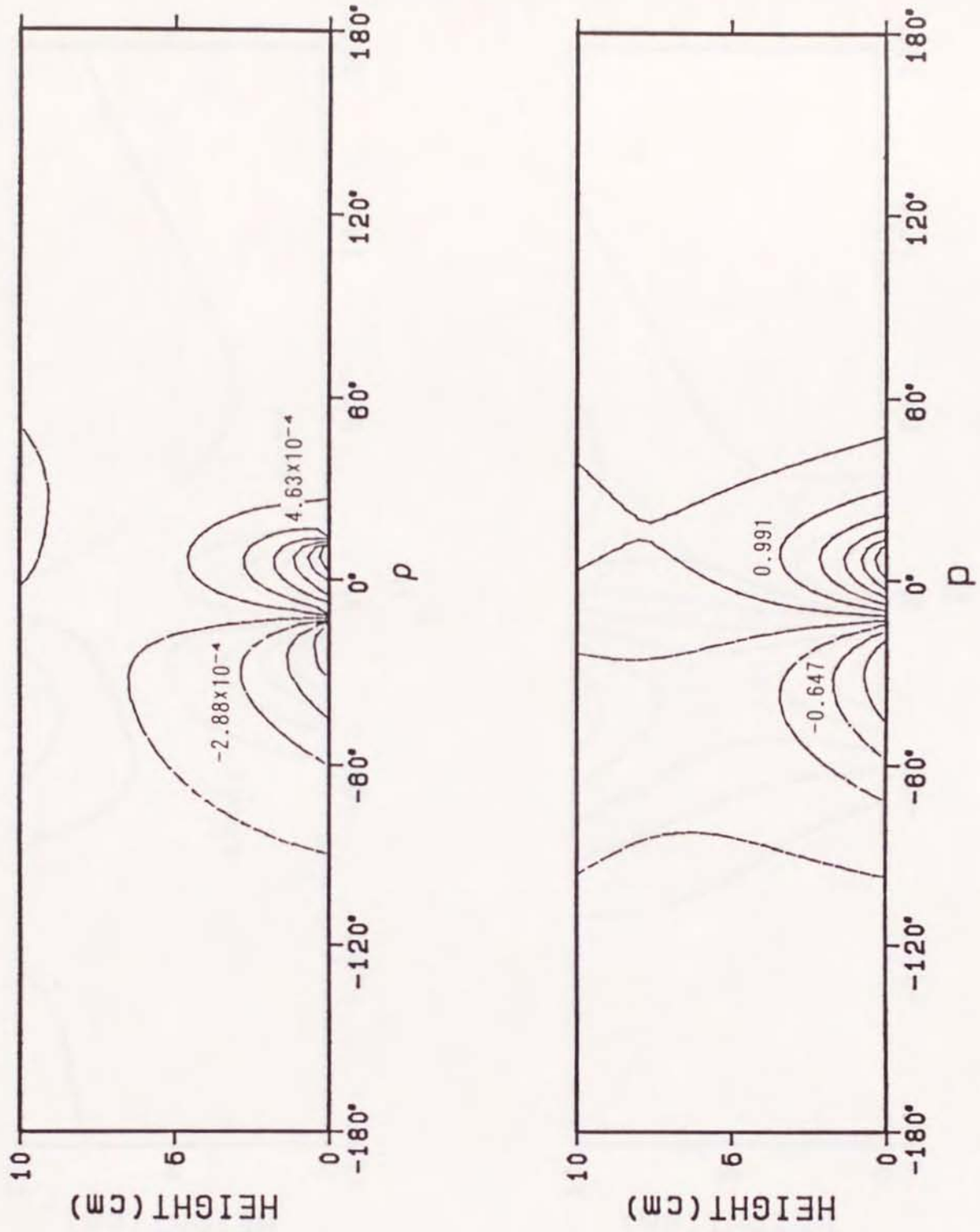

Fig. 16(b) Same as Fig. 16(a) but for f = 0.3 and Λ = 4.94 $\times 10^{-2}$ cm/s.

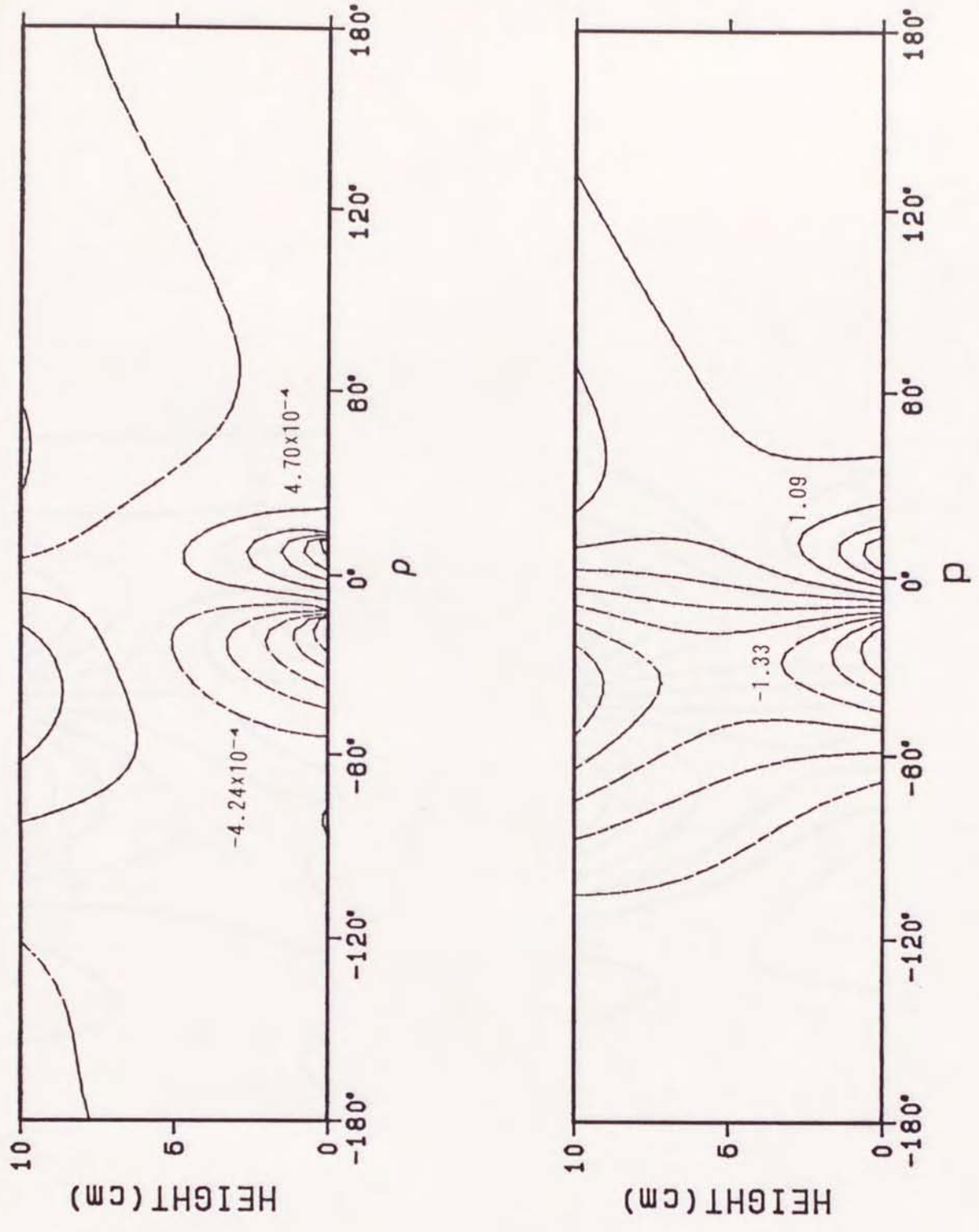

Fig. 16(c) Same as Fig. 16(a) but for f = 0.4 and Λ = 3.71 $\times 10^{-2}$ cm/s.

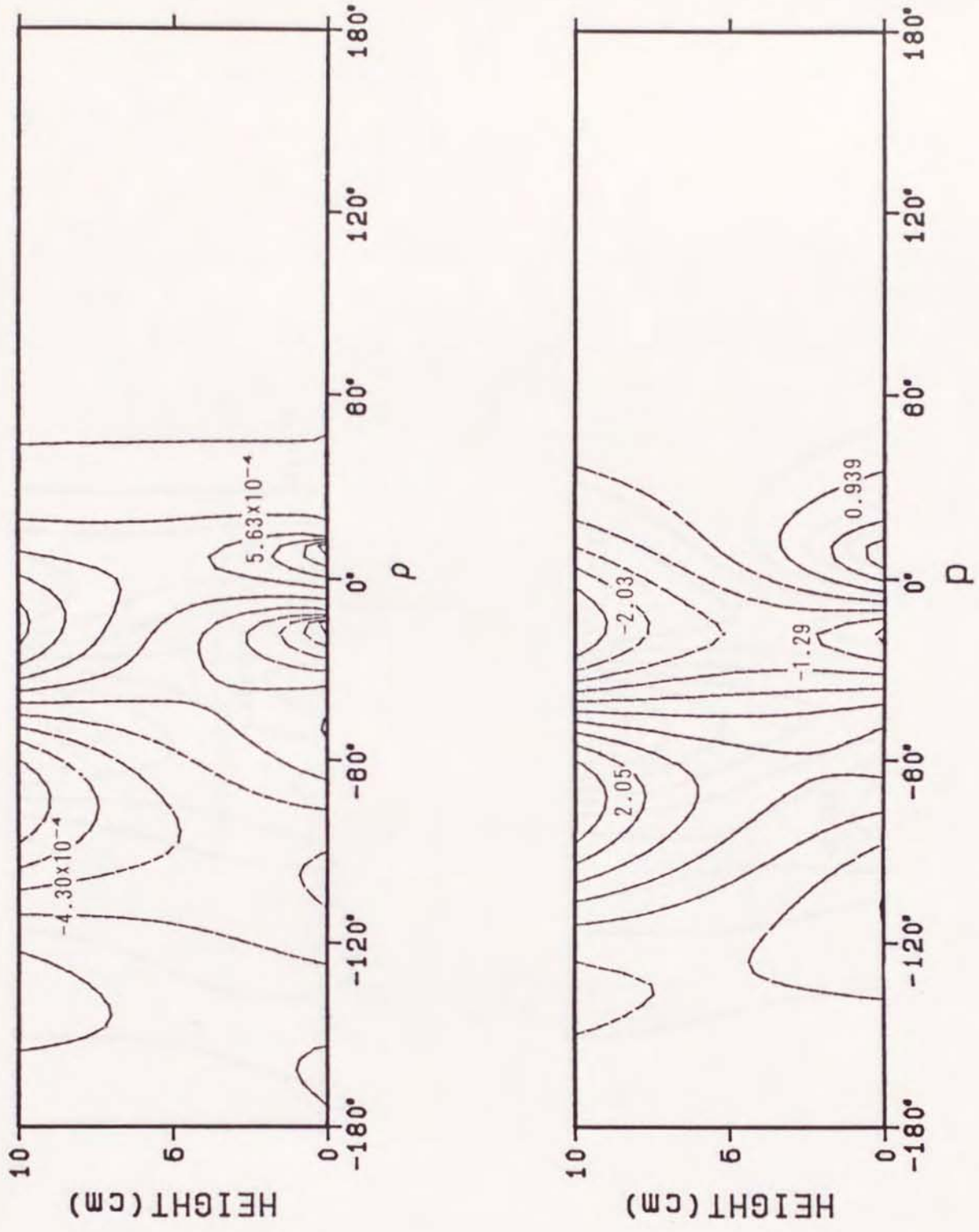

Fig. 16(d) Same as Fig. 16(a) but for f = 0.5 and Λ = 2.96 $\times 10^{-2}$ cm/s.

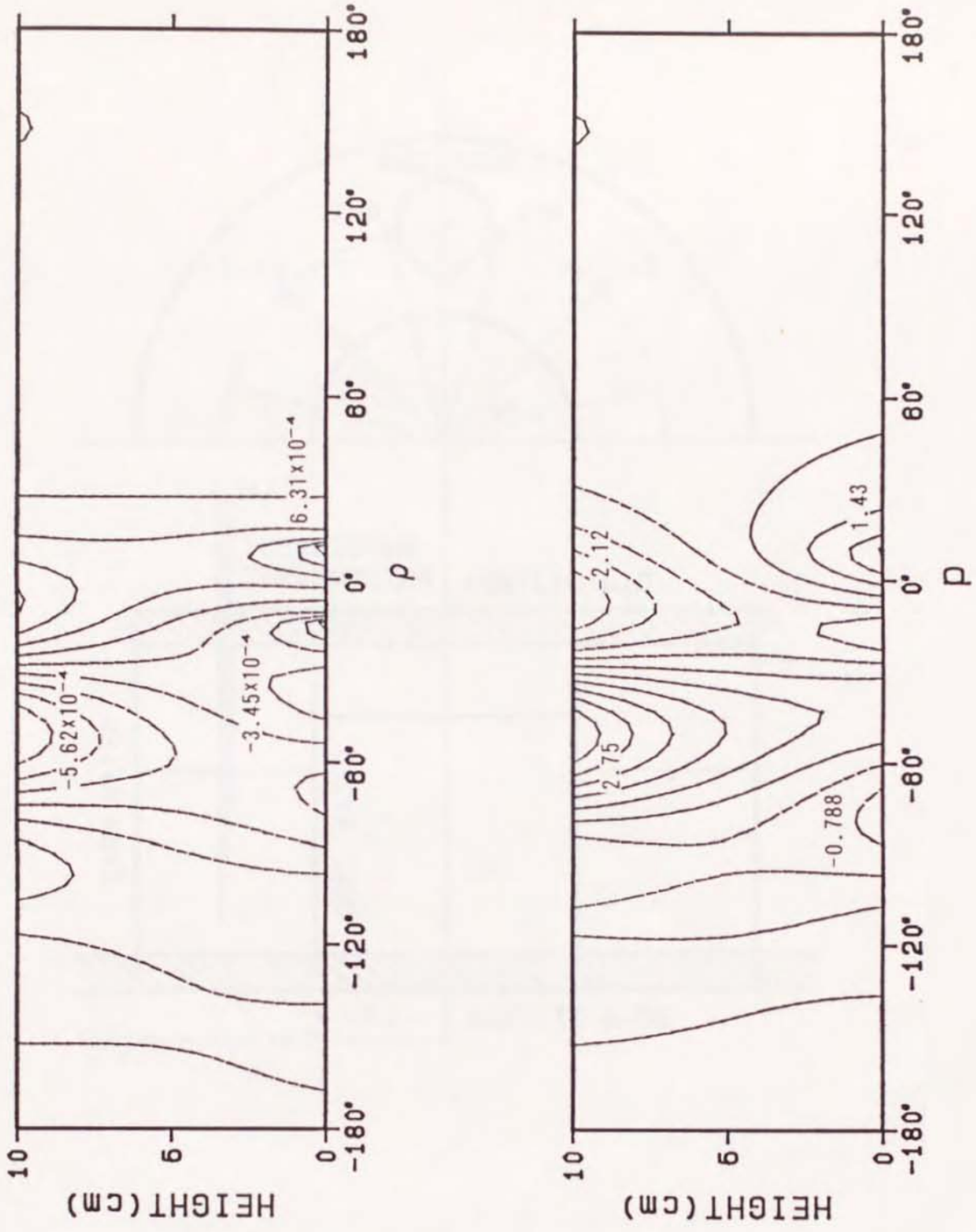

Fig. 16(e) Same as Fig. 16(a) but for f = 0.6 and Λ = 2.47 $\times 10^{-2}$ cm/s.

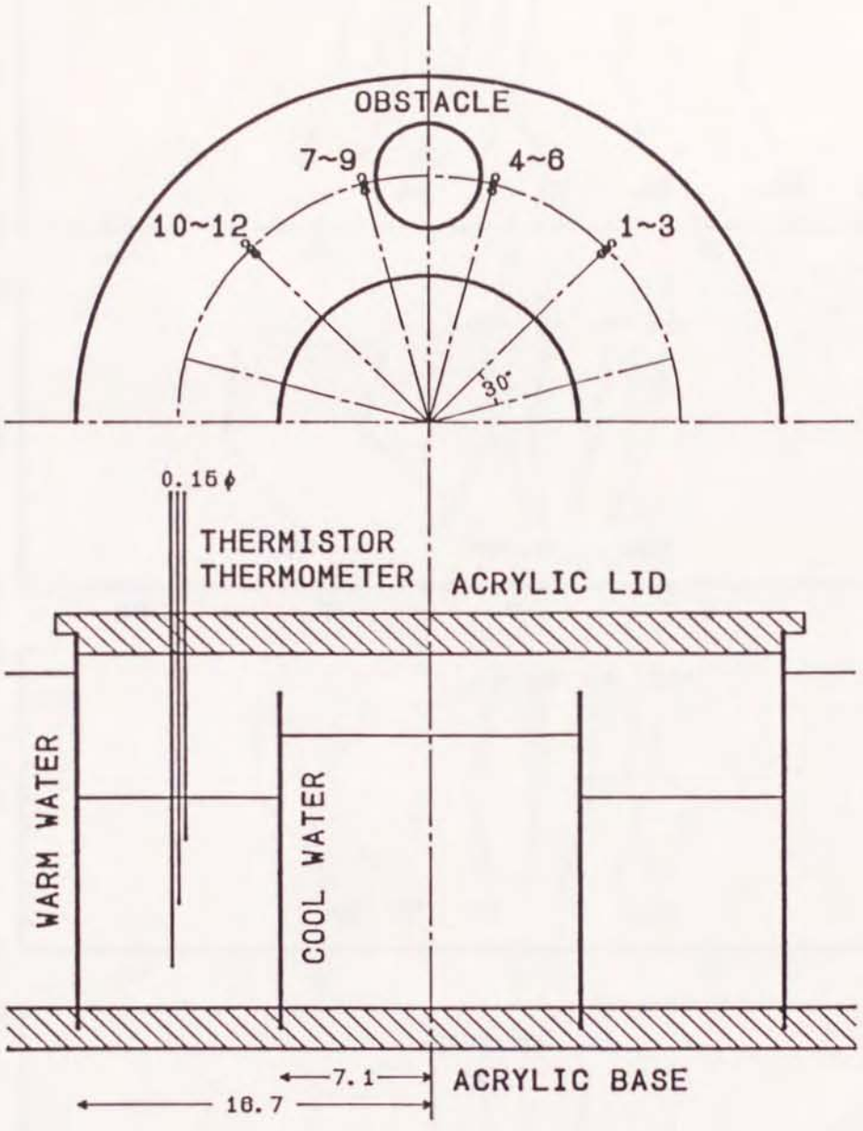

Fig. 17 The array of thermistor thermometers arranged for measuring the vertical structure of baroclinic waves. In this array, four groups of probes are set at the mean radius and at θ = -45° , -15° , 15° and 45° with each group consisting of three thermistor thermometers set at z/d = 0.2, 0.5 and 0.8.

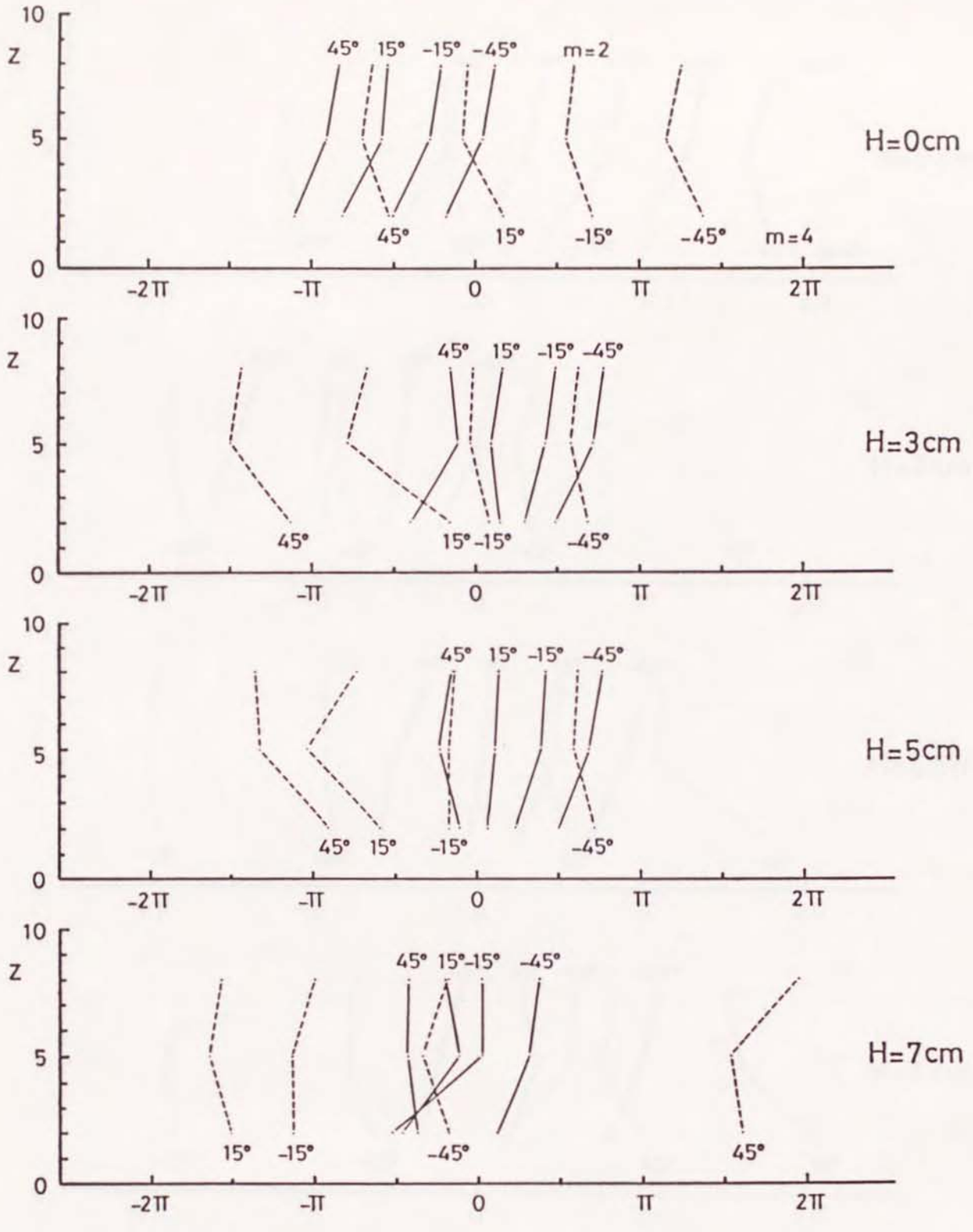

Fig. 18(a) The vertical structure of baroclinic waves at various positions relative to the obstacle (θ = -45° , -15° , 15° , 45°), where $\Omega = 2.50 \times 10^{-1}$ rad/s , k = 2 and H/d=0, 0.3, 0.5 and 0.7.

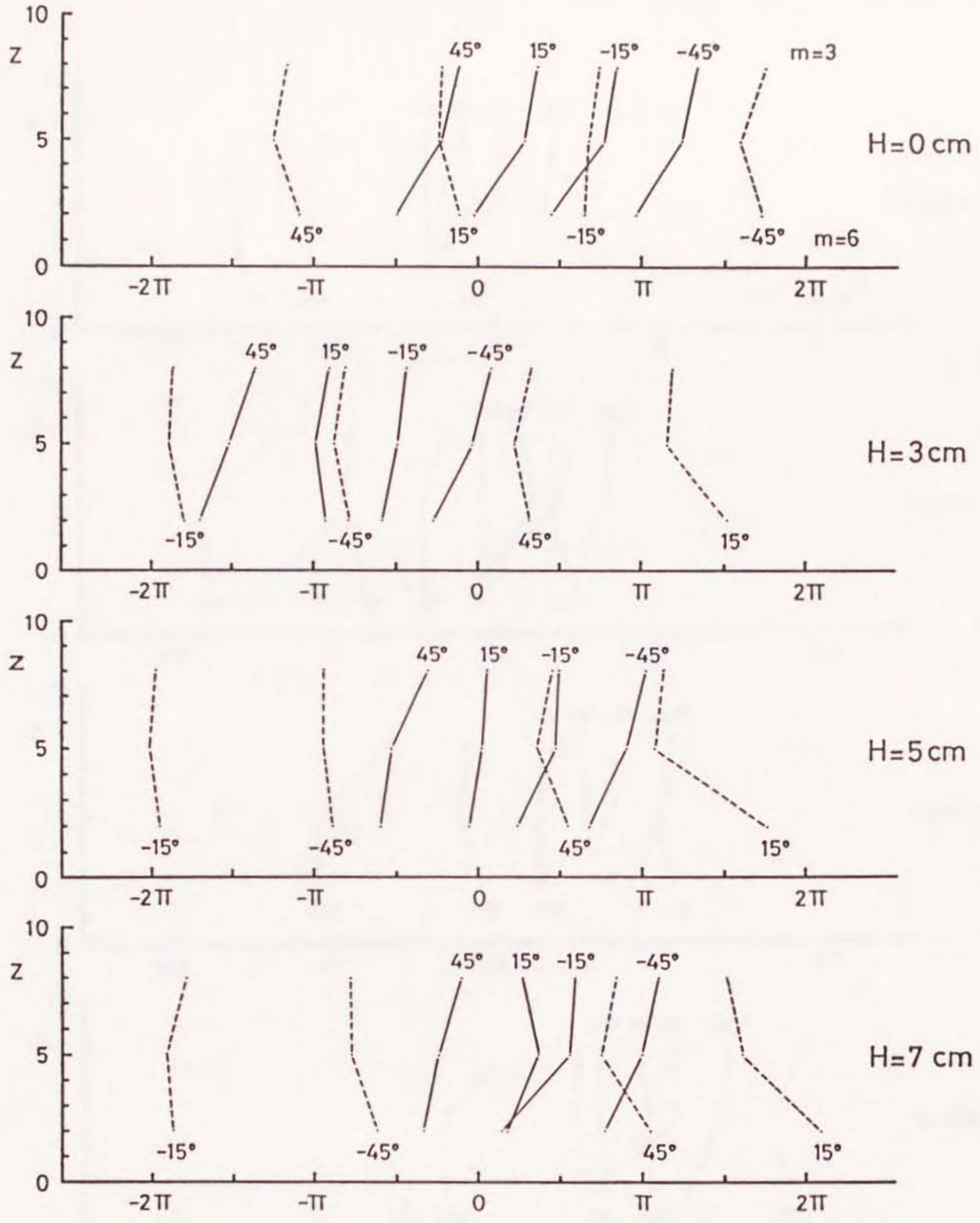

Fig. 18(b) Same as Fig. 17(a) but for $\Omega = 3.0 \times 10^{-1}$ rad/s and k = 3.

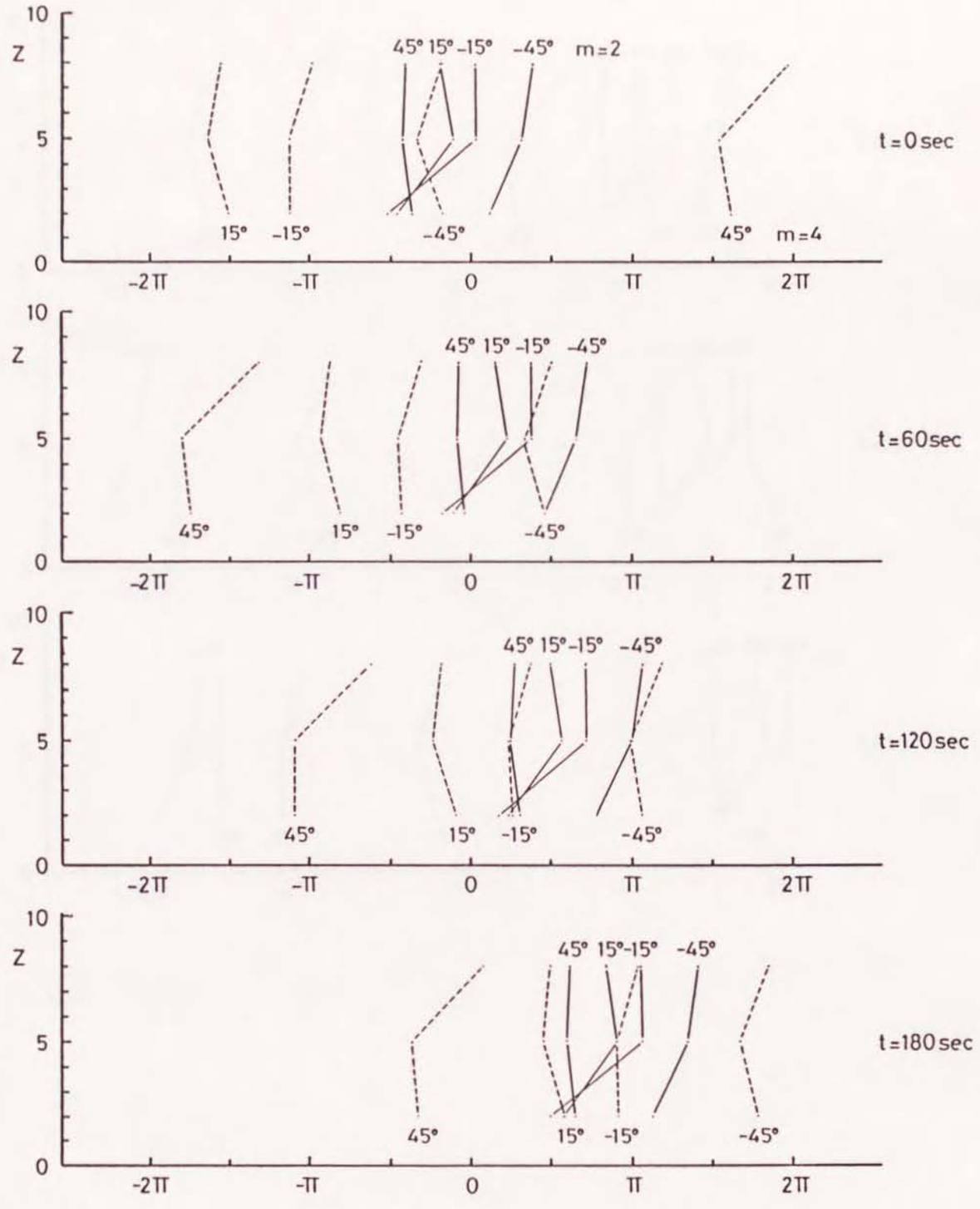

Fig. 19(a) Time sequence of the vertical structure of baroclinic waves, where $\Omega = 2.50 \times 10^{-1}$ rad/s , k = 2 and H/d = 0.7.

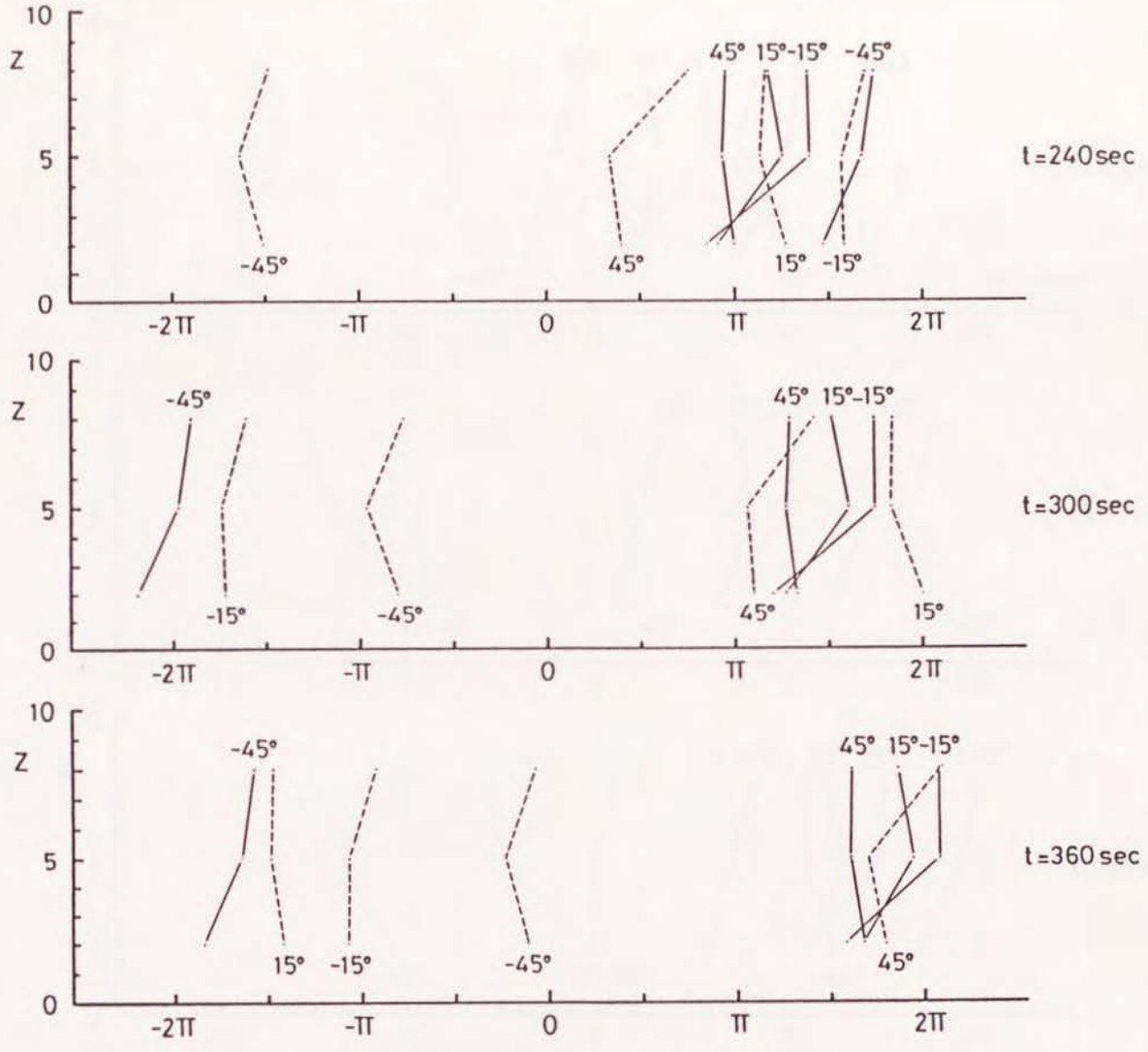

Fig. 19(a) (continued)

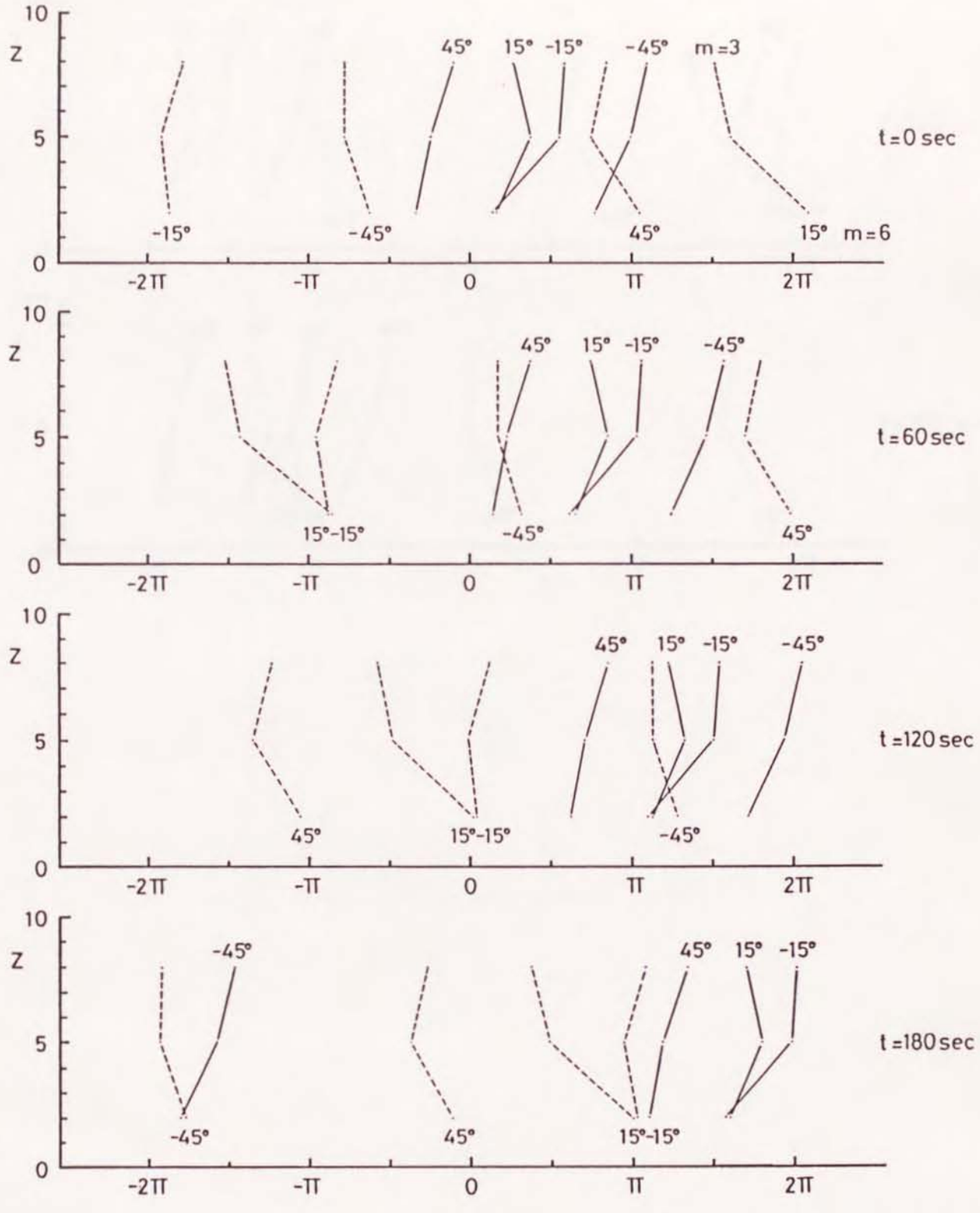

Fig. 19(b) Same as Fig.19(a) but for $\Omega = 3.00 \times 10^{-1}$ rad/s , k = 3 and H/d = 0.5.

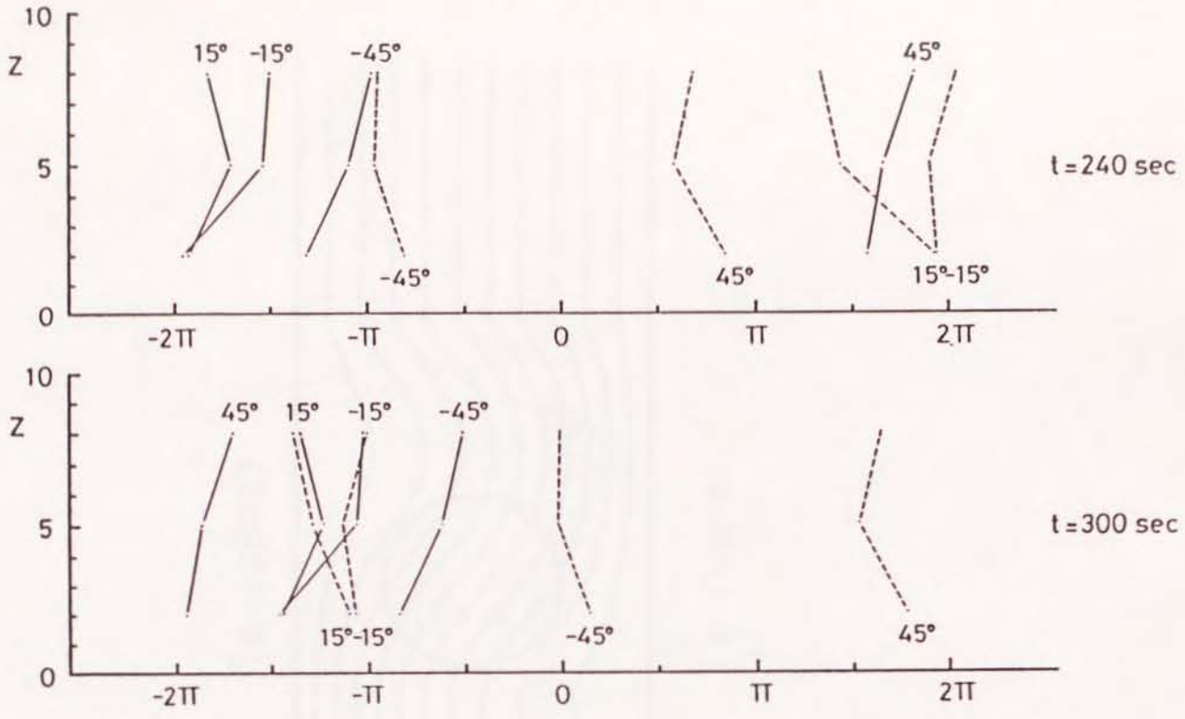

Fig. 19(b) (continued)

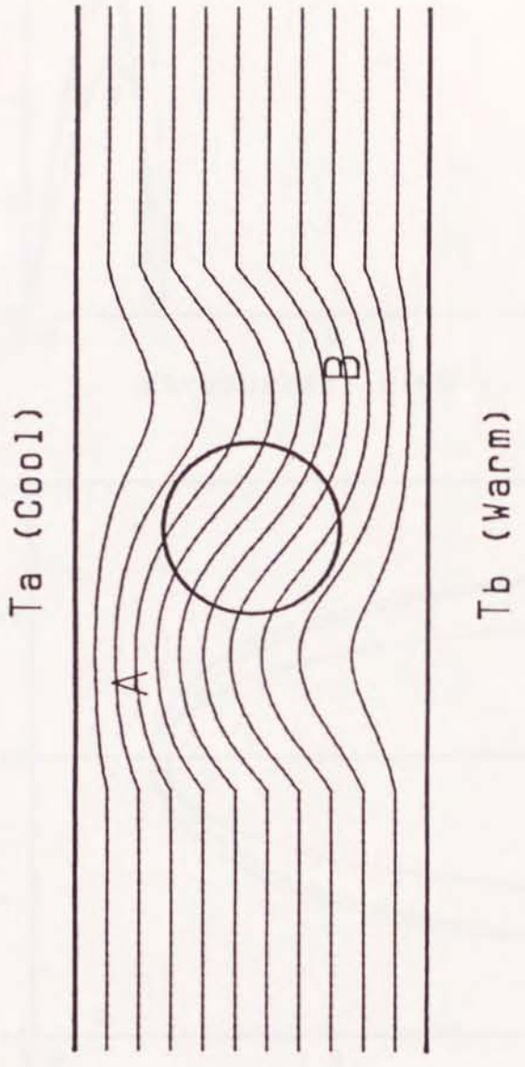

Fig. 20 The schematic plan view of the skewed temperature field around the obstacle.

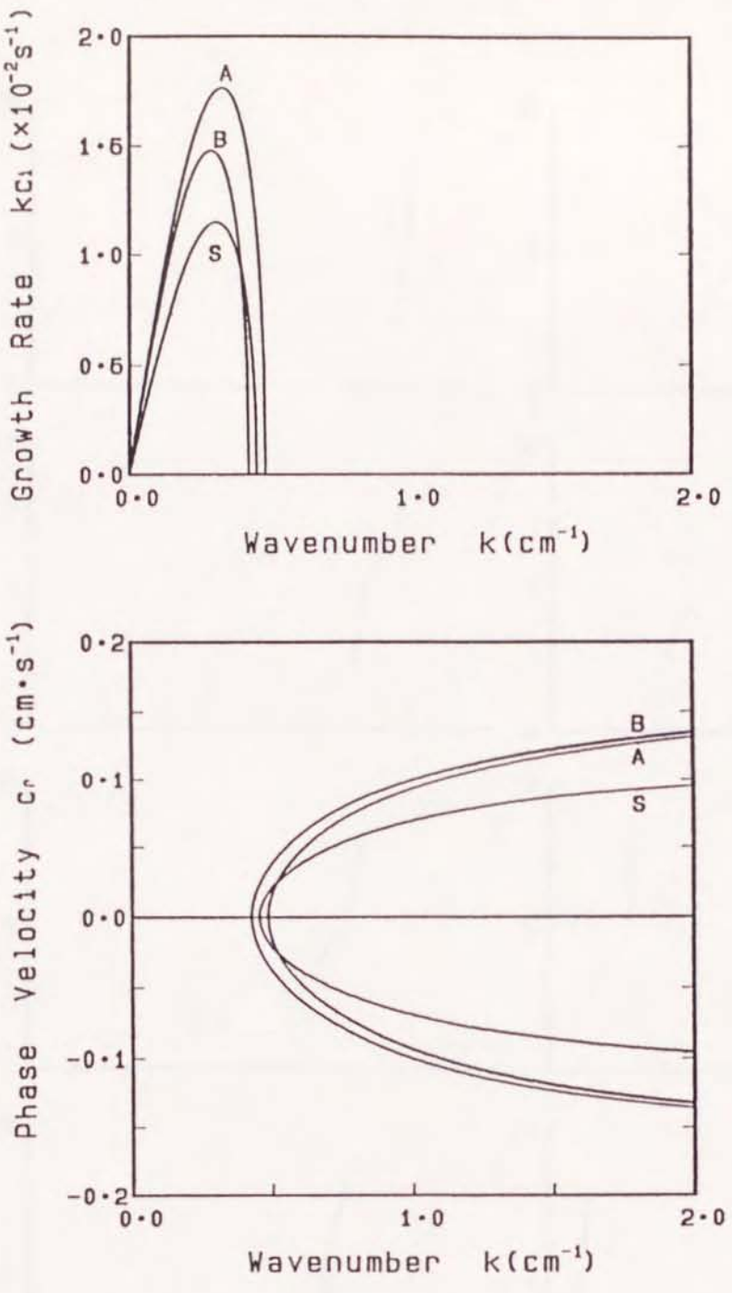

Fig. 21 The dependence of the growth rates (top panel) and the phase velocities (bottom panel) of baroclinic waves on wavenumber k at the northwest region of the obstacle A, the southeast region of the obstacle B and the undisturbed region S.

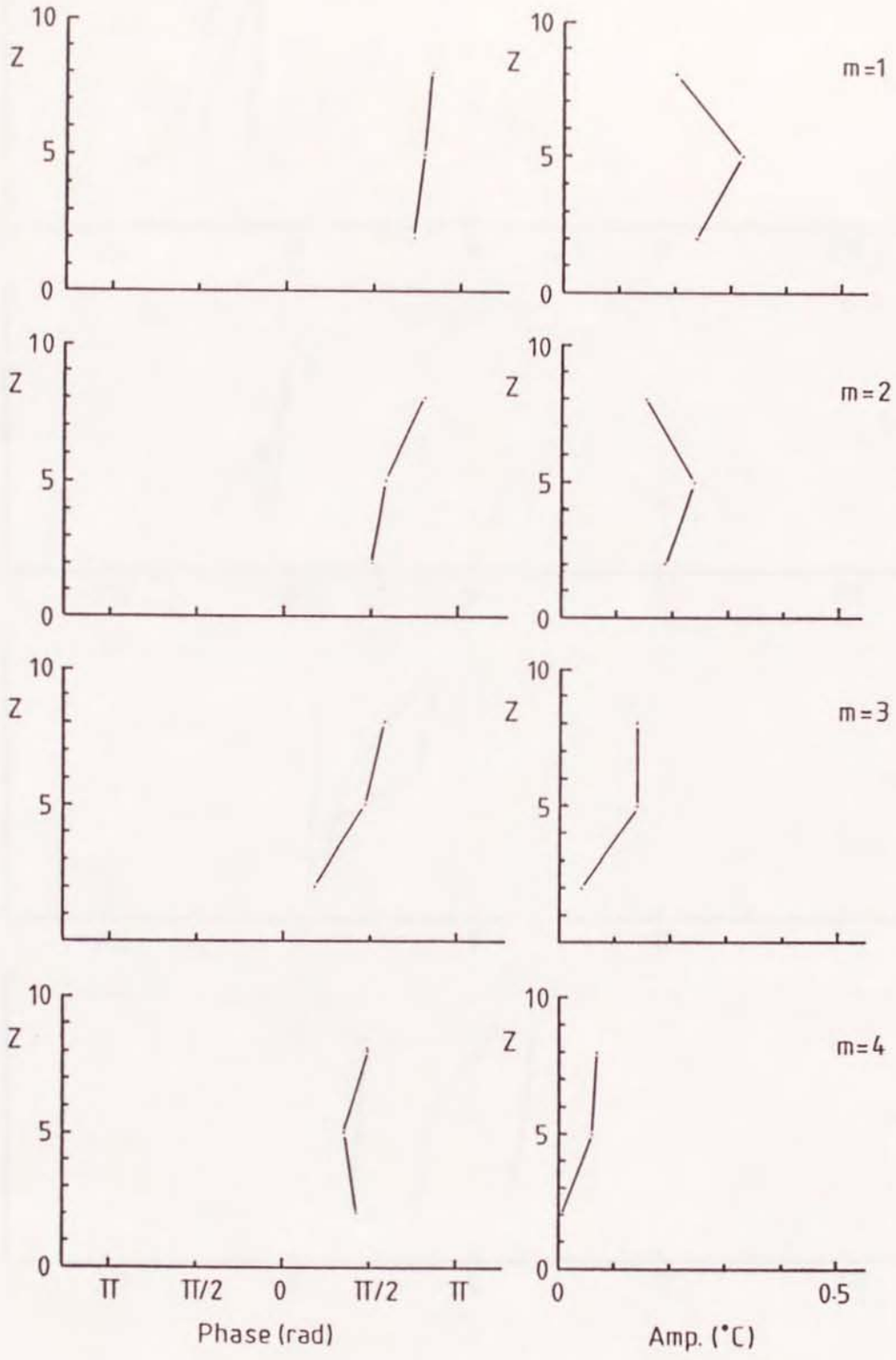

Fig. B1 The vertical structure of the amplitude and the phase line of each Fourier component of temperature perturbation from the ground to the fourth harmonic of wavenumber 1.

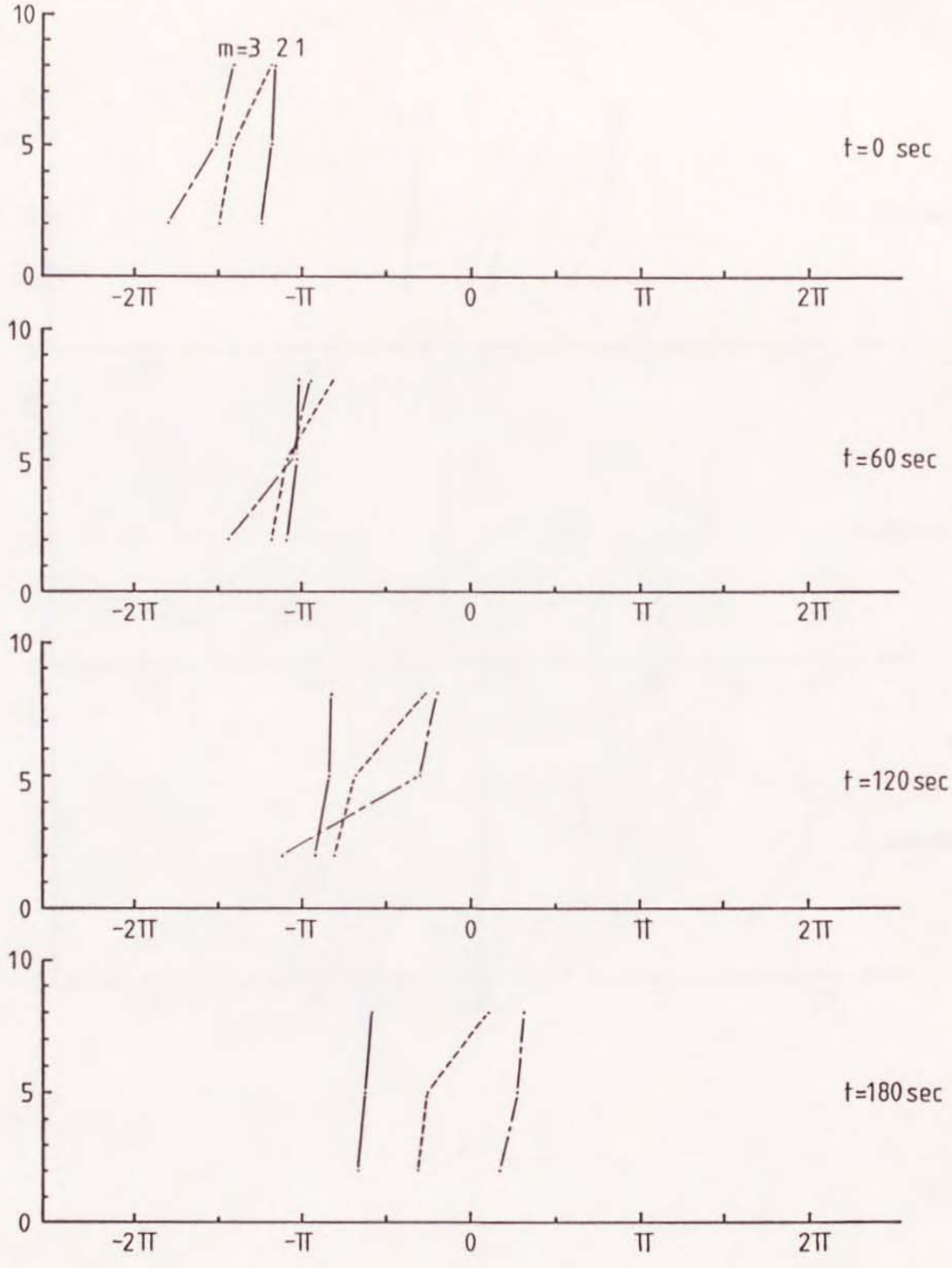

Fig. B2 Time sequence of the vertical structure of the wave of wavenumber 1, where $\Omega = 2.218 \times 10^{-1}$ rad/s , $H/d = 0.8$, $\Theta = 1.824$ and $Ta = 1.313 \times 10^{7}$.

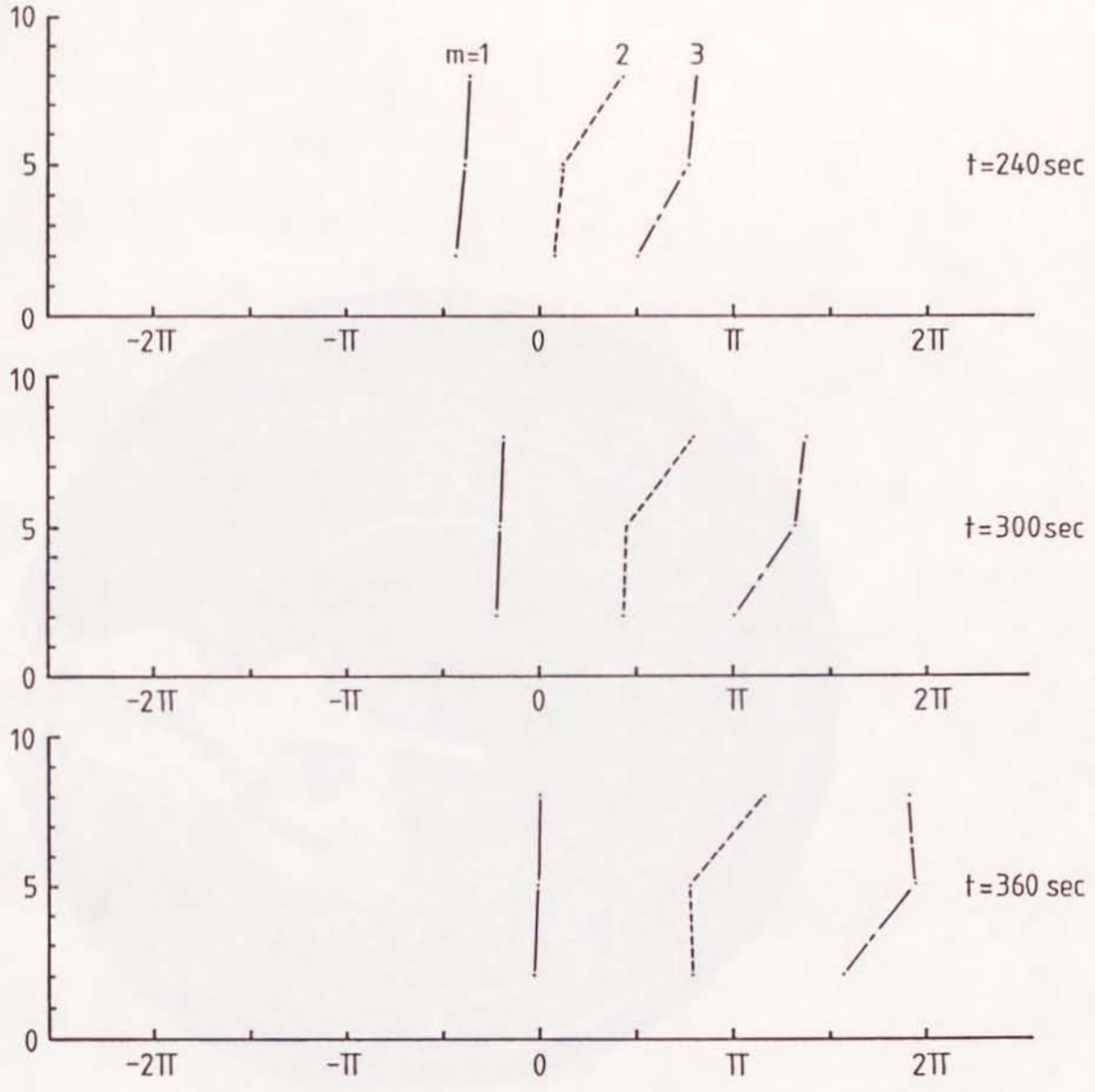

Fig. B2 (continued)

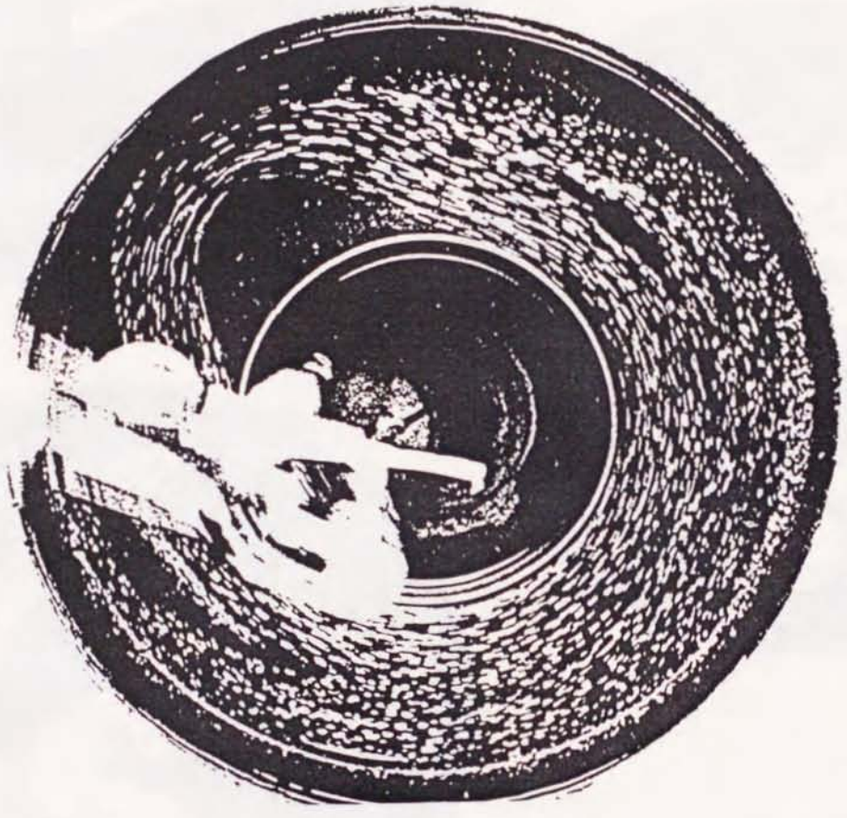

Photo. 1 The streak photograph of the surface flow of the baroclinic wave with wavenumber 1, where the exposure time is 1 second, $\Delta T = 3.2℃$, $H/d = 5/8$, $\Omega = 1.661\times 10^{-1}$ rad/s, $\Theta = 2.210$ and $Ta = 1.216\times 10^{7}$.

Photo. 2 The streak photographs of the surface flow of baroclinic waves with wavenumber 3, where the exposure time is 1 second, $\Delta T = 9.0℃$, $H/d = 3/8$, $\Omega = 3.180\times 10^{-1}$ rad/s, $\Theta = 1.933$ and $Ta = 5.265\times 10^{7}$.

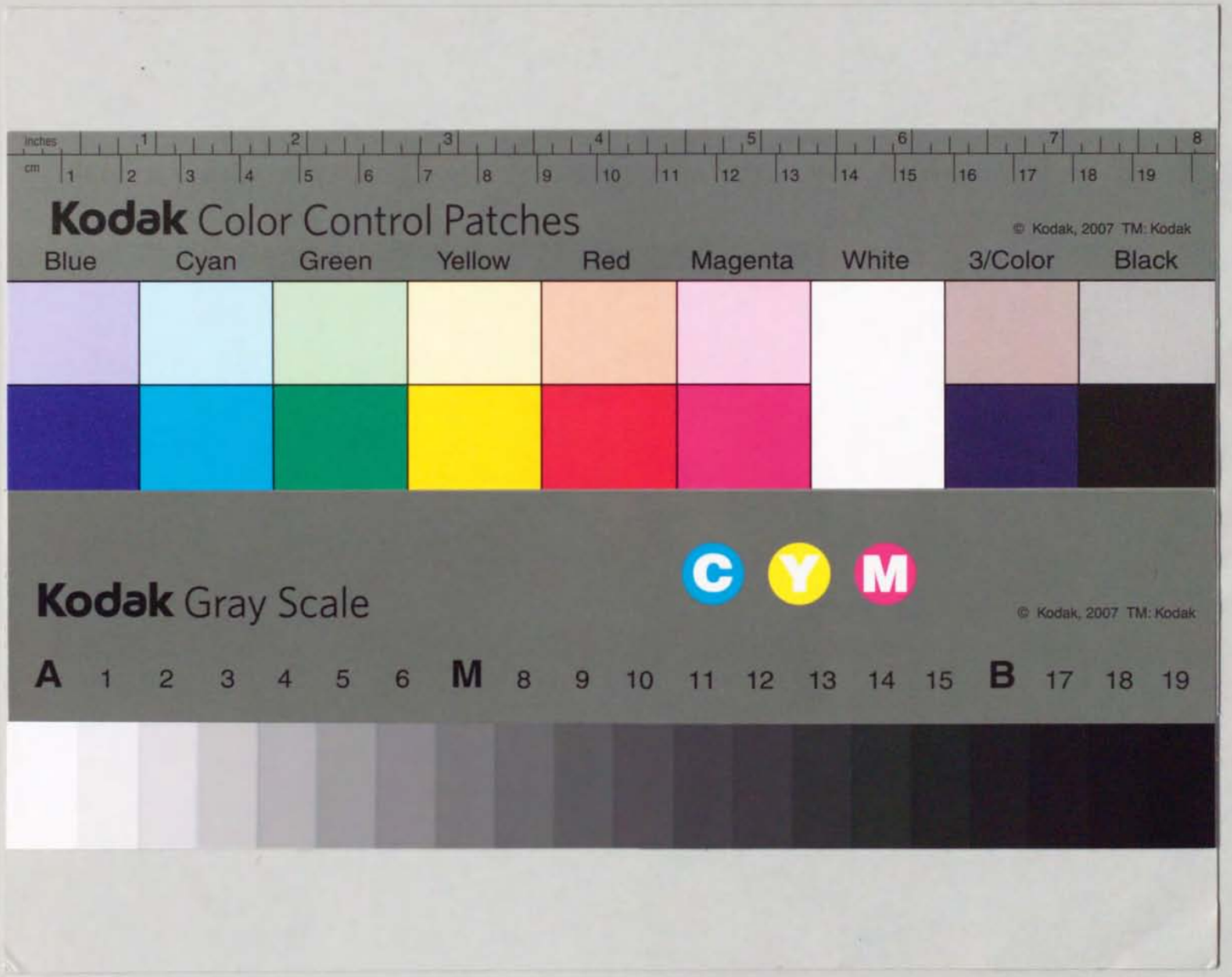
inches
cm
Kodak Color Control Patches
© Kodak, 2007 TM: Kodak
Blue
Cyan
Green
Yellow
Red
Magenta
White
3/Color
Black
Kodak Gray Scale
C
Y
M
© Kodak, 2007 TM: Kodak
A 1 2 3 4 5 6 M 8 9 10 11 12 13 14 15 B 17 18 19